ALMA MATER STUDIORUM - UNIVERSITÀ DI BOLOGNA

FACOLTÀ DI SCIENZE MATEMATICHE FISICHE E NATURALI
DOTTORATO DI RICERCA IN FISICA, XXI CICLO
Area 02 – Scienze Fisiche: FIS/04 Fisica Nucleare e Subnucleare

Ph.D. Thesis

The Time-Of-Flight detector of ALICE at LHC: construction, test and commissioning with cosmic rays

Dr. Roberto Preghenella

Advisor:
Professor
Luisa Cifarelli

Ph.D. coordinator:
Professor
Fabio Ortolani

Bologna, Italy, 2009

Ph.D. Thesis

The Time-Of-Flight detector of ALICE at LHC: construction, test and commissioning with cosmic rays

Dr. Roberto Preghenella

Advisor:
Professor
Luisa Cifarelli

Ph.D. coordinator:
Professor
Fabio Ortolani

*If both the past and the external world
exist only in the mind, and if the mind
itself is controllable – what then?*

George Orwell, 1984

Contents

Introduction

After several years of research and development the Time-Of-Flight detector of ALICE (A Large Ion Collider Experiment) has been constructed and is presently fully installed and operative in the experimental area located at the interaction point n.2 of the LHC (Large Hadron Collider) at CERN[1]. Many people have worked hard to carry out the various tasks which eventually led to the final apparatus and I am really glad to write this report just after the end of a long period dedicated to detector construction and commissioning. Moreover, though not documented here, during these years a big effort has also been made to develop the necessary software tools which allow to obtain from the detector the relevant quantities for physics analysis.

The Time-Of-Flight (TOF) detector was proposed in 1999 and presented at the beginning of 2000 in the ALICE Technical Design Report n.8 as a central detector for the ALICE experiment, dedicated to the identification of charged particles in the intermediate momentum range over the full central region. ALICE has been designed as a general-purpose detector to address the physics of the strongly-interacting matter and the Quark-Gluon Plasma (QGP) at the extreme values of temperature and energy density provided by the LHC nuclear collisions. For this reason a design based on a large number of readout channels was chosen for the TOF detector in order to cope with the extremely high charged-particle density foreseen.

The interest of physics in ultrarelativistic heavy-ion collisions has recently further increased following the exciting results of RHIC (Relativistic Heavy Ion Collider) at BNL[2] which reveal collective bulk phenomena and other features as possible signatures of a new state of matter: the QGP. The formed

---

[1]European Organization for Nuclear Research.
[2]Brookhaven National Laboratory.

matter seems to be different from the asymptotically free QGP, originally proposed in 1975, and heavy-ion collisions at the LHC will enable to shed light on that. In the first chapter a brief introduction on heavy-ion collisions and the features of a hot and dense QCD matter are outlined. Some of the experimental probes which have been proposed as signatures of QGP formation are also discussed. Finally the ALICE experiment is briefly described focusing on the detector layout and its subsystems.

Particle identification in ALICE is essential, as many observables are either mass or flavour dependent, therefore many different techniques are used to cover the largest possible momentum range. As said, the TOF (Time-Of-Flight) detector, of which a comprehensive review is given in Chapter 2, is dedicated to hadron identification at medium momenta. The detector exploits the novel technology based on the Multigap Resistive Plate Chamber (MRPC) which guarantees the excellent performance required for a very large time-of-flight array. The construction of the ALICE TOF detector has required the assembly of a large number of MRPC detectors which has been successfully carried out thanks to a careful mass production controlled by strict quality assurance procedures. The uniformity in the production and in detector performance are stressed in Chapter 3 which focuses on the quality assurance tests performed during all the phases of the construction of the detector. In Chapter 3 the online data quality monitor tools for the TOF detector are also presented.

The fourth chapter aims at presenting the first results obtained with cosmic rays during the global commissioning phase of ALICE along with a brief description of the first data-taking experience. The trigger system of the TOF detector has been long commissioned and besides the TOF many other ALICE detectors have taken advantage of it for data-taking with cosmic rays. A first and preliminary calibration of the detector has been achieved with cosmic rays providing, although the low statistics collected so far prevents the optimal calibration based on a channel-to-channel approach, satisfactory results which allow to push the time-resolution performance close to the target one. Moreover, further studies prove that the information provided by the TOF detector can be successfully combined with other detectors and will thus contribute to the physics analysis since the first collisions at the LHC, extending the particle-identification capabilities of ALICE to higher momenta.

Riassunto

Il rivelatore Time-Of-Flight (TOF) di ALICE (A Large Ion Collider Experiment) è progettato per l'identificazione delle particelle cariche prodotte nelle collisioni nucleari di LHC (Large Hadron Collider) allo scopo di studiare la fisica della materia fortemente interagente ed il Quark-Gluon Plasma (QGP). Il rivelatore sfrutta la tecnologia innovativa MRPC (Multigap Resistive Plate Chamber) che garantisce le eccellenti prestazioni richieste ad un vasto sistema per la misura del tempo di volo. La costruzione e l'installazione dell'apparato nel sito sperimentale sono state completate ed il rivelatore è attualmente operativo in tutte le sue parti. Tutti i passi necessari per la costruzione del rivelatore finale sono stati accompagnati da una serie di procedure per il controllo della qualità della produzione allo scopo di garantire prestazioni elevate ed uniformi; infine il corretto funzionamento del rivelatore è stato verificato con raggi cosmici.

Questa tesi ha lo scopo di fornire una visione d'insieme dettagliata del rivelatore TOF di ALICE, focalizzando l'attenzione anche sui test effettuati durante le fasi di costruzione. Oltre ad una breve descrizione dell'esperienza acquisita nelle prime fasi di presa dati, sono presentati i primi risultati ottenuti con raggi cosmici che confermano promettenti le prestazioni del rivelatore TOF per lo studio delle collisioni di LHC.

Chapter 1

The ALICE experiment at LHC

1.1   Heavy-ion collisions at LHC

The longstanding main objective of heavy-ion physics is to explore the phase diagram of strongly-interacting matter, to study the QCD[1] (Quantum Chromo-Dynamics) phase transition and the physics of the Quark-Gluon Plasma (QGP) state[2]. This will allow to study and understand how collective phenomena and macroscopic properties of complex and dynamically evolving systems emerge from the microscopic laws of elementary-particle physics, validated over the last decades in the Standard Model[3] (SM).

The most striking collective bulk phenomenon predicted by the Standard Model is the occurrence of phase transitions in quantum fields at characteristic energy densities. This affects crucially our present understanding of both low-energy structure of the Standard Model itself and the evolution of the early Universe[4] [1]. Moreover, within the Standard Model, the appearance of a phase transition is intrinsically connected to the breaking of fundamental

---

[1]Gauge field theory of strong interactions. See Section 1.1.1 for more details.

[2]See Section 1.1.2 for more details.

[3]The Standard Model (SM) is a detailed, though still incomplete, theory of elementary particles and their interactions.

[4]According to Big-Bang cosmology, the Universe evolved from an initial state of extreme energy density to its present state. During its evolution, it underwent a rapid expansion and cooling, thereby traversing the series of phase transitions predicted by the Standard Model (Figure 1.1). Global features of the Universe are believed to be linked to characteristic properties of these phase transitions (i.e. baryon asymmetry, large-scale structures).

Figure 1.1: Evolution of the temperature of the Universe as a function of the time elapsed after the Big-Bang.

symmetries of nature[5]. Particle content and particle masses originate as a consequence of the breakdown of the symmetry.

Heavy-ion collisions at the CERN Large Hadron Collider (LHC) [2] will allow to observe and study the hadronic matter embedded in an extreme temperature and energy-density environment, where the transition to QGP is expected to occur. For this purpose, the LHC will accelerate, besides protons, also lead ions[6] to make them collide at a centre-of-mass energy $\sqrt{s} = 5.5$ TeV per nucleon pair. The energy density available after such violent events should be high enough to heat the system above the critical temperature, melting hadrons into a deconfined state of quarks and gluons. Lattice calculations predict a critical temperature $T_c \simeq 170$ MeV, corresponding to an energy density $\epsilon \simeq 1$ GeV/fm^3, for the transition to occur. Furthermore, heavy-ion collisions offer the possibility to observe how the Universe was looking like about 10^{-6} seconds after the Big-Bang (Figure 1.1).

---

[5]In general, intrinsic symmetries of the theory, which are valid at high energy densities, are broken below a certain critical energy density.

[6]The Large Hadron Collider (LHC) at CERN will accelerate protons as well as lead ions. The design centre-of-mass energy for pp collisions and Pb–Pb collisions is $\sqrt{s} = 14$ TeV and $\sqrt{s} = 5.5$ TeV per nucleon pair, respectively. The design luminosity if of 10^{34} cm^{-2}s^{-1} for pp collisions and of 10^{27} cm^{-2}s^{-1} for Pb–Pb collisions [3].

A rich ultrarelativistic heavy-ion programme has been carried out during the past years at BNL-AGS and CERN-SPS[7] and it is still under way at the BNL Relativistic Heavy-Ion Collider (RHIC)[8]. Despite the data from RHIC over the last years have led many to conclude that the medium created is not the expected Quark-Gluon Plasma[9], but rather a strongly-interacting quark-gluon plasma (sQGP [7]), for simplicity reason we will keep referring to this state as QGP.

1.1.1 Quantum Chromo-Dynamics

Quantum Chromo-Dynamics (QCD) describes the interaction of quarks and gluons in the form of a gauge field theory, very similar to the way Quantum Electro-Dynamics (QED) does for electrons and photons. In both cases we have spinor matter fields interacting through massless vector gauge fields. In QCD, however, the intrinsic colour charge is associated to the non-Abelian gauge group $SU(3)$, in place of the Abelian group $U(1)$ for the electric charge in QED. The quarks thus carry three colour charges, and the gluons, transforming according to the adjoint representation, carry eight. The intrinsic charge of the gauge field (the gluon) is the decisive modification in comparison to QED; it makes the pure gluon system self-interactive, in contrast to the ideal gas of photons. As a result, the three-dimensional Laplace equation, which in non-relativistic QED leads to the Coulomb potential $V \sim 1/r$, for massive quarks becomes effectively one-dimensional, with the confining potential $V \sim r$ as the solution.

The Lagrangian density of QCD is given by

$$\mathcal{L} = -\frac{1}{4} F_{\mu\nu}^a F_a^{\mu\nu} + \sum_f \bar{\psi}_\alpha^f (i\gamma_\mu \mathcal{D}^\mu)^{\alpha\beta} \psi_\beta^f, \tag{1.1}$$

with

$$F_{\mu\nu}^a = (\partial_\mu A_\nu^a - \partial_\nu A_\mu^a - g f_{bc}^a A_\mu^b A_\nu^c) \tag{1.2}$$

---

[7]Ultrarelativistic heavy-ion collisions have been first studied at GSI-SIS (Heavy-Ion Synchrotron) at $\sqrt{s} \sim 2$ GeV per nucleon pair and at the BNL-AGS (Alternate Gradient Synchrotron) at $\sqrt{s} \sim 5$ GeV per nucleon pair [4]. At the CERN-SPS (Super Proton Synchrotron) collisions occurred at $\sqrt{s} \sim 20$ GeV per nucleon pair [5].

[8]At the BNL-RHIC (Relativistic Heavy-Ion Collider) gold nuclei collide at energies up to $\sqrt{s} \sim 200$ GeV per nucleon pair [6].

[9]An asymptotically free ideal gas of quarks and gluons.

and

$$\mathcal{D}_\mu = \partial_\mu + ig\frac{\lambda_a}{2}A_\mu^a. \tag{1.3}$$

Here A^a denotes the gluon field of colour a ($a = 1, ..., 8$) and ψ_α^f the quark field of colour α ($\alpha = 1, 2, 3$) and flavour f. λ_a are the Gell-Mann matrices. The inclusion of quark masses would add a term

$$\mathcal{L}_m = \sum_f m_f \bar{\psi}_\alpha^f \psi^{\alpha,f} \tag{1.4}$$

in Eq. 1.1. Equation 1.3 contains one dimensionless coupling constant g, and hence Eq. 1.1 provides no scale: QCD predicts only the ratios of physical quantities, not absolute values in terms of physical units.

In QCD hadrons are colour-neutral bound states of quarks (baryons) or of quark-antiquark pairs (mesons); they are thus the chromodynamic analog of atoms or positronium as the electrically-neutral bound states in QED. The difference between the two theories becomes significant at large distances: while a finite ionization energy ΔE suffices to break up the electrodynamic bound, this is not possible in the case of quark binding. This property of the QCD leads to the concept of "confinement": quarks and gluons are confined inside hadrons. At short distances QCD shows another peculiar behaviour: the decrease of the colour charge with decreasing the distance from the colour-probe to the charge itself. This leads to the concept of "asymptotic freedom", which implies that partons[10] inside hadrons interact weakly among themselves and can be considered as almost free.

1.1.2 Hot and dense QCD matter: the QGP

The idea of an intrinsic limit to hadron thermodynamics was the starting point which led to the present understanding that ordinary matter should undergo a phase transition to a new, hot and dense state of matter. Different conceptual approaches had led to an ultimate temperature of strongly-interacting matter. Pomeranchuk [8] first obtained it from the finite spatial extension of hadrons: a hadron can only have an independent existence if it has an independent volume. Then Hagedorn [9], before QCD was established as the fundamental theory of strong interactions, stated that the mass

---

[10]The basic constituents of hadrons, namely quarks and gluons.

spectrum of resonances produced in hadronic collisions implies some form of critical behaviour at high temperature and/or density. With the advent of the quark infrastructure of hadrons, the subsequent formulation of QCD and the observation that QCD is an asymptotically free theory, it became clear that the ultimate temperature at which the critical behaviour sets in is related to a transition point to a new state of matter, to a "plasma" of deconfined quarks and gluons [10].

At very short distances, as it has been already pointed out in the previous section, the QCD coupling constant between partons is weak and it decreases as the distance between partons decreases (asymptotic freedom). An expected consequence of asymptotic freedom is that a system created by heating the vacuum to high temperature should have the properties of an almost ideal relativistic gas in which colour is deconfined [11]. The high temperature of this medium entails an extremely high concentration of partons, whose thermodynamics follows the Stefan-Boltzmann law.

At another extreme, it is known that the only stable configuration of strongly-interacting matter at low temperature and densities is the multitude of colour-neutral objects, which we call "hadrons". In addition, the QCD Lagrangian is understood to have a higher symmetry than the observed hadron states. The solutions of QCD at normal temperature and densities[11] spontaneously break the so-called "chiral symmetry" [12–14]. The questions of what form and phases of QCD matter exist between the two extremes and what symmetries, properties and interactions characterize these phases, are currently the subject of very active theoretical and experimental research.

The existence of a phase transition from the ordinary hadronic matter (hadron gas) to a quark and gluon matter (quark-gluon plasma) has been convincingly demonstrated by statistical QCD in the finite-temperature lattice formulation. Experimental attempts to create the QGP in the laboratory and measure its properties have been carried out for more than 20 years, by studying collisions of heavy nuclei and analyzing the fragments and produced particles emanating from such collisions.

No decisive proof of QGP formation was found in the BNL-AGS heavy-ion experiments, but at CERN-SPS a number of signals pointing to the formation of a new dense state of matter were found [15, 16]. The subsequent results collected so far by RHIC experiments can be taken as further evi-

---

[11]Temperatures and densities which correspond to normal matter, that is the world of hadrons and nuclei.

3-flavour phase diagram

$T_\chi^{n_f=2} \sim 175$ MeV

$n_f = 2$

Pure Gauge

$T_d \sim 270$ MeV

∞

2nd order
O(4) ?

1st order

m_s^{tric}

$n_f = 3$

$m_{PS}^{crit} \simeq 2.5$ GeV

? phys. point

crossover

$n_f = 1$

m_s

?

2nd order
Z(2)

$m_{PS}^{crit} \simeq 300$ MeV

1st order

$\overline{\chi}^{n_f=3} \sim 155$ MeV

0

0

m_u , m_d

∞

Figure 1.2: The QCD phase diagram of 3-flavour QCD with degenerate (u,d)-quark masses $m_u = m_d$ and a strange-quark mass m_s.

dence for the formation of a state of deconfined partonic matter [17–20], the so called Quark-Gluon Plasma (QGP). Nonetheless, they have led many to conclude that the medium created is not the expected Quark-Gluon Plasma (QGP), but rather a strongly-coupled or strongly-interacting quark-gluon plasma (sQGP). The name "sQGP" [7] helps to distinguish that matter from ordinary hadronic resonance matter and also from the original 1975 asymptotically free QGP [10].

1.1.3 QCD phase transition and diagram

At vanishing baryon number density or zero chemical potential[12] the properties of the QCD phase transition depend on the number of quark flavours

---

[12]In thermodynamics the chemical potential μ measures the amount of change of the system internal energy U after introducing an additional particle

$$\mu = \frac{\partial U}{\partial N}. \tag{1.5}$$

The baryo-chemical potential μ_B measures the same quantity after introducing an additional baryon.

6

Figure 1.3: Lattice Monte Carlo results on the QCD phase boundary [21, 22] shown together with chemical freeze-out conditions obtained from a statistical analysis of experimental data (open symbols) [23, 24].

and their masses. While it is a detailed quantitative question at which temperature the transition to the high-temperature plasma phase occurs, we do expect that the nature of the transition, e.g. its order and details of the critical behaviour, are controlled by global symmetries of the QCD Lagrangian. Such symmetries only exist in the limits of either infinite ($m_q \to \infty$) or vanishing ($m_q \to 0$) quark masses. For any non-zero value of quark masses the global symmetries are explicitly broken. In fact, in the case of QCD the explicit symmetry breaking induced by the finite quark masses is very much similar to that induced by an external ferromagnetic field in spin models. We thus expect that a continuous phase transition, which may exist in the

zero or infinite quark-mass limit, will turn into a non-singular crossover behaviour for any finite value of the quark mass. First-order transitions, on the other hand, may persist for some time before they end in a continuous transition. Whether a true phase transition exists in QCD with the physically realized spectrum of quark masses or whether in this case the transition is just a (rapid) crossover is a quantitative question which has to be addressed through direct numerical calculations.

In the limit of infinitely heavy quarks ($m_q \to \infty$), the pure $SU(3)$ gauge theory, the large-distance behaviour of the heavy-quark free energy[13] provides a unique distinction between confinement below T_c and deconfinement for $T > T_c$. The effective theory for the order parameter is a 3-dimensional spin model with global $Z(3)$ symmetry. A first-order phase transition is expected in the infinite quark-mass limit [26].

In the limit of vanishing quark masses ($m_q \to 0$) the classical QCD Lagrangian is invariant under chiral symmetry transformation; for n_f massless quark flavours the symmetry is

$$U_A(1) \times SU_L(n_f) \times SU_R(n_f). \qquad (1.6)$$

However, only the $SU(n_f)$ flavour part of this symmetry is spontaneously broken in the vacuum, which gives rise to ($n_f^2 - 1$) massless Goldstone particles, the pions. The basic observable which reflects the chiral properties of QCD is the chiral condensate $\langle \bar{\chi}\chi \rangle$. In the limit of vanishing quark masses the chiral condensate stays non-zero as long as chiral symmetry is spontaneously broken. The chiral condensate thus is an obvious order parameter in the chiral limit.

For light quarks the global chiral symmetry is expected to control the critical behaviour of the QCD phase transition. In particular, the order of the transition is expected to depend on the number of light or massless flavours [27]. So far no theoretical indication for a discontinuous transition has been observed for $n_f = 2$. The transition is found to be first-order for $n_f \geq 3$.

The phase diagram of 3-flavour QCD at vanishing baryon number density is shown in Fig. 1.2. An interesting aspect of the phase diagram is the

---

[13]The heavy quark free energy $F_{\bar{q}q}$ can be calculated on the lattice from the expectation value of the Polyakov loop correlation function [25]. The Polyakov loop expectation value is an order parameter for deconfinement in the $SU(3)$ gauge theory.

Figure 1.4: Lattice QCD results [25] for ϵ/T^4 as a function of the temperature scaled by the critical temperature T_c. Note the arrows on the right side indicating the values for the Stefan-Boltzmann limit ϵ_{SB} as given by Eq. 1.11.

occurrence of a second-order transition line in the light quark-mass regime, the boundary of the region of first-order phase transitions.

Figure 1.3 shows the results on the position of the phase boundary and a compilation of the chemical freeze-out parameters, extracted from experimental data in a very broad range of energy[14] [23, 24, 28–30], together with the freeze-out condition of fixed energy per particle $\simeq 1$ GeV. It is interesting to note that already at SPS and RHIC the chemical freeze-out parameters coincide with the critical-temperature conditions obtained from lattice QCD.

1.1.4 Lattice QCD calculations

The phase transition of ordinary QCD matter to a quark-gluon plasma state is quantitatively best studied in QCD thermodynamics within the

---

[14]Data from GSI-SIS, BNL-AGS, CERN-SPS and BNL-RHIC.

framework of lattice QCD. Phase transitions are related to large-distance phenomena in a thermal medium, to the collective behaviour and spontaneous breaking of global symmetries. In order to study such mechanisms in QCD we need a calculation approach able to deal with all non-perturbative aspects of the theory of strong interactions: this is precisely the purpose of lattice QCD [31]. A discrete space-time lattice is introduced in this formulation of QCD, well suited for numerical calculations[15].

As already discussed in the previous section, lattice calculations predicted that the transition to the high-temperature phase of QCD is continuous and non-singular for a large range of quark masses. Nonetheless, for all quark masses this transition proceeds rather rapidly in a small temperature interval. A definite transition point can be identified in the lattice QCD formulation through the location of peaks in the susceptibility of the Polyakov loop or the chiral condensate.

In lattice QCD calculations the order of transition as well as the value of the critical temperature depend on the number of flavours and quark masses [25, 32, 33]. In the pure $SU(3)$ gauge theory (infinite quark masses) one finds that the critical temperature of the first-order phase transition is $T_c^{(pure\ gauge)} = (271 \pm 2)$ MeV [25]. Calculations for the transition temperature with light quarks indicated that the inclusion of light quarks leads to a significant decrease of the transition temperature. In the chiral limit of 2-flavour QCD one finds a critical temperature of $T_c = (173 \pm 8)$ MeV, being about 20 MeV smaller for 3-flavour QCD [25, 32]. The influence of a small chemical potential has been estimated as well and for typical chemical potentials characterizing the freeze-out at RHIC ($\mu_B \simeq 50$ MeV) it has been found to be small[16] [21, 34, 35]. Although the phase transition has been estimated of the second order in the chiral limit of 2-flavour QCD and of the first order for 3-flavour QCD, it is likely to be only a rapid crossover in the case of physical quark masses. The crossover, however, takes place in a narrow temperature range, making the transition still well localized. This reflects a rapid rise of the energy density at the critical temperature (Figure 1.4).

---

[15]Lattice QCD calculations involve systematic errors due to the finite lattice space $a > 0$ and higher quark masses. In principle, both sources of systematic errors can be eliminated, however the required computational power increases rapidly with decreasing lattice space and quark masses.

[16]The influence of a non-zero chemical potential will thus be even less important at LHC energies.

The most fundamental quantity in equilibrium thermodynamics is, of course, the partition function Z itself, or the free energy density

$$f = -\frac{T}{V} \ln Z(T, V), \tag{1.7}$$

where T is the temperature and V is the volume of the system. All basic bulk thermodynamic observables can be derived from the free energy density. In the thermodynamic limit we obtain directly the pressure, $p = -f$ and subsequently also other quantities like the energy (ϵ) and entropy (s) densities or the velocity of sound (c_s),

$$\frac{\epsilon - 3p}{T^4} = T\frac{d}{dT}\left(\frac{p}{T^4}\right), \tag{1.8}$$

$$\frac{s}{T^3} = \frac{\epsilon + p}{T^4}, \tag{1.9}$$

$$c_s^2 = \frac{dp}{d\epsilon}. \tag{1.10}$$

In the limit of infinite temperature asymptotic freedom suggests that these observables approach the ideal-gas limit for a gas of free quarks and gluons (Stefan-Boltzmann constants). At high temperature we expect

$$\frac{\epsilon_{SB}}{T^4} = \frac{3p_{SB}}{T^4} = \left(16 + \frac{21}{2}n_f\right)\frac{\pi^2}{30}. \tag{1.11}$$

1.2 Probing the quark-gluon matter

Quantum Chromo-Dynamics (QCD) predicts a phase transition at sufficiently high energy density from normal hadronic matter to a deconfined state of quarks and gluons, the Quark-Gluon Plasma (QGP). As said, such a phase transition may be achievable in ultrarelativistic heavy-ion collisions. Many QGP signatures have been proposed which include rare probes (e.g. direct photon and dilepton production, jet modification) as well as bulk probes (e.g. enhanced strangeness, strong collective flow).

The aim of this section is to give an overview of some observables that can be measured in ALICE. The simultaneous measurement of these quantities in the same apparatus will probe the matter created by LHC Pb–Pb collisions and allow direct comparisons of its properties.

1.2.1 Kinematic probes and chemical composition

The multiplicities, yields, momentum spectra and correlations of hadrons emerging from heavy-ion collisions, especially in the soft sector comprising particles at transverse momenta $p_t \lesssim 1.5$ GeV/c, reflect the properties of the bulk of the matter produced in the collision.

The average charged-particle multiplicity per rapidity unit (dN_{ch}/dy), on the theoretical side, fixes a global property of the medium produced in the collision. This quantity enters the calculations of most of the observables, being related to the energy density (ϵ) of the system created by the collision. On the experimental side, charged-particle multiplicity per unit rapidity largely influences the detector performance determining the accuracy with which many observables can be measured. Another important "day-one" observable is the total transverse energy per rapidity unit (dE_t/dy). Despite their theoretical and experimental importance there is no calculation able to extract these quantities from the QCD (Quantum Chromo-Dynamics) Lagrangian, being both observables dominated by soft non-perturbative QCD. Nonetheless, studies to derive the charged-particle density at the LHC have been done. A simple approach based on experimental data and "effective energy" arguments has been used in [36, 37] to predict the charged-particle multiplicity and density both in proton–proton and in Pb–Pb collisions at the LHC energies.

The measured hadron spectra reflect the properties of the bulk of the matter at kinetic freeze-out, after elastic collisions among the hadrons have ceased. At this stage the system is already relatively dilute and "cold". However from the detailed properties of the hadron spectra at kinetic freeze-out, information about the earlier hotter and denser stage can be obtained. Somewhat more direct information on an earlier stage can be deduced from the integrated yields of the different hadron species, which change only via inelastic collisions. These inelastic collisions cease already (at the so-called chemical freeze-out) before kinetic freeze-out. The total yields, reflecting the particle abundances and thus the chemical composition of the exploding fireball, are frozen at hadronization and are very weakly affected by hadronic rescattering. The degree to which chemical equilibrium among the hadrons is established provides important constraints on the microscopic chemical reaction processes and their timescales. If it is the case that the chemical freeze-out temperature coincides with the critical temperature predicted

from lattice QCD, the observed equilibrium cannot have been generated via hadronic rescattering due to the short timescale. Equilibrium must have been established by the hadronization process itself: hadrons form into chemical equilibrium.

1.2.2   Electromagnetic probes

A prominent topic of interest in the field of relativistic heavy-ion collisions is the identification of the thermal radiation emitted by the system and in particular the thermal radiation emitted by the QGP via $q\bar{q}$ annihilation. Such radiation is a direct fingerprint of the matter formed and is regarded as a very strong signal of deconfinement. Its spectral shape should provide a direct measurement of the plasma temperature. In principle thermal radiation can be studied through real photons or dileptons. In practice the measurements are extremely challenging. The thermal radiation is expected to be a small signal compared to the large background.

Several mechanisms for photon production are at work at different temporal stages of ultrarelativistic heavy-ion collisions. Early in the collision "prompt" photons are produced by parton–parton scattering in the primary nucleus–nucleus collision, like in nucleon–nucleon collisions. This process can be calculated in perturbative QCD for large enough values of the photon transverse momentum p_t. In the following stage of the collision, quark-gluon plasma is expected to form. Photons are radiated off the quarks which undergo collisions with other quarks and gluons in the thermal bath. Photons are produced as well in the hot hadronic phase and finally, after the freeze-out, further photons can be produced by the decay of π^0 and η mesons. Photons produced by π^0 decays $\pi^0 \to \gamma\gamma$, either from the primary collisions or final-state interactions, constitute a large reducible background to "direct" photons. On the other hand, the "prompt" photons produced in the early stage by partonic scattering provide an irreducible background. Precise estimate of their production rate is needed to extract the rate of thermal photons.

Dilepton production is an important tool for measuring the temperature and the dynamical properties of the matter produced in relativistic heavy-ion collisions. Lepton-pair production is similar to that of photons: there are prompt contributions from the hard nucleon–nucleon collisions, thermal radiation from the quark-gluon plasma and the hot hadronic phase, as well
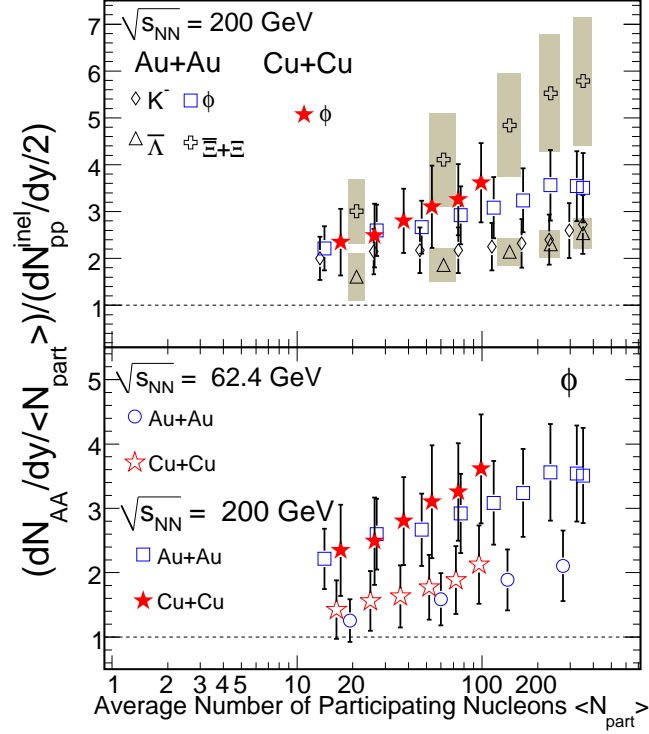
Figure 1.5: Strangeness enhancement measured by the NA57 experiment. The enhancements are defined as the particle yields normalized by the number of participating nucleons in the collision, and divided by the observed yield in proton–beryllium collisions. The yields expected from a simple superposition of nucleon–nucleon collisions would lie on a straight line positioned at unity.

as final-state interactions and meson decays (Dalitz decays, i.e. $\pi^0 \to e^+ e^- \gamma$) after freeze-out. The prompt contribution to the continuum in the dilepton mass range above pair mass $M \sim 2\,\text{GeV}$ is dominated by semi-leptonic decays of heavy-flavour mesons and by the Drell-Yan process and can be calculated in perturbative QCD. The physics objective is then similar to that of the photon case, that is the discrimination of thermal radiation from the large prompt background.

1.2.3 Strangeness enhancement and ϕ meson production

Strange particles are of particular interest since the initial strangeness content of the colliding nuclei is very small and there is no net strangeness. This means that all strange hadrons must be formed in the matter produced. Originally, it was proposed that strangeness production would increase due to the formation of a QGP compared to that from a hadron

Figure 1.6: Strangeness enhancement measured by the STAR experiment. Upper panel: the ratio of the yields of K^-, ϕ, $\bar{\Lambda}$ and $\Xi + \bar{\Xi}$ normalized to $\langle N_{part} \rangle$ in nucleus–nucleus collisions and to corresponding yields in inelastic pp collisions as a function of $\langle N_{part} \rangle$ at 200 GeV. Lower panel: same as above for ϕ mesons in Cu–Cu collisions at 200 and 62.4 GeV.

gas [38]. This enhancement is due to the high production rate of $gg \rightarrow s\bar{s}$ (gluon fusion) in a QGP, a process absent in the hadronic state. The subsequent hadronization of these (anti)strange quarks results in a significant increase in strange particle production. STAR[17] [39] has recently observed an enhanced strange-baryon production in Au–Au collisions compared to pp collisions at $\sqrt{s_{NN}} = 200$ GeV [40]. The enhancement observed increases with the strangeness content of the baryon, and increases for all strange baryons with collision centrality (Figure 1.6). A similar behaviour was al-

---

[17]The Solenoidal Tracker At RHIC (STAR) is one of the experiments at the BNL Relativistic Heavy-Ion Collider (RHIC).

ready observed at CERN SPS [41–43] (Figure 1.5).

The mechanism for ϕ meson production in high-energy collisions has remained an open issue. As the lightest bound state of strange quarks ($s\bar{s}$) with hidden strangeness, ϕ meson production is suppressed in elementary collisions because of the Okubo-Zweig-Iizuka (OZI) rule[18] [44–47]. In an environment with many strange quarks, ϕ mesons can be produced readily through coalescence[19], bypassing the OZI rule [48]. An enhancement of ϕ meson production due to the coalescence of $s\bar{s}$ pairs in the hot medium has been predicted to be a probe of the QGP in ultrarelativistic heavy-ion collisions [38, 49–53], and has been observed by the STAR experiment at RHIC [54, 55] (Figure 1.6).

The chiral properties of vector mesons in the nuclear medium are also interesting [53]. The mass and the width of the ϕ meson were predicted to change due to partial restoration of chiral symmetry in the nuclear medium. A ϕ mass decrease was predicted due to many-body effects in a hadronic medium [56, 57]. A double ϕ peak structure in dilepton invariant-mass spectrum from relativistic heavy-ion collisions was proposed as a signature of a phase transition from the QGP to hadronic matter [58].

The study of the ϕ meson in the $\phi \rightarrow K^+K^-$ decay channel through invariant-mass reconstruction can be performed using the Time-Of-Flight (TOF) detector of ALICE combined with the central tracking detectors [59].

1.2.4   Heavy-quark and quarkonium production

Heavy-quark (charm and bottom quarks) production and attenuation will provide unique tomographic probes of the partonic matter created in the relativistic heavy-ion collisions at LHC energies. Due to their large mass heavy quarks are predicted to lose less energy than light quarks by gluon radiation in the medium [60–62]. In contrast, recent measurements of the p_t distributions and nuclear modification factors of non-photonic electrons (NPE) from heavy-quark decays at high p_t show a suppression level similar

---

[18]The Okubo-Zweig-Iizuka (OZI) rule states that processes with disconnected quark lines in the initial and final state are suppressed.

[19]Quark coalescence is a simple model of hadronization where all quarks and antiquarks present in the quark matter at the latest stage of its evolution are redistributed between colour-singlet final states (hadrons).
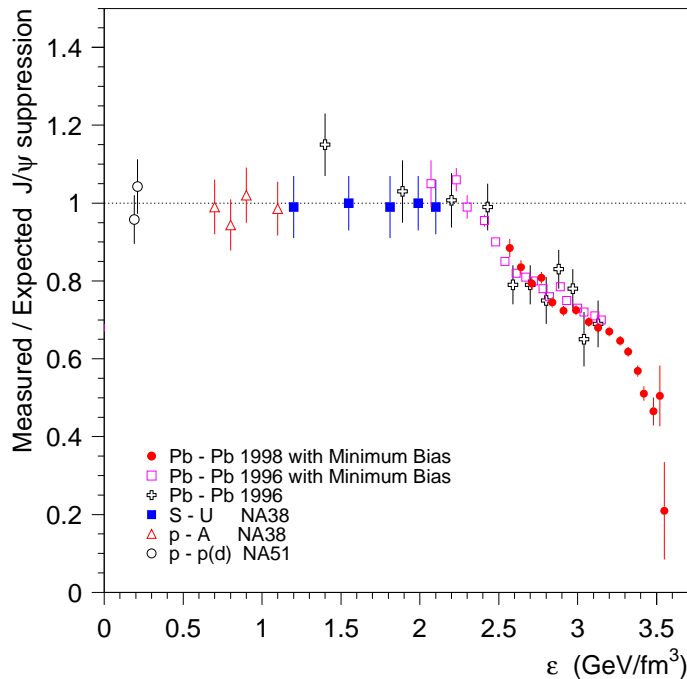
Figure 1.7: Measured J/ψ production yields at SPS, normalized to the yields expected assuming that the only source of suppression is the ordinary absorption by the nuclear medium. The data is shown as a function of the energy density reached in the several collision systems.

to light hadrons [63, 64], indicating substantial energy loss of heavy quarks. This observation renews the interest in heavy-quark production and their interaction with the hot and dense matter produced in relativistic heavy-ion collisions.

Heavy quarks provide sensitive probes of the collision dynamics at both short and long timescales. Heavy-quark production is an intrinsically perturbative phenomenon which takes place on timescales of the order of $1/m_q$, where m_q is the heavy-quark mass. On the other side, the long lifetime of charm and bottom quarks allows them to live through the thermalization phase of the plasma and to possibly be affected by its presence. In addition, the high temperature of the produced plasma may give rise to thermal production of heavy-quark pairs. Measurements of charm and bottom pro-
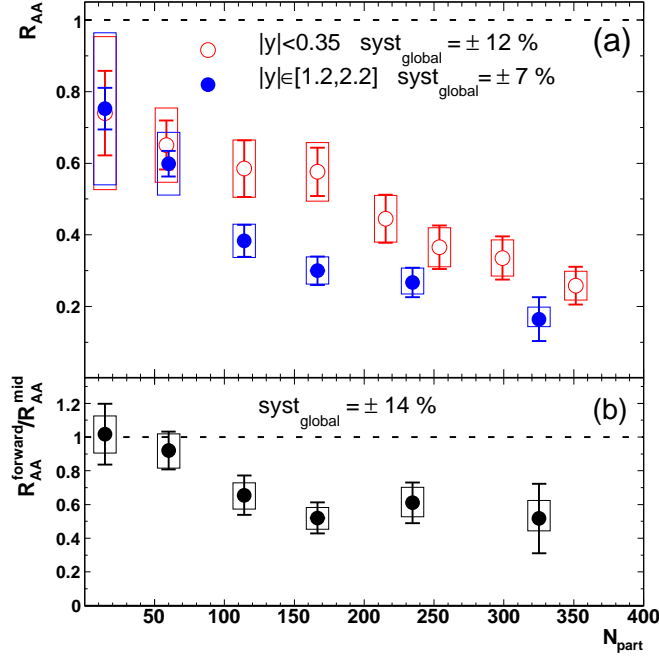
Figure 1.8: (a) J/ψ R_{AA} vs. N_{part} for Au–Au collisions, as measured at RHIC by PHENIX. Mid (forward) rapidity data are shown with open (filled) circles. (b) Ratio of forward/mid rapidity J/ψ R_{AA} vs. N_{part}.

duction at low p_t probe the QCD medium at thermal scales and are thus sensitive to bulk medium properties like density and viscosity.

Heavy-quark production is of crucial importance to understand the production of quarkonium states. The total charm production cross section is an important input in models of statistical J/ψ production via charm quark coalescence in a Quark-Gluon Plasma [65–70]: an additional production of $c\bar{c}$ pairs in the plasma will enhance the chance of J/ψ formation.

The suppression of the charmonium states by colour screening has been predicted as one of the most interesting signatures of the formation of a deconfined state of quarks and gluons in high-energy heavy-ion collisions [71]. The idea is that the initially formed $c\bar{c}$ pair would be unable to form a J/ψ resonance in a QGP medium because of the screening of the confining potential. Lattice-based potential models indicate that the dissociation temperature for J/ψ is $T_{J/\psi} \approx 2.1 T_c$, while the excited states χ_c and ψ' are dissolved

close to the critical temperature $T_{\chi_c} \approx 1.2 T_c$, $T_{\psi'} \approx 1.1 T_c$ [72]. Moreover, the detection of J/ψ and ψ' mesons through their leptonic decay to a pair of muons is particularly interesting since muons are not affected by the strong interactions in the later stages of the collision evolution.

The analysis of the Pb–Pb data collected by the NA50 experiment [73] at CERN-SPS first showed [74–76] that the J/ψ production yield, with respect to the production of Drell-Yan dimuons, is suppressed. In particular, NA50 has observed that below a certain centrality threshold the J/ψ production is well described invoking nuclear absorption as the only suppression mechanism [77, 78]; on the contrary, above that threshold, an extra suppression known as "anomalous" suppression sets in (Figure 1.7). The NA60 experiment [79] has observed similar behavior in In–In collisions at the same energy (158 GeV/nucleon) [80]. On the contrary, models which describe the low-energy J/ψ data at SPS invoking only J/ψ destruction based on the local medium density would predict a significant larger suppression at RHIC and more suppression at mid rapidity than at forward rapidity [81, 82]. Recently published high-statistics Au–Au data by PHENIX[20] experiment [83] at RHIC [84, 85] contradict both trends: the suppression of J/ψ at mid-rapidity is very similar to that observed by NA50 in Pb–Pb collisions at over an order of magnitude lower collision energy, and the suppression is larger at forward rapidity ($1.2 < |y| < 2.2$) than at mid-rapidity ($|y| < 0.35$). Both of these observations contradict the simple prediction of increasing suppression with increasing local energy density (Figure 1.8 shows the J/ψ nuclear modification factor R_{AA}[21] as a function of collision centrality).

1.2.5   Fluctuations

Any physical quantity measured in an experiment is subject to fluctuations which, in general, depend on the properties of the system under study.

---

[20] The Pioneering High Energy Nuclear Interaction eXperiment (PHENIX) at RHIC.

[21] The nuclear modification factor in a given centrality, p_t and y bin is:

$$R_{AA} = \frac{d^2 N_{J/\psi}^{AA}/dp_t dy}{N_{coll} d^2 N_{J/\psi}^{pp}/dp_t dy} \tag{1.12}$$

with $d^2 N_{J/\psi}^{AA}/dp_t dy$ being the J/ψ yield in Au–Au collisions in the centrality bin, N_{coll} the corresponding mean number of binary collisions and $d^2 N_{J/\psi}^{pp}/dp_t dy$ the J/ψ yield in elastic pp collisions.

Fluctuations may reveal important insight into the system itself. The most efficient way to address fluctuations of a system created in heavy-ion collision is via the study of event-by-event fluctuations: a given observable is measured on a event-by-event basis and the fluctuations of that observable are studied over an ensemble of events. Large-acceptance detectors allow one for a detailed analysis of individual collisions. Due to the hundreds or even thousands of particles produced in these collisions statistical methods can be applied.

In the framework of statistical physics, fluctuations measure the so-called susceptibility of a system which determines the response of the system to external forces[22]. Fluctuations allow to gain access to fundamental properties of the system just like in the experiments which deal with macroscopic quantities. In general fluctuations may reveal information well beyond the thermodynamic properties of a system: as the system expands, fluctuations may have been frozen earlier, thus providing information about how the system was looking like before its thermal freeze-out set in. A beautiful example comes from astrophysics: fluctuations in the cosmic wave background radiation, first observed by COBE[23].

In heavy-ion collisions fluctuations of transverse momentum and charge have been studied so far. The former should be sensitive to temperature–energy fluctuations [87–89] which in turn provide a measure of the heat capacity of the system

$$\langle (\delta T)^2 \rangle = \langle T^2 \rangle - \langle T \rangle^2 = \frac{T^2}{C_V}. \tag{1.13}$$

The QCD phase transition is associated with a maximum of the specific heat therefore temperature fluctuations should exhibit a minimum.

Charge fluctuations [90, 91] are sensitive to fractional charges carried by the quarks. If an equilibrated partonic phase forms after heavy-ion collisions the charge fluctuation per entropy would be about a factor 2 or 3 smaller than in a hadronic scenario. Fluctuation of the ratio of positively to negatively

---

[22]For example, by measuring the fluctuations of the net electric charge in a given rapidity interval one obtains information on how the system (or subsystem) would react to the application of an external (static) electrical field.

[23]NASA's COBE (Cosmic Background Explorer) [86] satellite was developed to measure infrared and cosmic microwave background radiation from the early Universe. COBE was launched on November 18, 1989.
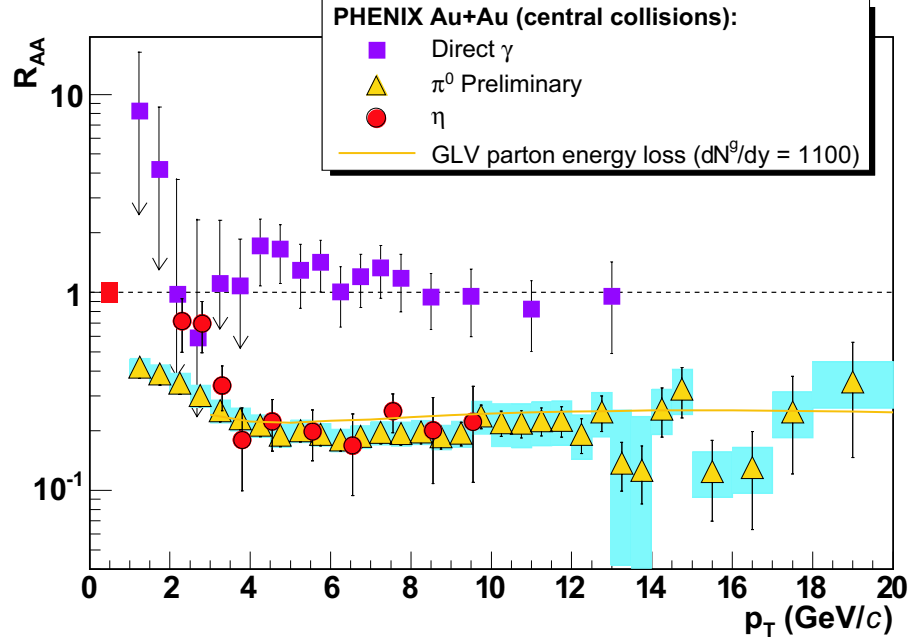
Figure 1.9: Nuclear modification factor R_{AA} from Eq. 1.15 of π^0 (triangles), η (circles) and direct photons (squares), as measured by PHENIX.

charged particles has been proposed as one observable

$$\left\langle \left(\delta \frac{N^+}{N^-} \right) \right\rangle \simeq 4 \frac{\langle (\delta Q)^2 \rangle}{\langle N_{ch} \rangle} \sim \frac{\langle (\delta Q)^2 \rangle}{S}. \tag{1.14}$$

Accounting for the fractional charge of the quarks, the variance of the ratio of positive and negative particles scaled by the total charged-particle multiplicity should be approximatively four times smaller than for a hadron gas. This prediction relies on the notion that quark–quark correlations can be neglected. However, they may be not negligible.

1.2.6 High-p_t and jet suppression

In 1982 Bjorken stated that a "high-p_t quark or gluon might lose tens of GeV of its initial transverse momentum while plowing through quark-gluon plasma produced in its local environment" [92]. Hard partons traversing the hot and dense medium created in heavy-ion collisions lose energy by
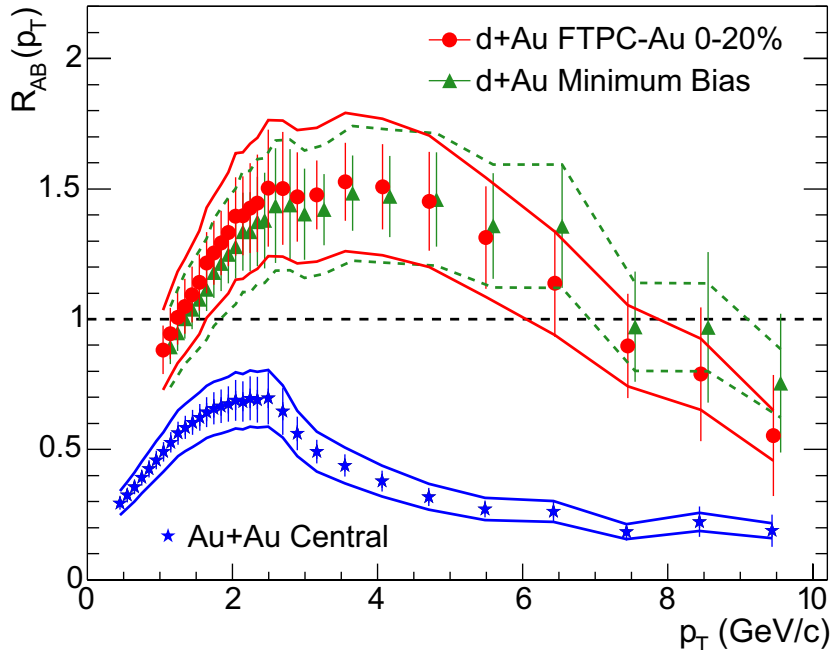
Figure 1.10: $R_{AB}(p_t)$ from Eq. 1.15 for minimum-bias and central d–Au collisions, and central Au–Au collisions, as measured by STAR. The minimum-bias data d–Au are displaced 100 MeV/c to the right for clarity.

gluon radiation and/or colliding elastically with surrounding partons [93, 94]. This would have many observable consequences, of which the most directly measurable would be a depletion in the yield of high-p_t hadrons [95–97].

When a high-energy parton traverses a length L of hot or cold matter, the induced radiative energy loss is proportional to L^2. The energy loss of a high-energy jet in a hot QCD plasma appears to be much larger than in cold nuclear matter even at moderate temperatures of the plasma $T \sim 200$ MeV [97]. The order of magnitude of the effect in hot matter compared to the case of cold nuclear matter may be expected to be large enough to lead to an observable and remarkable signal of Quark-Gluon Plasma production. Indeed, it has been proposed to measure the magnitude of "jet-quenching" in the transverse momentum spectrum of hard jets produced in heavy-ion collisions, comparing suppression and change of shape of the jet spectrum with hadron data.

One of the most exciting results to date at RHIC is that the yield of π^0
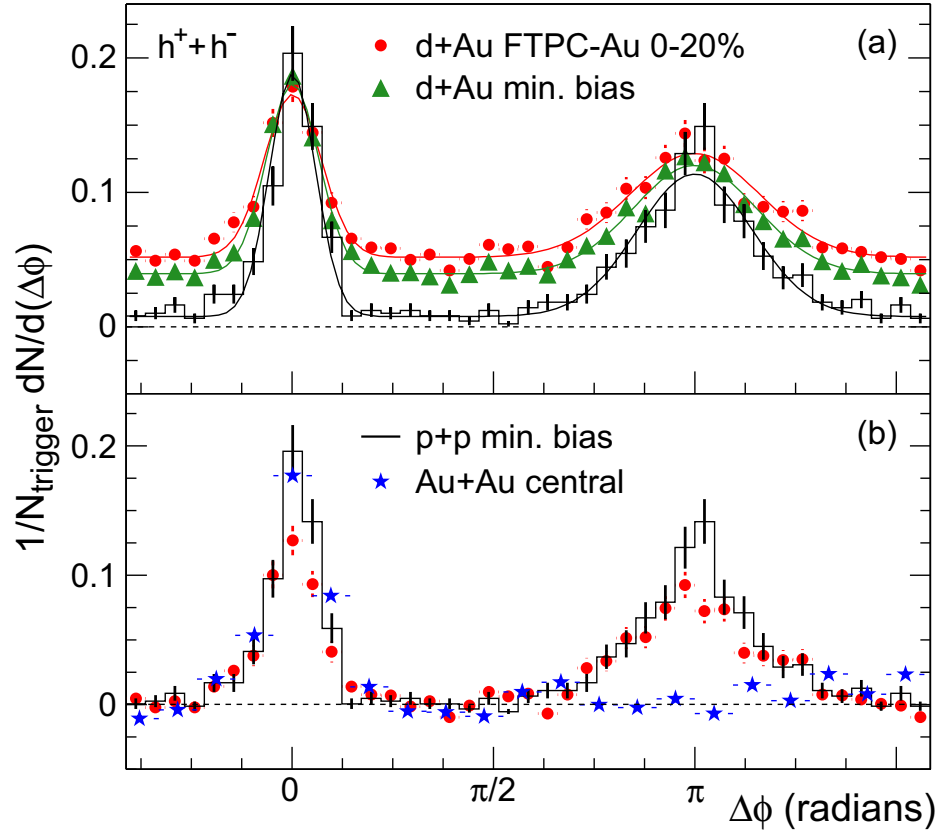
Figure 1.11: (a) Two-particle azimuthal distribution for minimum-bias and central d–Au collisions, and for pp collisions, as measured by STAR. (b) Comparison of the two-particle azimuthal distribution for central d–Au collisions to those seen in pp and central Au–Au collisions.

at high transverse momentum in central $\sqrt{s_{NN}} = 200$ GeV Au–Au collisions is suppressed compared to the yield in pp collisions scaled by the number of underlying nucleon–nucleon collisions [98–100] (Figure 1.9). The observation that single-particle inclusive spectra in d–Au collisions at the same energy are not suppressed demonstrate that the strong suppression of the inclusive yield observed in central Au–Au collisions is due to final-state interactions with the dense medium generated in such collisions [101] (Figure 1.10). The phenomenon is interpreted as a consequence of the jet-quenching effect. Nuclear effects on hadron production in d–Au and Au–Au collisions are measured through comparison to the pp spectrum using the ratio

$$R_{AB}(p_t) = \frac{d^2N/dp_t d\eta}{T_{AB} d^2\sigma^{pp}/dp_t d\eta}, \qquad (1.15)$$

where $d^2N/dp_t d\eta$ is the differential yield per event in the nuclear collision A–B, $T_{AB} = \langle N_{bin}\rangle/\sigma^{pp}_{inel}$ describes the nuclear geometry, and $d^2\sigma^{pp}/dp_t d\eta$ for pp inelastic collisions is determined from the measured pp differential cross section.

A hard hadronic collision at high energy may be pictured in the following way: partons distributed in the projectiles are involved in a hard scattering, with a large transfer of energy-momentum, whereas the non-colliding remnants of the incoming hadrons initiate what is called the "underlying event". The energetic coloured partons produced by the hard subprocess undergo a cascade of branchings which degrade their energies and momenta. Finally the end points of this branching process and the remnants of the incoming projectile fragment into colourless hadrons during the hadronization stage. The hadronic final state may be partitioned in clusters of hadrons, called "jets"[24].

Measurements of two-hadron angular correlations at large transverse momentum for pp and Au–Au collisions provide the most direct evidence for production of jets in high-energy nucleus–nucleus collisions, and allow measurements, not accessible in inclusive spectra, of the fate of the back-to-back jets in the dense medium. Partons fragment into jets of hadrons in a cone around the direction of the original hard-scattered parton. The leading hadron in the jet tends to be most closely aligned with the original parton direction. Since

---

[24]The jet definition gives the rule for the clustering of hadrons and assigns a transverse energy E_t, a pseudorapidity η and an azimuthal angle ϕ to each jet. In this way it is possible to trace back through the showering and hadronization stages to the hard partons.
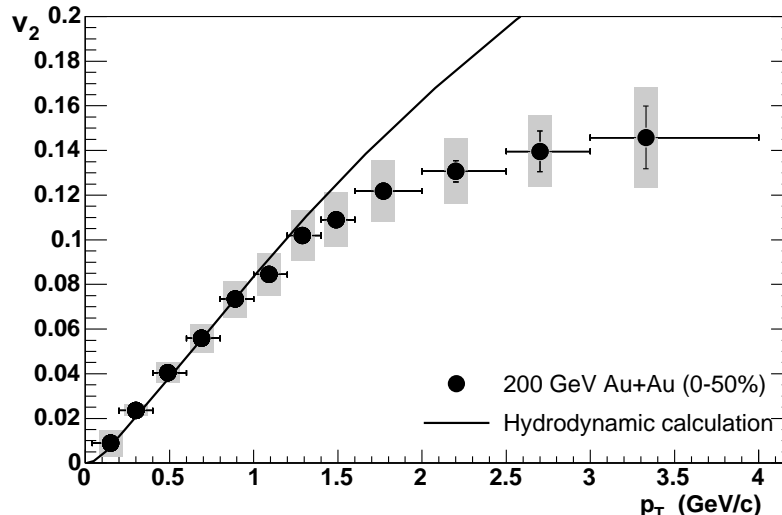
Figure 1.12: Elliptic flow as a function of transverse momentum $v_2(p_t)$ for Au–Au collisions and hydrodynamic calculation.

the large multiplicities in high-energy heavy-ion collisions make full jet reconstruction impractical, the method of two-particle azimuthal correlation of high-p_t hadrons is used to identify jets on a statistical basis [102]. Clear correlation peaks are observed near $\Delta\phi \sim 0$ and $\Delta\phi \sim \pi$ in pp and d–Au data, while the disappearance of back-to-back $\Delta\phi \sim \pi$ high-p_t hadron correlation in central Au–Au collisions (Figure 1.11) seems to be consistent with large energy loss in a system that is opaque to the propagation of high-momentum partons or their fragmentation products [101, 103].

1.2.7 Collective phenomena

Azimuthal anisotropies of hadron spectra are a good measure of collective behaviour of the dense particle system formed in the ultrarelativistic heavy-ion collisions [104]. The origin of such anisotropies is thought to be the rescattering among the particles, which are initially produced in isotropic partonic interactions. Important insights into the evolution of the created system may be obtained from the study of these azimuthal anisotropies, most of which are believed to originate in the early stages of the collision processes. Large anisotropies may indicate strong collective behaviour which in turn is argued to be indicative of early local thermal equilibrium.
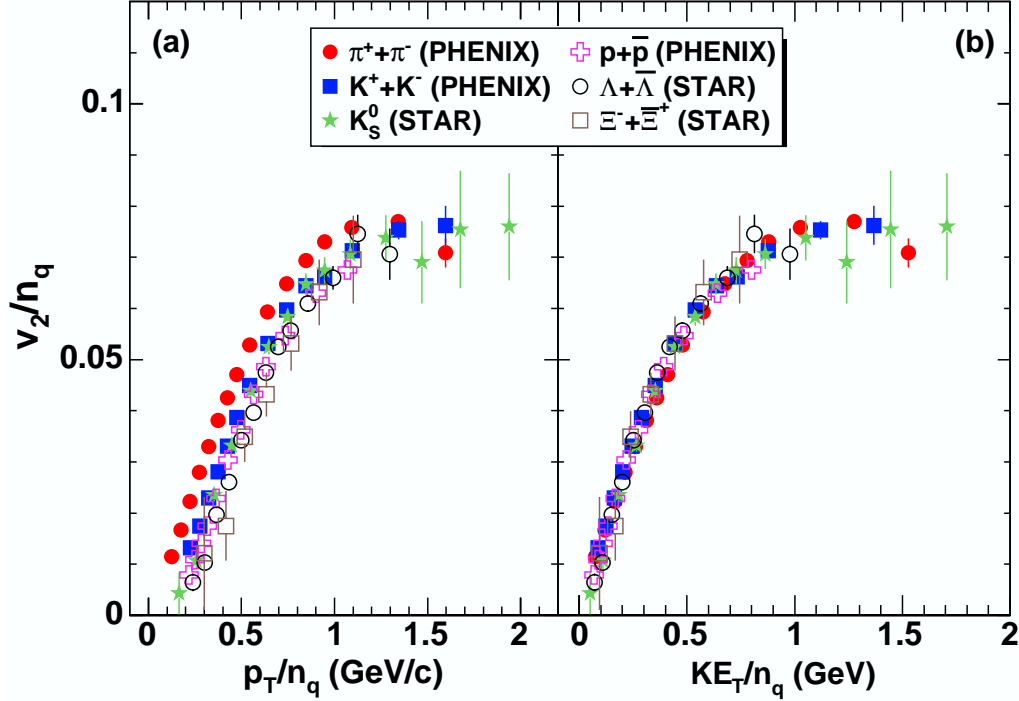
Figure 1.13: (a) v_2/n_q vs. p_t/n_q and (b) v_2/n_q vs. KE_t/n_q for identified particle species in minimum-bias Au–Au collisions at RHIC.

In the "standard method" to study azimuthal anisotropies of hadron spectra one estimates the "reaction plane", which is spanned by the vector of the impact parameter and the beam direction. Its azimuth is given by Ψ_{RP}. The particle azimuthal distribution measured with respect to the reaction plane is not isotropic; so it is customary to expand it in a Fourier series [105]:

$$E\frac{d^3N}{d^3p} = \frac{1}{2\pi}\frac{d^2N}{p_t dp_t dy}\left(1 + \sum_{n=1}^{\infty} 2v_n \cos[n\left(\phi - \Psi_{RP}\right)]\right), \qquad (1.16)$$

where the $v_n = \langle\cos[n(\phi_i - \Psi_{RP})]\rangle$ coefficients are used for a quantitative characterization of the event anisotropy, and the angle brackets mean an average over all particles in all events. The sine terms are not present because of symmetry with respect of the reaction plane. v_1 is referred to as "direct flow", and v_2 as "elliptic flow".

At RHIC energies, there is now significant evidence that elliptic flow, in

26

non-central collisions, results from hydrodynamic pressure gradients developed in a locally thermalized "almond-shaped" collision zone. That is, the initial transverse coordinate-space anisotropy of this zone is converted, via particle interactions, into an azimuthal momentum-space anisotropy. Indeed, when plotted as a function of the transverse kinetic energy $KE_t \equiv m_t - m$ divided by the number of valence quarks n_q, of a given hadron ($n_q = 2$ for mesons and $n_q = 3$ for baryons), v_2/n_q shows universal scaling for a broad range of particle species [106, 107] (Figure 1.13). This has been interpreted as evidence that hydrodynamic expansion of the QGP occurs during a phase characterized by independent quasi-particles which exhibit the quantum numbers of quarks [107–111].

Hydrodynamics is a macroscopic approach to describe the dynamical evolution of the expansion stages of a heavy-ion collision. It is a phenomenological model that describes the evolution of thermodynamic fields like energy density, pressure, temperature and flow without introducing unknown microscopic parameters [112]. Hydrodynamic treatment requires a large, macroscopic system in local thermal equilibrium and an adiabatic expansion stage. The good agreement of hydrodynamic simulations and experimental data from RHIC points towards such rapid thermalization followed by a hydrodynamic expansion (Figure 1.12).

1.3   The ALICE experiment

ALICE [113–115] (A Large Ion Collider Experiment) is a general-purpose heavy-ion detector at the CERN LHC (Large Hadron Collider) [2] which focuses on QCD (Quantum Chromo-Dynamics), the theory of strong interactions of the Standard Model. The detector design has been chosen to address the physics of strongly-interacting matter and the Quark-Gluon Plasma (QGP) in nucleus–nucleus collisions at extreme values of temperature and energy density.

A unique design has been adopted for ALICE in order to fulfill the requirements to track and identify particles from very low (~ 100 MeV/c) up to quite high (~ 100 GeV/c) transverse momenta in an environment with large charged-particle multiplicities (up to 8000 charged particles per rapidity unit at mid-rapidity). Moreover, since the interaction rate with nuclear beams at LHC is low (10 kHz for Pb–Pb collisions) and radiation doses are

moderate, ALICE uses slow but high-granularity detectors which make the detector optimization differ substantially from the one selected for dedicated pp experiments at LHC. The tracking uses three-dimensional hit information with many points (up to 150) in a moderate magnetic field of 0.5 T. To measure particle momenta over such a broad momentum range a combination of very thin materials reduces the multiple scattering at low p_t while a large tracking lever arm of up to 3.5 m guarantees a good resolution at high p_t. Particle identification (PID) is essential, as many observables are either mass or flavour dependent. ALICE makes use of almost all known PID techniques: specific ionization energy loss, time-of-flight, transition and Cherenkov radiation, electromagnetic calorimetry, muon filters and topological decay reconstruction.

1.3.1   Detector layout

The ALICE experiment, shown in Fig. 1.14 and 1.15, consists of a central-barrel detector system and several forward detectors.

The central system, which covers the mid-rapidity region $|\eta| \leq 0.9$ over the full azimuthal angle, is installed inside a large solenoidal magnet which generates a magnetic field of ≤ 0.5 T. The central system includes, from the beam pipe to the outside, six layers of high-resolution silicon detectors (Inner Tracking System – ITS), the main tracking device of the experiment (Time-Projection Chamber – TPC), a transition-radiation detector for electron identification (Transition-Radiation Detector – TRD) and a time-of-flight detector for charged-hadron identification (Time-Of-Flight – TOF). The central system is complemented by three small-area detectors: an array of ring-imaging Cherenkov detectors for identification of high-momentum particles (High-Momentum Particle Identification Detector – HMPID), an electromagnetic calorimeter for photon and neutral-meson measurements (Photon Spectrometer – PHOS) and a second electromagnetic calorimeter to enhance the capabilities for measuring jet properties (Electromagnetic Calorimeter – EM-Cal).

The large-rapidity systems include a single-arm muon spectrometer covering the pseudorapidity range $-4.0 \leq \eta \leq -2.4$, a photon-counting detector (Photon Multiplicity Detector – PMD), a silicon detector to measure particle multiplicity in the forward region (Forward Multiplicity Detector – FMD) and two sets of neutron and proton calorimeters, located at 0° about 116 m
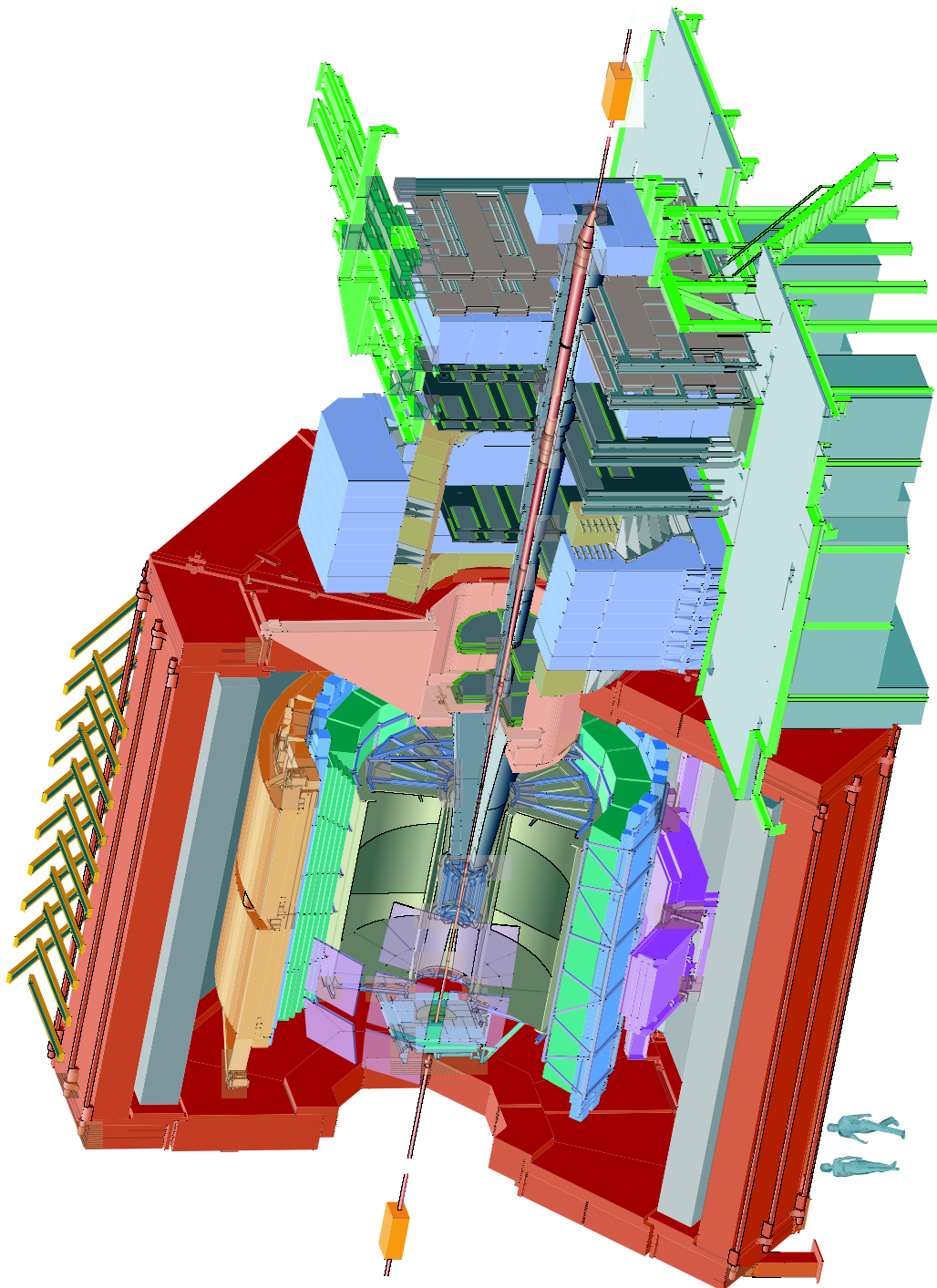
28

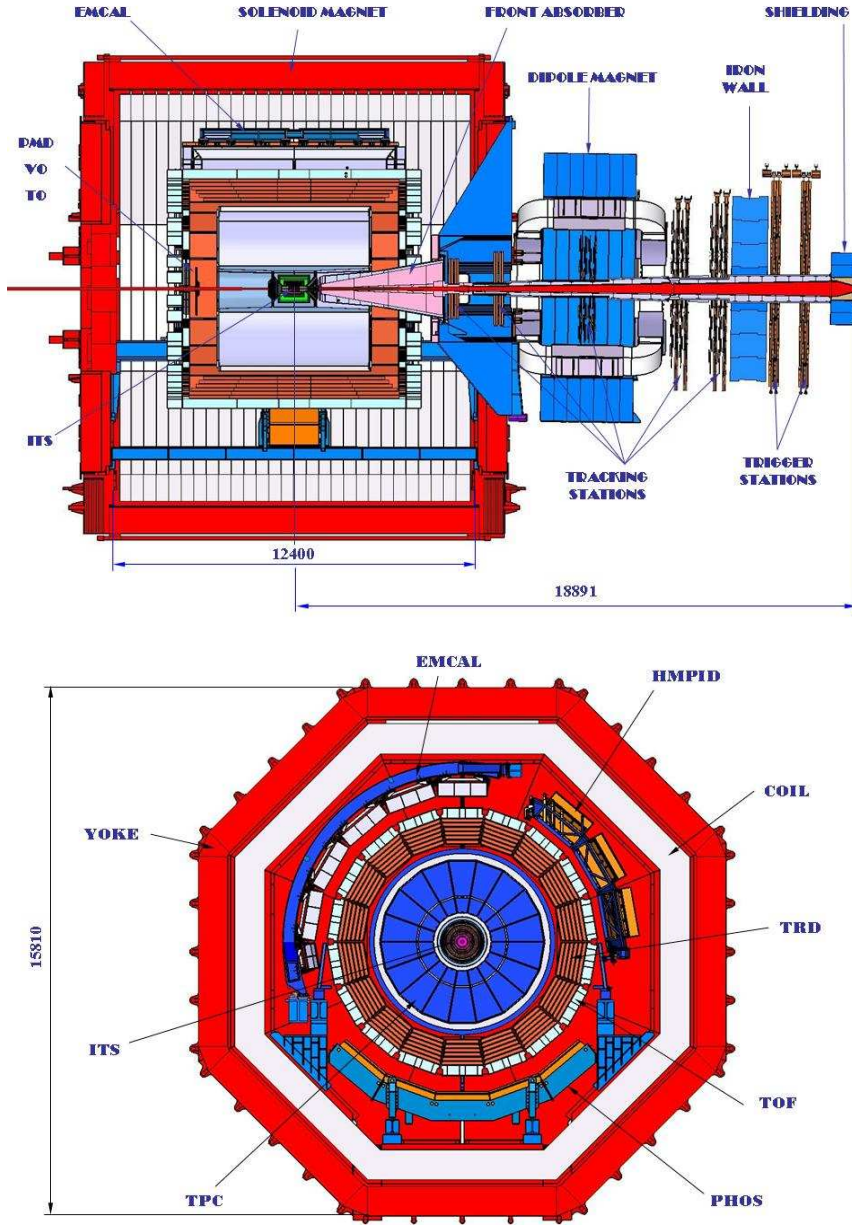**Figure 1.14:** Schematic layout of the ALICE detector.

Figure 1.15: ALICE 2-D cut views along the yz direction (upper part) and along the xy direction (lower part).

from the interaction point, to measure the impact parameter in nucleus–nucleus collisions (Zero-Degree Calorimeter – ZDC). In addition the forward region is instrumented with a system of Cherenkov counters to provide the event time (T0) and with two arrays of segmented scintillator counters used for minimum-bias trigger and beam–gas background rejection (V0).

An array of 60 large scintillators is installed on top of the magnet to provide a cosmic-ray trigger for calibration and alignment purposes as well as for cosmic-ray physics (ACORDE).

1.3.2   Magnets

The ALICE experiment uses two magnets. The L3 solenoid magnet, which encloses the central part of the detector, is a room-temperature solenoid constructed for the L3 experiment at LEP[25] [116]. The nominal field of the solenoid is 0.5 T and the field variations in the volume of the detectors are below 2%, better compared to L3 situation thanks to the achieved improvements to the field homogeneity.

A dipole magnet [117] with resistive coils and a horizontal field perpendicular to the beam axis is also used, as an integral part of the muon-spectrometer arm. The nominal magnetic field and the field integral are of 0.67 T and 3 Tm respectively.

1.3.3   Tracking detectors

Inner Tracking System (ITS)

The Inner Tracking System (ITS) [113, 118] surrounds the 800 μm-thick beryllium beam pipe of ALICE. It consists of six concentric layers of silicon detectors (Figure 1.16) located between 4 cm and 43 cm from the beam axis and covering the central rapidity region ($|\eta| \leq 0.9$). The main tasks of the ITS are:

- to localize the primary vertex with a resolution better than 100 μm;

- to reconstruct secondary vertexes from decays of hyperons and from the decay of D and B mesons;

---

[25]The magnet was put into operation in 1988 for the L3 LEP experiment.
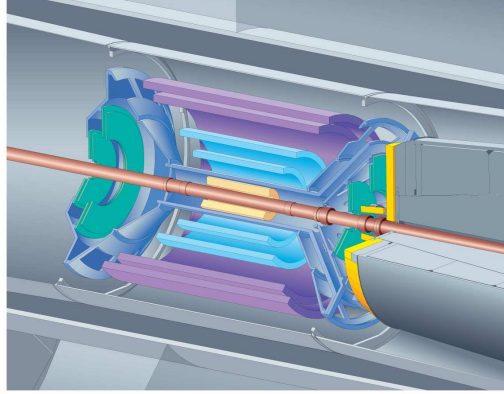
Figure 1.16: Schematic layout of the Inner Tracking System (ITS). From the beam pipe to the outside: SPD, SDD and SSD silicon detectors. The FMD (both sides of the ITS) and the front absorber (muon-spectrometer side) are also shown.

- to track and identify particles with momentum below 200 MeV/c;

- to improve momentum and angle resolution of high-p_t particles and to reconstruct particles crossing dead regions of the TPC.

The charged-particle density expected from LHC Pb–Pb collisions is high, therefore high-granularity devices have been chosen for the innermost layers of the ITS: two layers of Silicon Pixel Detectors (SPD) followed by two layers of Silicon Drift Detectors (SDD). At larger radii, where the requirements in terms of granularity are less strict, two layers of double-sided Silicon Strip Detectors (SSD) are used. The SDD and SSD detectors have analog readout and therefore can be used for particle identification at low momentum via the dE/dx measurement.

Time-Projection Chamber (TPC)

The Time-Projection Chamber (TPC) [113, 119] is the main tracking detector of the ALICE central barrel (Figure 1.17). Together with other
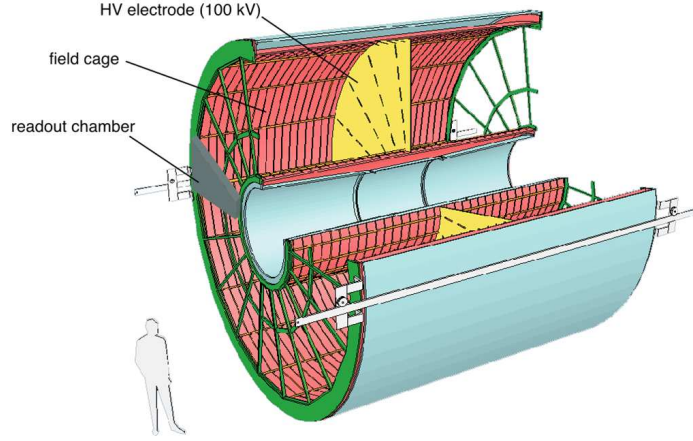
Figure 1.17: Schematic drawing of the Time-Projection Chamber (TPC).

central-barrel detectors the TPC has to provide charged-particle momentum measurements with good two-track separation, particle identification and vertex determination. The TPC covers the pseudorapidity range $|\eta| < 0.9$ over the full azimuthal angle with a good momentum resolution which ranges from low-p_t particles up to 100 GeV/c. The TPC is cylindrical in shape and it is the biggest TPC ever built. The active volume[26] has an internal radius of about 85 cm, an outer radius of about 250 cm and an overall length along the beam direction of 500 cm. The extremely high number of tracks which have to be reconstructed by the TPC has required a design which limits detector occupancy at the inner radius and at the same time guarantees good momentum resolution for high-p_t particles. The charge collected on TPC readout pads is used to measure particle specific energy loss and allows to evaluate the mean energy loss per path length (dE/dx). This information combined with particle momentum measurement yields the particle mass using the Bethe-Bloch formula in the low-momentum region[27] ($1/\beta^2$). Precise Monte Carlo simulations of the geometrical acceptance, detector efficiency

---

[26]The 90 m^3 TPC active volume is filled with a $Ne/CO_2/N_2$ (90%/10%/5%) gas mixture. The electron drift velocity of 2.7 cm/μs over 250 cm (the maximum drift length) fixes the maximum drift time of 92 μs which defines the rate capability of the TPC.

[27]The Bethe-Bloch equation

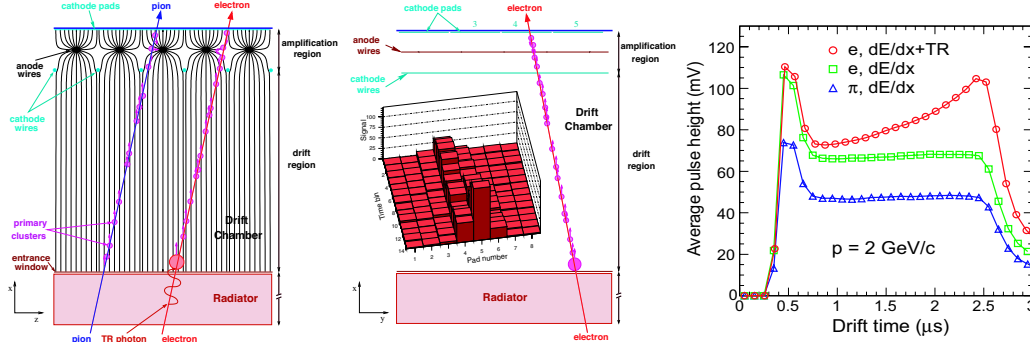$$dE/dx = C_1/\beta^2[\ln(C_2\beta^2\gamma^2) - \beta^2 + C_3] \tag{1.17}$$

Figure 1.18: Cross-sectional views of one TRD chamber and average signals. Ionizing radiation produces electrons in the gas. Particles exceeding the threshold ($\gamma \sim 1000$) produce also transition radiation.

and track-reconstruction algorithms foresee a charged-particle reconstruction efficiency better than 90% for the highest particle density.

1.3.4 Particle identification detectors

Transition-Radiation Detector (TRD)

The Transition-Radiation Detector (TRD) [113, 120] has the main task to provide electron identification in the ALICE central barrel for particle momenta greater than 1 GeV/c. Electrons with momentum above this value radiate transition radiation[28] which can be exploited to extend the pion-

---

with $\gamma = 1/\sqrt{1 - \beta^2}$ and detector-specific constants C_1, C_2 and C_3, relates the mean energy loss per path length dE/dx to the velocity β of the particle.

[28]Transition radiation is produced by relativistic charged particles ($\gamma \gtrsim 1000$) when they cross the interface of two media of different dielectric constant. Photons are emitted in the keV range with typical energy

$$\hbar\omega \approx \frac{1}{4}\hbar\omega_p\gamma, \tag{1.18}$$

where ω_p is the plasma frequency

$$\omega_p = \sqrt{\frac{n_e e^2}{\varepsilon_0 m_e}} \tag{1.19}$$

and n_e is the electron density.

rejection capability of the TPC to higher momenta. Furthermore, the TRD provides tracking information with a larger tracking lever arm, thus improving momentum resolution at high p_t. These features allow the reconstruction in the central region of light and heavy vector-meson resonances in the e^+e^- channel in pp collisions as well as in Pb–Pb collisions.

The detector covers the full azimuth of the mid-rapidity region ($-0.84 < \eta < 0.84$) from 2.90 m to 3.68 m from the interaction vertex. The TRD is made of 540 modules arranged in 18 super-modules around the beam pipe. Each module consists of a radiator 4.8 mm thick, a drift section 30 mm long and a multi-wire proportional chamber section of 7 mm with readout pads (Figure 1.18). A Xe/CO_2 (85%/15%) gas mixture fills the gas volume of the detector. The detector can derive a fast trigger for high-momentum charged particles and it contributes to the Level-1 trigger of ALICE.

Time-Of-Flight detector (TOF)

The Time-Of-Flight detector (TOF) [113, 121, 122] covers with a large cylindrical array (~ 170 m^2) the central region ($-0.9 < \eta < 0.9$) and provides charged-particle identification in the intermediate momentum range. With a global time resolution of 80 ps the system is expected to provide π/K and K/p separation better than 3σ up to a particle momentum $p \simeq 2.5$ GeV/c and $p \simeq 4$ GeV/c respectively. The active element is the double-stack Multigap Resistive Plate Chamber (MRPC) [123] strip operated in a $C_2H_2F_4$ (90%), i-C_4H_{10} (5%), SF_6 (5%) gas mixture. To guarantee low detector occupancy even in the highest charged-particle density scenario ($dN_{ch}/d\eta = 8000$) the MRPC strip is segmented into two rows of 48 pickup pads of 3.5×2.5 cm^2, for a total of about 160000 readout channels.

A comprehensive review of the Time-Of-Flight detector of ALICE will be given in Chapter 2.

High-Momentum Particle Identification (HMPID)

As the name suggests, the aim of the High-Momentum Particle Identification Detector (HMPID) [113, 124] is to enhance the particle-identification capabilities of ALICE at high p_t, extending the useful range for π/K and K/p separation up to 3 GeV/c and 5 GeV/c respectively. It is particularly dedicated to inclusive measurements of identified hadrons for $p_t > 1$ GeV/c.
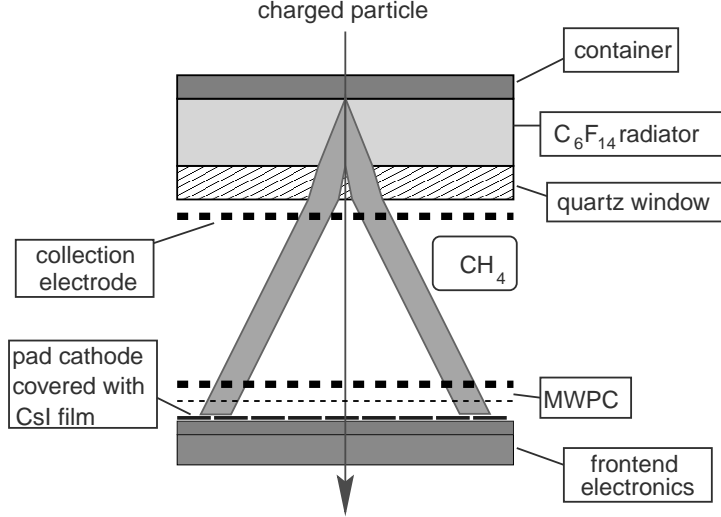
Figure 1.19: Working principle of a RICH detector employing CsI thin films deposited onto the cathode plane of a MWPC. The Cherenkov light-cone produced by a particle above the threshold refracts out of the liquid radiator and expands in the proximity volume of CH_4 before reaching the MWPC photon detector.

The HMPID is based on proximity-focusing Ring Imaging Cherenkov (RICH) counters[29] (Figure 1.19) arranged in an array with an acceptance of 5% of the central barrel phase space (Figure 1.20). The radiator, which defines the momentum range sensitivity of the device, is a 15 mm thick layer of a liquid (perfluorohexane C_6F_14) with refraction index $n = 1.2989$[30]. The threshold for Cherenkov radiation production is $\beta_{th} = 0.77$ which corresponds to a particle threshold momentum of $p_{th} = 1.21m$, where m is the particle mass. Cherenkov photons are detected by a photon counter thanks to the

---

[29]Cherenkov radiation is emitted when a charged particle passes a dielectric medium with velocity

$$\beta \geq \beta_{thr} = \frac{1}{n}, \qquad (1.20)$$

where n is the refraction index of the medium. The photons are emitted at an angle

$$\cos \theta_c = \frac{1}{n\beta}. \qquad (1.21)$$

[30]Refraction index at $\lambda = 175$ nm.

novel technology based on a thin layer of CsI deposited on the pad cathode of a Multi-Wire Proportional Chamber (MWPC).

1.3.5   Electromagnetic calorimeters

Photon Spectrometer (PHOS)

The Photon Spectrometer (PHOS) [113, 125] is a high-resolution electromagnetic calorimeter. It will detect electromagnetic particles in a limited acceptance region at central rapidity to provide photon identification as well as neutral-meson reconstruction through the 2-photon decay channel. The main physics objectives are to measure direct photons resulting from the initial phase of Pb–Pb collisions and the study of jet-quenching through measurements of high-p_t π^0.

The PHOS is designed as a single-arm electromagnetic spectrometer consisting of 5 modules (Figure 1.21) each made of a highly-segmented calorimeter (PHOS) and a Charged Particle Veto (CPV) detector[31]. The high energy resolution and granularity, required to achieve π^0 identification via invariant-mass analysis of the decay photons, is provided by $22 \times 22 \times 180$ mm^3 lead-tungstate ($PbWO_4$, PWO) crystals of $20X_0$ with high photo-electron yield, coupled to 5×5 mm^2 Avalanche Photo-Diodes (APD) and low-noise amplifiers. To increase the light-yield of the PWO crystals the PHOS modules are operated at a temperature of $-25°$ C.

Electromagnetic Calorimeter (EMCal)

The construction of a large Electromagnetic Calorimeter (EMCal) [113, 126] has the aim to enable ALICE to explore in more details the physics of jet-quenching in heavy-ion collisions at LHC. The EMCal is a large Pb-scintillator sampling calorimeter[32] with cylindrical geometry. It covers $|\eta| < 0.7$ and $\Delta\phi = 107°$ at a radius of about 4.5 metres from the beam axis and it will be placed opposite in azimuth to the PHOS detector. The EMCal will provide a

---

[31]The Charged Particle Veto (CPV) detector is a Multi-Wire Proportional Chamber (MWPC) with charged-particle detection efficiency better than 99%. The CPV is placed on top of a PHOS module.

[32]The chosen technology is a layered Pb-scintillator sampling calorimeter with a longitudinal pitch of 1.44 mm Pb and 1.76 mm scintillator. Longitudinal wavelength-shifting fibers are used for light collection.
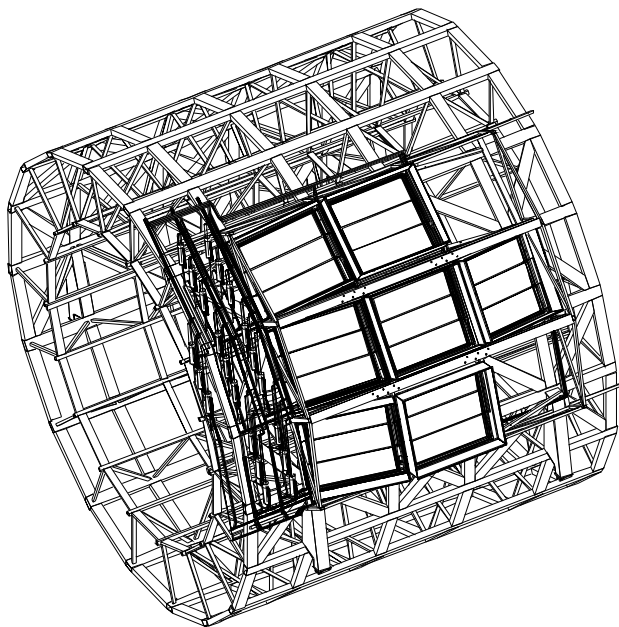
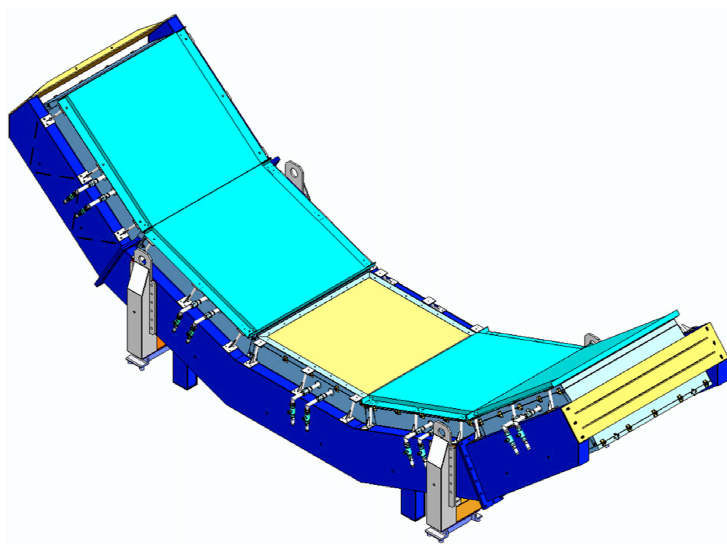**Figure 1.20:** Axonometric view of the HMPID in the space frame.

Figure 1.21: Schematic layout of the five PHOS modules inside the cradle.
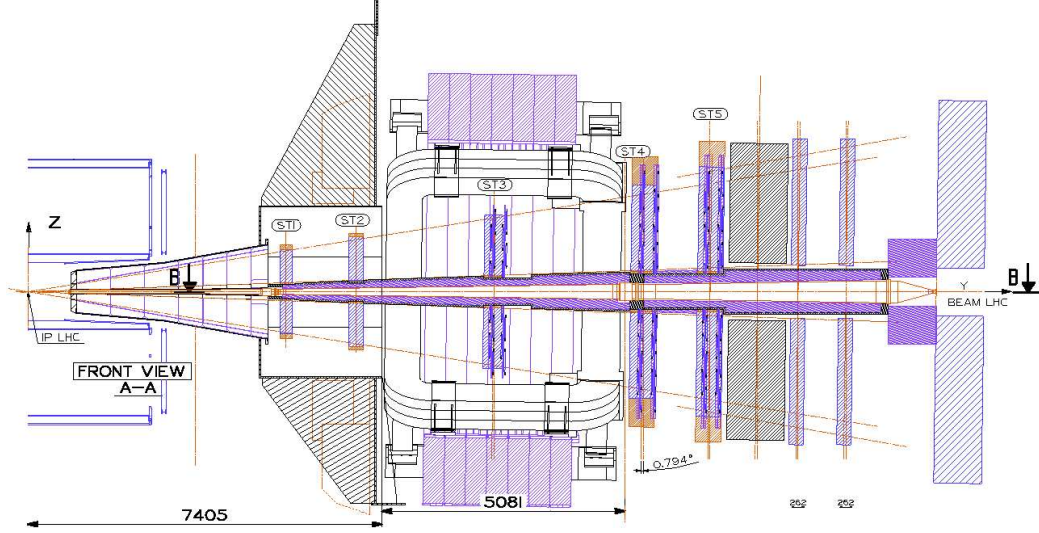
Figure 1.22: Layout of the Muon Spectrometer. The conical front absorber on the left is followed by 10 tracking stations: 4 placed between the absorber itself and the dipole magnet, two inside the magnet and four between the magnet and the muon-filter wall. Four planes of trigger chambers follow the muon filter.

fast and efficient trigger (Level-0 and Level-1) for hard jets allowing ALICE to fully exploit the LHC luminosity.

1.3.6 Muon spectrometer

The muon spectrometer [113, 127] is designed to detect muons in the pseudorapidity range of $-4.0 \leq \eta \leq -2.5$. It will allow to measure the complete spectrum of heavy-quark vector-mesons (i.e. J/ψ, ψ', Υ, Υ' and Υ'') and the lighter ϕ meson in the $\mu^+\mu^-$ decay channel. The simultaneous measurements of quarkonia species with the same apparatus allow direct comparisons of their properties (production rate, width) versus different global parameters such as collision centrality.

The spectrometer consists of the following components:

- a passive front absorber for hadrons and photons coming from the interaction region;

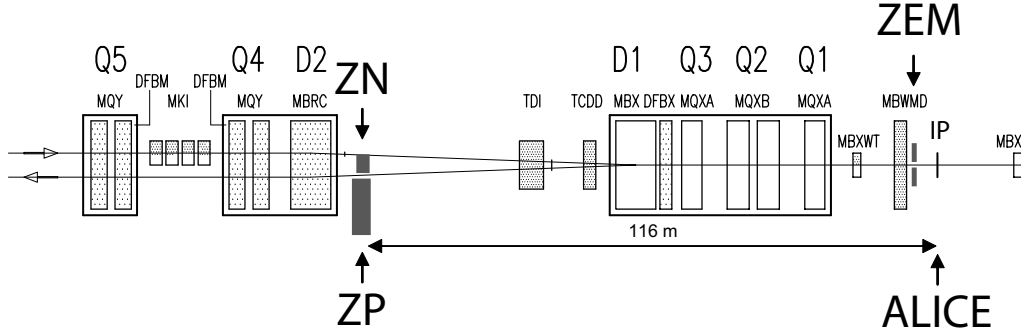- a high-granularity tracking system of 10 detection planes;

39

Figure 1.23: Schematic top view of the ALICE beam line opposite to the muon spectrometer. The locations of the neutron (ZN), proton (ZP) and forward electromagnetic calorimeters (ZEM) are shown.

- a large dipole magnet[33];

- a passive muon-filter wall, followed by four planes of trigger chambers;

- an inner beam shield to protect the chambers from particles and secondaries produced at large rapidity.

The 4.3 m long front absorber ($\sim 10\lambda_{int}$) is located inside the L3 magnet and it is made predominantly of carbon and concrete. The tracking chambers are designed to achieve 100 μm spatial resolution for an invariant-mass resolution of about (100 MeV/c^2) at the Υ mass. The muon-filter wall, that is an iron wall 1.2 m thick ($\sim 7.2\lambda_{int}$), provides additional protection for the trigger chambers[34] allowing only muons with momentum $p > 4$ GeV/c to reach them.

1.3.7 Forward and trigger detectors

Zero-Degree Calorimeter (ZDC)

In ALICE the Zero-Degree Calorimeter (ZDC)[113, 128] is composed of two sets of hadron calorimeters located at 116 m on either side of the Inter-

---

[33]See Section 1.3.2.
[34]Resistive Plate Chambers (RPC) operated in streamer mode.

action Point (IP) to measure event centrality in nucleus–nucleus collisions[35]. In addition two small electromagnetic calorimeters (ZEM, $7 \times 7 \times 20.4$ cm^3) are placed at about 7 m from the IP on both sides of the beam pipe, opposite to the muon spectrometer (Figure 1.23). Each ZDC set is made of two calorimeters: one for spectator neutrons (ZN, $7.04 \times 7.04 \times 100$ cm^3) and one for spectator protons (ZP, $12 \times 22.4 \times 150$ cm^3). Since spectator protons are spatially separated from neutrons by the beam magnetic elements, the ZP is placed externally to the ongoing beam line (on the side where positive particles are deflected) while the ZN is placed between the beam pipes at 0° with respect to the beam axis[36].

The hadronic ZDCs are quartz-fibre sampling calorimeters: the shower generated by incident particles in the absorber[37] produces Cherenkov radiation in the quartz fibres. The optical readout is divided into four independent towers. One out of two fibres is sent to a single photomultiplier (PMT), while the remaining ones are sent to the four PMTs which define the four towers. The ZEM[38] complements the hadronic ZDCs helping in discriminating between central and peripheral collisions. Since in very peripheral A–A collisions spectator nucleons can bound into fragments which stay in the beam pipes, they cannot be detected by the ZDCs. Therefore in very peripheral events only a small amount of energy is detected in the hadronic ZDCs, just like in central events, where the number of spectator nucleons is small. On the contrary the energy detected by the ZEM calorimeter increases monotonically with the collision centrality.

Photon Multiplicity Detector (PMD)

The Photon Multiplicity Detector (PMD) [113, 129, 130] will measure the multiplicity and the spatial distribution of photons in the forward rapidity region ($2.3 < \eta < 3.7$) to provide estimation of the collision reaction

---

[35]The number of participant nucleons is mostly related to the geometry of A–A collisions, that is the centrality. It can be estimated by measuring the energy carried by non-interacting (spectator) nucleons in the forward region (at 0° relative to the beam direction).

[36]Spectator protons and neutrons are no longer bounded to the collided nuclei. Protons are deflected by the LHC magnets while neutrons are not.

[37]Tungsten alloy and brass are used for the absorbers of ZN and ZP respectively.

[38]The detection technique is similar to the one used for the hadronic calorimeters. A lead-plate absorber is used with quartz fibres.
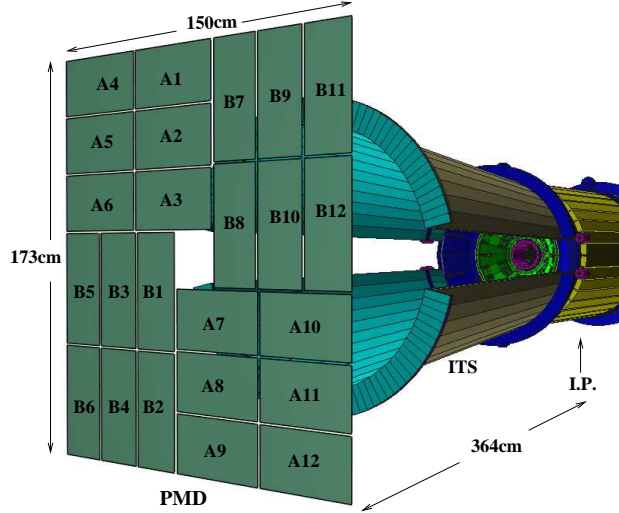
Figure 1.24: PMD position and layout in ALICE.

plane on an event-by-event basis (Figure 1.24). Because of the large particle density in the forward region, calorimetric techniques are not feasible. The method used for the PMD detector makes use of the preshower technique: a three radiation length thick converter is placed between two planes of gas proportional counters where the first plane is used as charged particle veto while the other one is used for photon identification.

Forward Multiplicity Detector (FMD)

The main task of the Forward Multiplicity Detector (FMD) [113, 131], shown together with ITS in Fig 1.16, is to measure charged-particle multiplicity in the forward region. It will cover the pseudorapidity range $-3.4 < \eta < -1.7$ and $-1.7 < \eta < 5.0$ with rings of silicon detectors placed in different positions from the interaction vertex. Two sets of two FMD rings are located on both sides of the ITS detector and have approximately the same acceptance. Another ring is placed farther from the interaction point.

V0 detector

The V0 detector [113, 131] is a small-angle detector consisting of two arrays of scintillator counters installed on either side of the ALICE interac-
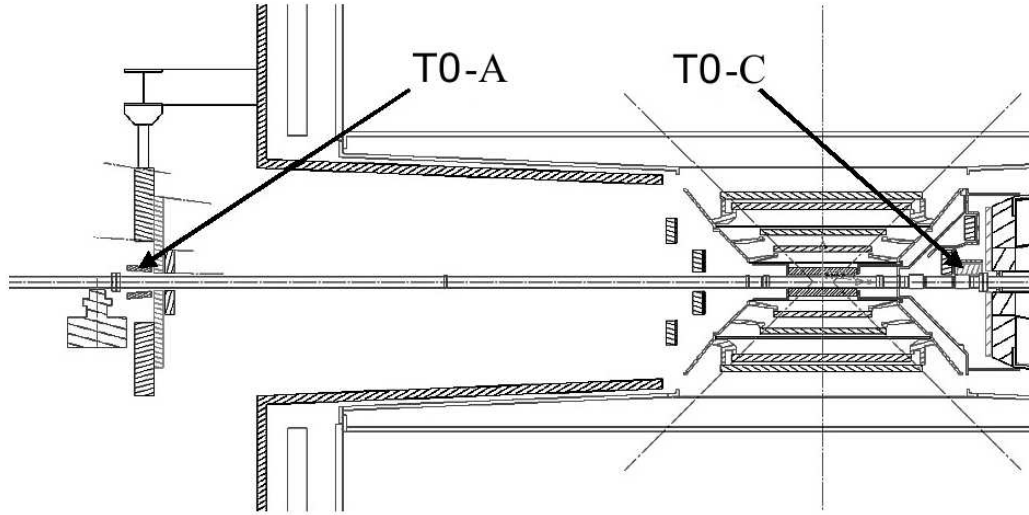
Figure 1.25: The layout of T0 detector arrays inside ALICE.

tion region. It will provide minimum-bias triggers for central-barrel detectors in both pp and nucleus–nucleus collisions and will help rejecting false events induced by interactions of protons with the residual gas of the vacuum chamber.

T0 detector

The T0 detector [113, 131] was designed to generate a start-time (T0) signal for the Time-Of-Flight (TOF) detector. This signal is independent of the vertex position and corresponds to the real time of the collision. The T0 detector can also measure the vertex position (with 1.5 cm precision) and provide Level-0 triggers when the position is within the preset value.

The detector consists of two arrays of Cherenkov counters, each with 12 counters. Each Cherenkov counter is based on a fine-mesh photomultiplier tube[39] coupled to a quartz radiator 20 mm in diameter and 20 mm thick. The two arrays are placed at 72.7 cm (T0-C) and 375 cm (T0-A) from the interaction point, respectively (Figure 1.25).

---

[39]A Russian made fine-mesh photomultiplier tube PMT-187, 30 mm in diameter, 45 mm long.

ALICE Cosmic-Ray Detector (ACORDE)

The ALICE detector is also instrumented with a cosmic-ray detector, ACORDE [113, 132, 133], an array of plastic-scintillator counters placed on the upper surface of the L3 magnet[40]. Together with some other ALICE detectors it will detect both single-muon and multi-muon events[41] (called muon bundles) thus providing precise information on cosmic rays with primary energy around 10^{15-17} eV, in the region of the knee of the cosmic-ray spectrum. Another major task of ACORDE is to provide Level-0 trigger signals for commissioning, calibration and alignment procedures of some of the ALICE central detectors.

A single ACORDE module consists of two 190×20 cm^2 scintillator counters 10 mm thick placed on top of each other and readout in coincidence by two PMTs at the end of each scintillator. A total of 60 modules are placed on top of the ALICE L3 magnet.

1.3.8   Data Acquisition and trigger system

Trigger system

The ALICE Central Trigger Processor (CTP) [113, 134] is designed to select events having a variety of different features at rates which can be scaled down to suit physics requirements and restrictions imposed by the bandwidth of the Data Acquisition (DAQ) system and the High-Level Trigger (HLT). The challenge of the ALICE trigger is to make optimum use of the detectors and to perform trigger selections in an optimized way for several different running modes[42].

The first response of the trigger system has to be fast to suit detector requirements. The "fast" part of the trigger is split into two levels: a Level-0 (L0) signal from CTP reaching the detectors after 1.2 μs and a Level-1 (L1) signal arriving after 6.5 μs. The L0 signal is too fast to enable the trigger inputs from all the detectors while the L1 signal can pick up all the remaining

---

[40]The available plastic material to build the array was previously used by the DELPHI experiment at LEP.

[41]The typical rate for single atmospheric muons reaching the ALICE detector is relatively low, being 4.5 Hz/m^2 on top of the magnet. The rate for multi-muon events is expected to be much lower, less than 10^{-3} Hz/m^2.

[42]The counting rate varies by almost two orders of magnitude for different running modes: nucleus–nucleus, pA and pp collisions.
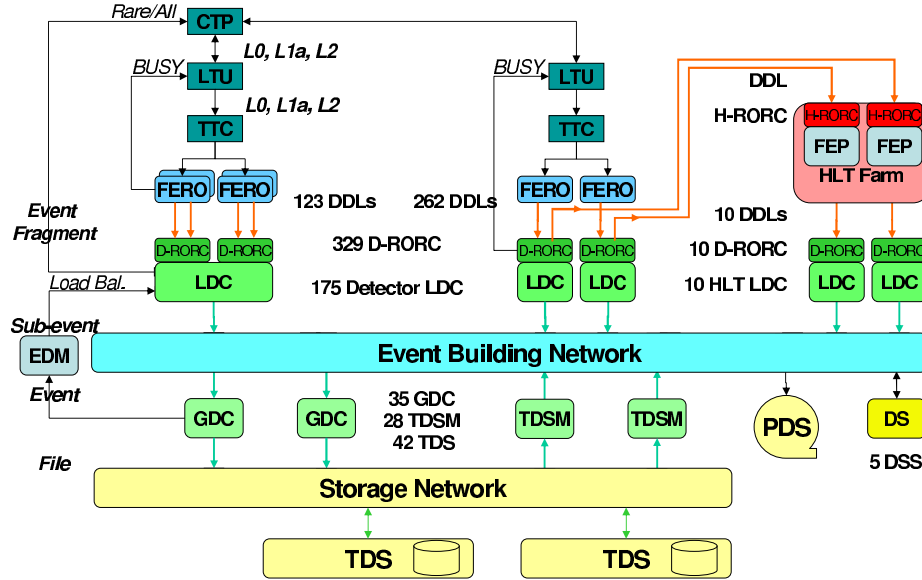
Figure 1.26: The overall architecture of the ALICE DAQ system and the interface to the HLT system.

fast inputs. CTP decisions are made in 100 ns. "Past-future" protection in ALICE avoids recording Pb–Pb collision events containing more than one central collision (the event reconstruction would not be possible in ALICE). A final level of trigger, Level-2 (L2), waits for the end of the past-future protection interval[43] (88 μs).

The CTP consists of seven different types of 6U VME boards housed in a single VME crate. The signal transmission to each detector is mediated by Local Trigger Units (LTU) which can be decoupled from the CTP for testing purposes[44].

Data Acquisition (DAQ)

The trigger and Data Acquisition (DAQ) systems of ALICE [113, 134] have been designed to give different observables a fair share of the trigger and

---

[43]This interval can also be used for running trigger algorithms.

[44]The ALICE LTUs can emulate CTP signals and trigger sequence. This feature allows testing and commissioning of detector electronics.

DAQ resources with respect to DAQ bandwidth. They have also to balance the capacity to record Pb–Pb central collisions (which generate large events) with the ability to acquire large fractions of rare events. To provide adequate physics statistics it has been estimated that a bandwidth of 1.25 GB/s to mass storage is suitable. This bandwidth is consistent with constraints imposed by technology, cost and storage capacity.

The architecture of the data acquisition is shown in Fig. 1.26. Detectors receive the trigger signals (and associated information) from CTP (Central Trigger Processor) through LTU (Local Trigger Unit). The data produced by the detectors (event fragments) are injected on the DDL (Detector Data Link) using the same protocol[45]. At the receiving end of the DDL, D-RORC (DAQ Readout Receiver Card) PCI-X based cards[46] receive and assemble the event fragments into sub-events in the LDCs (Local Data Concentrators). The role of the LDC is to ship the sub-events to a farm of machines (Global Data Concentrator, GDC) where the whole events are built. The GDCs feed the recording system which eventually records the events in the Permanent Data Storage (PDS).

High-Level Trigger (HLT)

The amount of data produced in the TPC alone in a single nucleus–nucleus collision has been estimated to be about 75 MB (assuming high charged-particle density $dN_{ch}/d\eta = 8000$ at mid-rapidity). The data rate can easily reach 25 GB/s while the DAQ archiving rate is about 1 GB/s. Therefore online processing is advisable to select relevant events and to compress data without loosing their physics content. The overall physics requirements of the High-Level Trigger [113, 134] (HLT) are the following:

- accept or reject events on a detailed online analysis;

- select a physics Region-Of-Interest (ROI) within the event;

- reduce the event size without loss of physics information of the accepted and selected data.

---

[45]The fact that all detectors use the DDL is one of the architectural features of the ALICE DAQ.

[46]The ALICE D-RORC PCI-X based receiving cards are hosted by front-end machines (commodity PCs) called LDCs (Local Data Concentrators). One LDC can handle one or more D-RORCs.

Chapter 2

The Time-Of-Flight detector

2.1 Design considerations

The Time-Of-Flight (TOF) detector of ALICE has been designed to identify charged particles produced in Pb–Pb collisions ($\sqrt{s} = 5.5$ TeV per nucleon pair) at the LHC. The TOF is located at 3.7 m from the beam axis and covers the pseudorapidity interval $|\eta| < 0.9$. With a magnetic field of 0.5 T the momentum threshold for particles to reach the TOF will be $p_{min} \sim 300$ MeV/c, being slightly higher for kaons and protons due to their larger energy loss at low momenta (~ 350 MeV/c and ~ 450 MeV/c respectively). With a global TOF time resolution of 80 ps the system is expected to provide a π/K and K/p separation better than 3σ up to a particle momentum $p \simeq 2.5$ GeV/c and $p \simeq 4$ GeV/c respectively.

Particle identification at low and intermediate momenta is of crucial importance in ALICE since the majority of the produced charged primary particles is emitted in this range. As an example, event-by-event hadron identification with a high statistics gives the opportunity to measure on a single-event basis production ratios and transverse-momentum spectra. In addition, reconstruction of particles and resonances via invariant-mass analysis of the decay products (i.e. $\phi \to K^+ K^-$, $D^0 \to K^- \pi^+$) is essential [59].

A large-coverage (141 m^2 active area) TOF detector was constructed with more than 10^5 independent channels to cope with the highest expected charged-particle density ($dN_{ch}/d\eta \sim 8000$). The required performance in terms of detection efficiency and time resolution has been obtained using as the basic detecting element the Multigap Resistive Plate Chamber (MRPC)
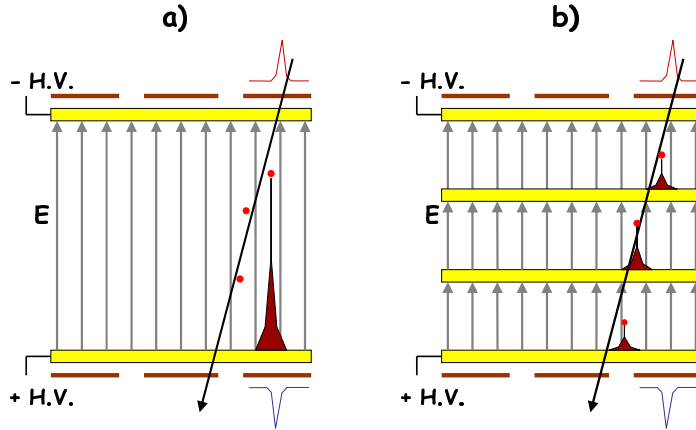
Figure 2.1: Schematic diagram and principle of operation of a multigap RPC (b) compared to a conventional single-gap RPC (a).

strip detector (Section 2.1.1 and 2.3.1). A solution based on fast scintillators and mesh photomultipliers would have been prohibitively expensive; so the choice was a gaseous TOF detector.

In the following sections the Multigap Resistive Plate Chamber technology and the particle-identification technique for a TOF detector are discussed. A description of the layout of the ALICE TOF detector is outlined in Section 2.3. In section 2.4 and 2.5 the electronics and services associated to the detector are presented.

2.1.1   The MRPC technology

In the framework of the LAA[1] project at CERN an intensive R&D[2] programme has led to the Multigap Resistive Plate Chamber [123] technology. A series of gas gaps with a single set of pickup pads reading out all gaps in parallel combines the advantages of a wide-gap RPC (high efficiency) with the better time-resolution performance of small-gap chambers (Figure 2.1).

A key issue in the operation of these detectors is the fact that the electric field is high and uniform and therefore the electrons produced by ionization start avalanching immediately; there is no drift time associated. There is

---

[1]The LAA project was a programme to develop new high-energy physics experimental techniques.

[2]Research and Development.

also a further advantage of subdividing the gas gap into many small gaps. A through-going particle produces individual and separate clusters of primary ionization; each of these clusters will start an avalanche and the final signal will be the sum of all avalanches. In a single-gap device, these avalanches are not independent and the resultant signal is as if there was only one large avalanche. On the contrary, for multigap chambers the signal is truly the sum of independent avalanches, since the avalanches occur in independent subgaps (Figure 2.1). Fluctuations within the avalanche mechanism dominate the single-gap behaviour while an average of many avalanches is the resultant signal in MRPCs.

Other main advantages of the MRPC technology are:

- the chamber operates at atmospheric pressure[3];

- the signal induced on the pickup electrodes by the movement of electrons and ions in the avalanche is the sum of the signals from all gaps. There is no late tail in the time response and the charge spectrum has a peak well separated from zero, thus the setting of the threshold is far less critical with respect to exponential-shaped charged spectra;

- the resistive electrodes quench streamers so that they do not initiate a spark breakdown; this allows for high-gain operation;

- the construction technique is rather simple and based on commercially available materials.

The Multigap Resistive Plate Chamber design used for the ALICE TOF detector is described in Section 2.3.1. This device, operated in a $C_2H_2F_4$/i-C_4H_{10}/SF_6 (90%/5%/5%) gas mixture, has demonstrated its excellent performance, with almost 100% efficiency and time resolution below 50 ps. The results obtained with a sample of the TOF MRPC mass production are presented in Section 3.1.3.

---

[3]With the Pestov [135] counter time resolution better than 50 ps was achieved with a 100 μm gas gap. However to reach high efficiency with such a small gap it is necessary to operate the chamber at more than 10 atm, which introduces important mechanical constraints.
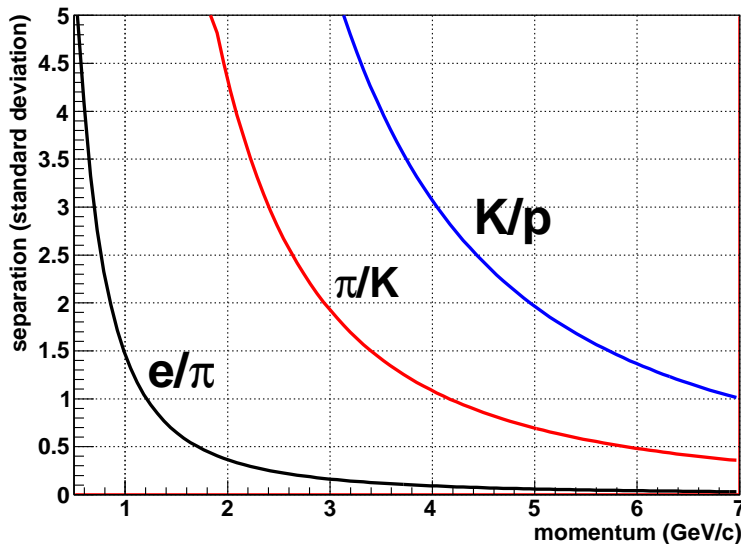
Figure 2.2: Particle identification capability a TOF detector with $\delta t = 80$ ps time resolution and particle track length $L = 3.7$ m. The number of standard deviations for e/π, π/K and K/p time difference are presented as a function of the particle momentum.

2.2 Particle Identification with the TOF detector

The identification of charged hadrons in ALICE is done combining the PID (Particle Identification) information provided by several detectors. The TOF detector is designed to identify charged particle at intermediate momenta using the Time-Of-Flight technique in the central rapidity region. Monte Carlo simulations of the apparatus confirm the good performance foreseen for such device.

2.2.1 The Time-Of-Flight technique

The identity of a particle can be only determined from its charge and mass. The particle charge can be directly measured, while particle mass cannot. The simultaneous and independent measure of two different kinematic

variables is needed, and one of them must depend on the particle mass.

Usually, in high-energy physics experiments particles are bent in a magnetic field to measure their momenta. Particle velocity measurement is often used together with momentum measurement for particle identification. Many techniques deal with particle velocity measurement, but the choice of the most suitable method is strongly related to the required momentum ranges. Particle identification using Cherenkov radiation detectors (i.e. differential Cherenkov detectors, Ring Imaging Cherenkov technique) works for sufficiently high momenta, when Cherenkov emission sets in. The Time-Of-Flight technique turns out to be well suited for particle identification in the mid-momentum region.

The Time-Of-Flight (TOF) technique is based on the measurement of the particle time-of-flight t over a known trajectory length L. This leads to the measurement of the particle velocity $v = L/t$. TOF measurements for particle identification require that the momentum of the particle p is also measured. The particle mass m is calculated using

$$m^2 = \frac{p^2}{c^2}\left(\frac{c^2 t^2}{L^2} - 1\right). \tag{2.1}$$

It is simple to show starting from this expression that mass resolution has three contributions:

$$\left(\frac{\delta m}{m}\right)_p = \frac{\delta p}{p}, \tag{2.2}$$

$$\left(\frac{\delta m}{m}\right)_L = \gamma^2 \frac{\delta L}{L}, \tag{2.3}$$

$$\left(\frac{\delta m}{m}\right)_t = \gamma^2 \frac{\delta t}{t}, \tag{2.4}$$

where

$$\gamma^2 = 1 + \frac{p^2}{m^2 c^2}. \tag{2.5}$$

Equation 2.4 and 2.5 show that particle identification using TOF measurements becomes worse as the square of the particle momentum: to achieve the same mass resolution at twice the momentum requires four-fold improvement in time resolution.

The time-of-flight difference for two particles of unequal mass m_1 and m_2 having the same momentum p and the same track length L is (in the limit $m^2 c^2 / p^2 < 1$)

$$t_1 - t_2 = \frac{L}{2c} \left(\frac{m_1^2 c^2 - m_2^2 c^2}{p^2} \right).$$ (2.6)

The particle-identification capability of a TOF detector is related to the number of standard deviations in the time-of-flight difference of two particles

$$n_\sigma = \frac{t_1 - t_2}{\delta t},$$ (2.7)

where δt is the time resolution.

Figure 2.2 shows the number of standard deviations as a function of the particle momentum for a TOF detector with $\delta t = 80$ ps time resolution and particle track length $L = 3.7$ m. Electron identification is feasible only at very low momenta ($p \lesssim 700$ MeV/c) where electron/pion separation is larger than 3σ. Nonetheless, the magnetic field used to measure particle momenta could prevent low-momentum particles to reach the TOF array. Pion and kaon separation better than 3σ is achieved for momenta below ~ 2.4 GeV/c, while kaon/proton separation extends up to ~ 4 GeV/c.

2.2.2 Bayesian PID

Particle identification in ALICE uses the Bayesian statistics approach [115].

The measured time-of-flight t is chosen as the PID discriminating variable for the TOF detector, and the expression

$$g_i(t) \sim \frac{1}{\sigma} \exp \frac{-(t - t_i^{exp})^2}{2\sigma^2}$$ (2.8)

is taken as the TOF detector response function for different mass hypotheses m_i ($i = e, \mu, \pi, K, p$). The response function depends on the expected time-of-flight t_i^{exp}, for a particle mass hypothesis m_i, and the overall TOF resolution σ (notice that the overall TOF resolution σ was already introduced in the previous section with the different notation δt).

On the basis of the response function $g_i(t)$, the conditional probability $P_i(t)$ for a particle to be of type i is assigned to each track, weighting $g_i(t)$

by the "a priori" probability[4] C_i:

$$P_i(t) = \frac{C_i g_i(t)}{\sum_j C_j g_j(t)}, \tag{2.9}$$

where $j = e, \mu, \pi, K, p$. The probabilities $P_i(t)$ are often called PID weights. The identity of the track is then defined by the highest among the probabilities $P_i(t)$.

This approach to particle identification allows to simply combine PID information coming from different detectors in a consistent way. Let us call $r(s_j|i)$ the generic detector response function, where s_j is the PID discriminating variable for the detector j and i is the mass hypothesis. The combined response function is the product of single detectors

$$R(\bar{s}|i) = \prod_j r(s_j|i). \tag{2.10}$$

The combined PID weights are then obtained, in the same way as for the single detector, from the combined response function

$$W(\bar{s}|i) = \frac{C_i R(\bar{s}|i)}{\sum_j C_j R(\bar{s}|j)}, \tag{2.11}$$

where $j = e, \mu, \pi, K, p$.

2.2.3   Performance

In this section a brief summary of the PID performance of the TOF detector is presented. The results have been obtained using Monte Carlo simulations of the apparatus, where a detailed description of the detector performance has been introduced on the basis of the test-beam results (Section 3.1.3). Further details on the Monte Carlo event samples and detector simulation can be found in [115], where a comprehensive review of the track-matching and PID procedures is also discussed.

The particle tracks reconstructed by the ALICE tracking detectors (Section 1.3.3) are associated with a TOF signal. In Figure 2.3 the performance

---

[4]The "a priori" probabilities C_i have to be determined. In the simplest approach they can be assumed to be equal.
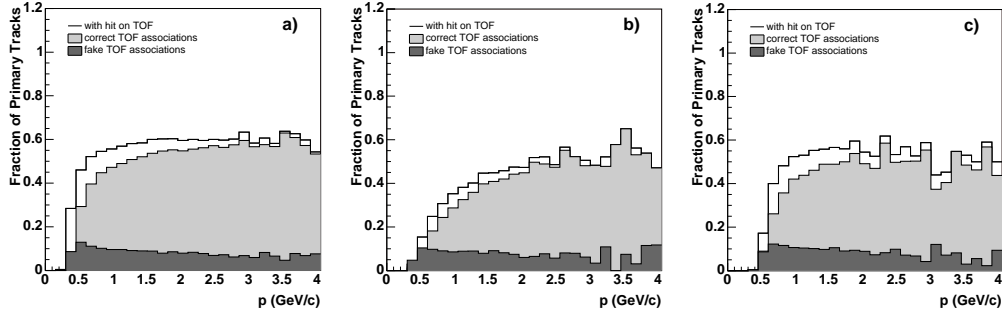
Figure 2.3: The fraction of primary pions (a), kaons (b) and protons (c), generated in the TOF acceptance region, which are associated with a TOF signal in simulated Pb–Pb central collisions. Further details in [115].
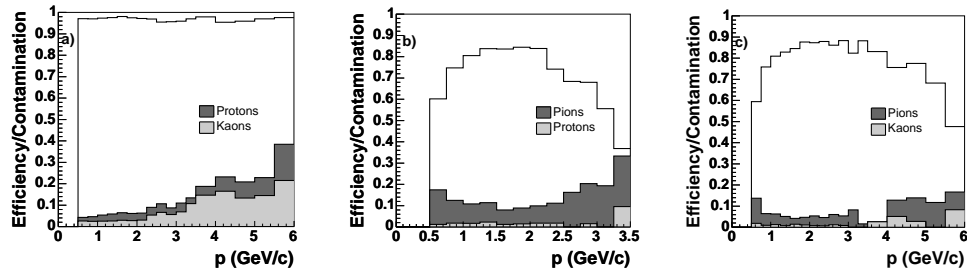

Figure 2.4: Momentum dependence of efficiency (empty histogram) and contamination (light and dark shaded histograms) of TOF particle identification algorithm for pions (a), kaons (b) and protons (c) in simulated Pb–Pb central collisions. Further details in [115].
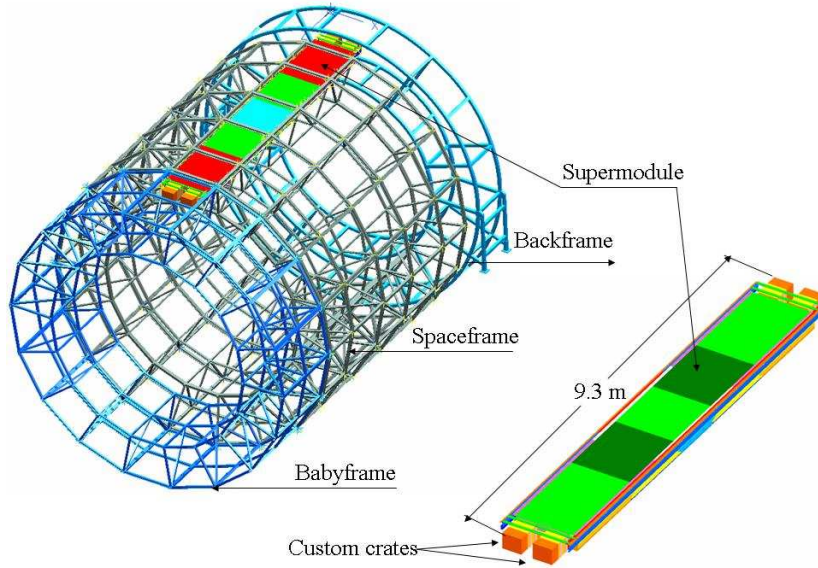
54

Figure 2.5: Schematic drawing of a TOF SuperModule in the ALICE Spaceframe.

of the association algorithm is shown in terms of the fraction of primary particles generated. The low-momentum loss is mostly due to interaction of particles with the material in front of the detector and to kaon decays.

A Bayesian method, already described in Section 2.2.2, is used to translate the track–signal association into particle-identification information. The efficiency (identified particles) and contamination (wrongly identified particles) for pion, kaon and proton identification are presented in Figure 2.4. The results show the expected separation capabilities for a 80 ps resolution Time-Of-Flight array (Section 2.2.1).

2.3   Detector layout

The TOF detector covers the full azimuth of the ALICE central region with a surface of polar acceptance $|\theta - 90°| < 45°$. The whole device is inscribed in a cylindrical shell with an internal radius of 370 cm and an external one of 399 cm from the beam axis. The whole thickness corresponds

Pseudorapidity coverage	$-0.9 < \eta < 0.9$
Azimuthal coverage	2π
Radial position	$370 < r < 399$ cm
Radial thickness	$X/X_0 = 29.5\%$
Active area (total area)	141 m^2 (171 m^2)
ϕ-segmentation	18-fold
z-segmentation	5-fold
Readout pad geometry	3.5×2.5 cm^2
Total number of modules	90
Total number of strips	1638
Number of readout channels	157248

Table 2.1: Summary table with TOF relevant parameters.

on average to 30% of a radiation length X_0.

The detector design [113] follows a modular structure, corresponding to a 18-fold segmentation in azimuth (sectors) and a 5-fold segmentation along the beam axis (modules). Each sector, which consists of 5 modules grouped in a line to form a SuperModule, is inserted into the outer cylindrical part of the ALICE Spaceframe 3.7 m away the interaction point (Figure 2.5).

The Multigap Resistive Plate Chamber (MRPC) strip (Sections 2.1.1 and 2.3.1) is the basic unit of the ALICE TOF detector. It is a 10-gap double-stack MRPC strip (120×7.4 cm^2 active area), segmented into two rows of 48 readout pads each. The strips are located inside gas-tight modules, transversely with respect to the beam direction, with a tilted positioning (with angles increasing from 0° to 45°) in order to have a pointing geometry. 1638 MRPC strips have been built for the whole system at the INFN laboratories in Bologna.

The TOF module (Section 2.3.2) consists of a group of several MRPCs closed in a gas-tight box (different modules are used). Front-end electronics is mounted on the external side of this box. The complete TOF system consists of 90 modules. Three central modules have not been installed to reduce the amount of material in front of the PHOS detector (Section 1.3.5). All the modules have been assembled at the INFN laboratories in Bologna.

Five modules in a row are bounded together with longitudinal and transverse aluminium beams to form the SuperModule (Section 2.3.3) structure. Front-end electronics, cables, pipes are located within the SuperModule vol-

ume. Four custom crates are fixed in pairs at both ends of the SuperModule to contain the power supply system (Section 2.5.1) required for front-end and readout electronics and the readout electronics itself (Section 2.4). The 18 SuperModules have been assembled at CERN and installed inside the ALICE Spaceframe.

2.3.1   The double-stack MRPC strip

The Multigap Resistive Plate Chamber (MRPC), introduced in Section 2.1.1, was originally developed in 1996 [123]. It consists of a stack of resistive plates with electrodes connected to the outer surfaces.

The basic detecting element used for the Time-Of-Flight detector of ALICE is the double-stack MRPC strip, shown in Figure 2.6 and 2.7. The strip geometry was chosen so that a differential signal can be directly derived from the pickup pads to fed the front-end electronics. Moreover, it allows the MRPCs to be oriented to the interaction point (in the rz plane). This reduces the number of very oblique transversal paths that can create a sharing effect of the signal among adjacent pads, thereby increasing the occupancy and the time resolution. The strip is a 120×7.4 cm^2 active area device (122 cm long and 13 cm wide), segmented into two rows of 48 pickup pads of 3.5×2.5 cm^2.

The double-stack design consists of two stacks of equally spaced resistive plates, creating 5 gas gaps of 250 μm each. Nylon fibres (fishing line) are used to define the size of the gas gap; these spacer fibres run across the width of the strip at the boundaries between pads[5] (every 2.5 cm), held by plastic pins. The high voltage is applied to the outer surfaces of the stack of resistive plates (external plates). The internal plates are electrically floating and take the voltage by electrostatics[6]. Two external (cathode-side) and one internal (anode-side) printed circuit boards (PCBs) define the two stacks. The PCBs contain the 96 pickup pads (to collect the avalanche signal) and two small high-voltage pads at the extreme ends (to provide the external plates with high voltage).

The resistive plates are made of "soda-lime" glasses[7]; the internal and

---

[5]A small amount of MRPC strips have been constructed using a "staggered" layout of the spacer fibres.

[6]The internal glasses are kept at the correct voltage value by the flow of positive ions and electrons in the avalanches [136].

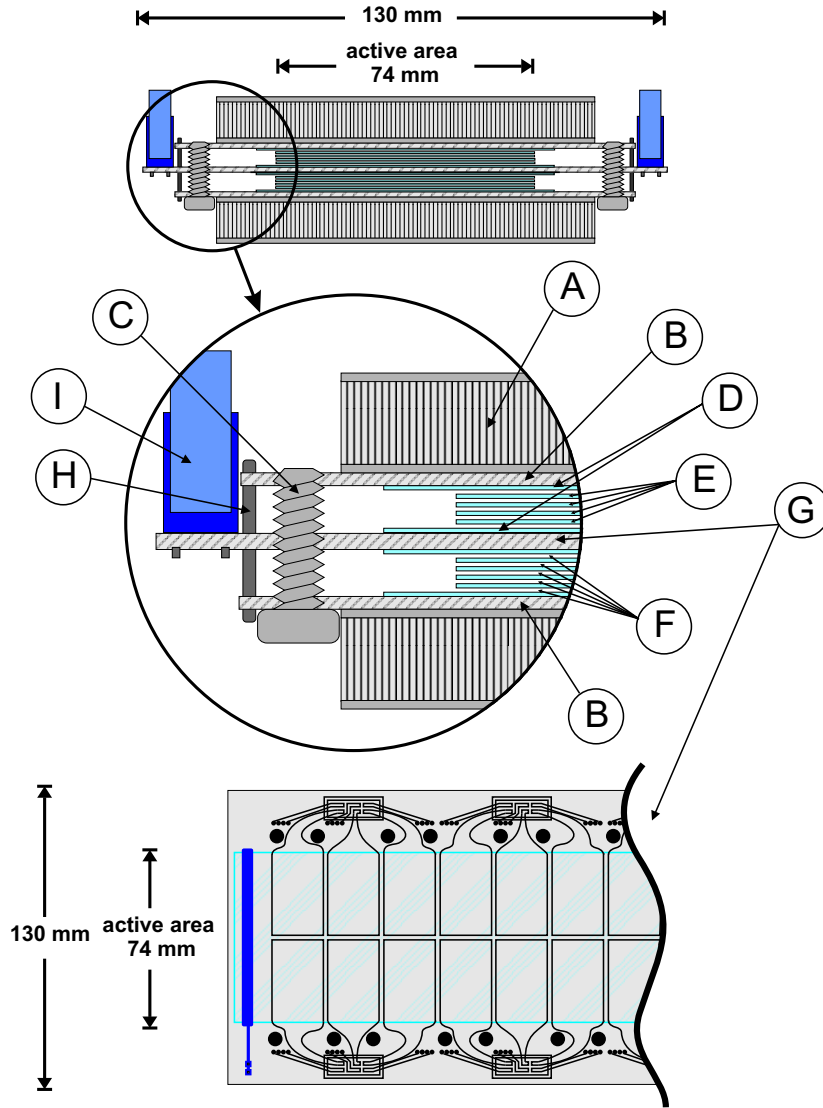[7]Manufactured by Glaverbel, Brussels, Belgium.

Figure 2.6: Schematic drawing (cross section and top view of the anode PCB) of the ALICE TOF MRPC strip. (A) 10 mm thick honeycomb panel; (B) PCB with cathode pads; (C) M5 nylon screw to hold fishing line; (D) 550 μm thick external glass plates with resistive coating; (E) 400 μm thick internal glass plates; (F) 250 μm wide gas gaps; (G) PCB with anode pads; (H) metallic pins to bring cathode signals to central PCB; (I) connectors for differential signal from MRPC to front-end electronics.
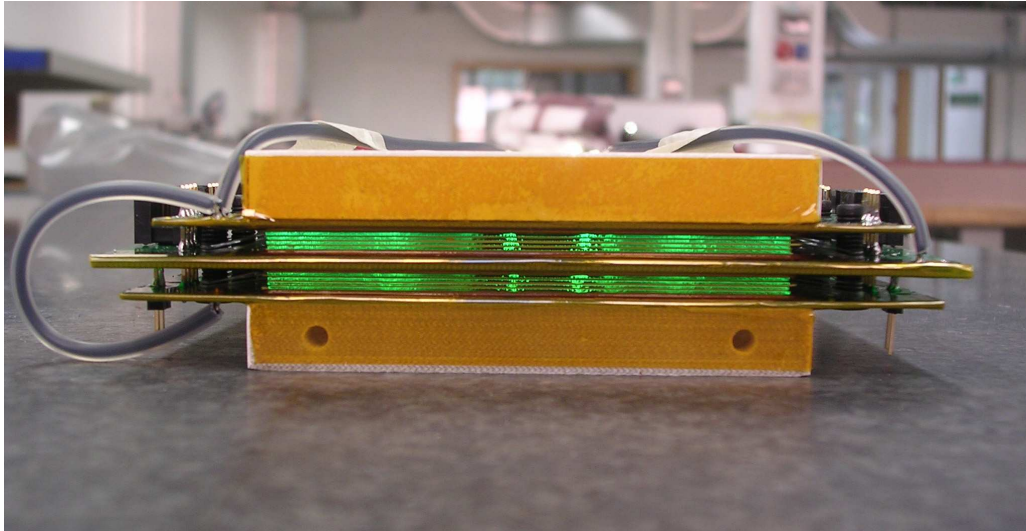
Figure 2.7: Photograph of a 10-gap double-stack MRPC strip.

external plates are 400 μm and 550 μm thick, respectively. The external surface (facing the PCB) of the outer plates is painted with a resistive coating[8] of a few MΩ/$\square$. This is used to apply the high voltage.

The mechanical stiffness is guaranteed by two honeycomb panels, glued on the external PCBs. Connecting pins are soldered across the 3 PCB layers in order to bring cathode signals from the external PCBs to the central PCB, where anode signals are collected. Moreover these pins keep the stacks compressed. Two rows of 16 connectors are soldered on the central PCB to transmit the differential signals to the front-end electronics.

Two pulse lines on one cathode PCB run along the length of the strip creating a capacitive coupling to the pickup pads used for monitor and calibration purposes (Section 3.3.3).

2.3.2 Modules

Five modules of three different types are needed to form a SuperModule: two external, two intermediate and one central. They have all the same structure and width (128 cm) but differ in length, number of strips and position along the SuperModule (as their names suggest). The external (177

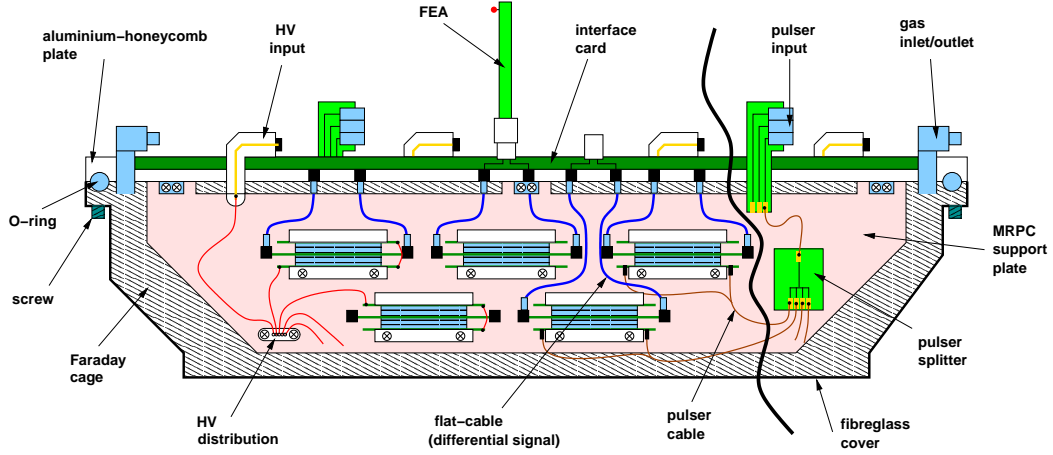[8]An acrylic paint loaded with metal oxides. DETEC, Torino, Italy.

Figure 2.8: Schematic drawing of a TOF module. The picture does not represent any of the three ALICE TOF module types, but aims to help focusing on the generic module design. See text in Section 2.3.2 for details.
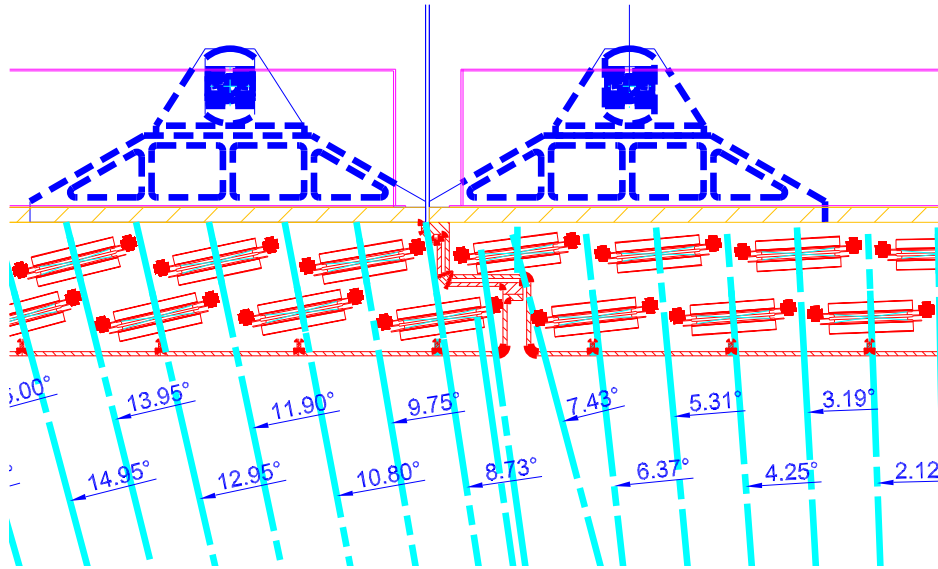

Figure 2.9: Detail of the overlap region between two modules and strip positioning.

cm long) and intermediate (137 cm) modules host 19 MRPC strips, the central module (117 cm) 15 strips. As already pointed out, the strips are tilted inside the modules to face the interaction point.

The modules have been designed to minimize dead regions. The dimensions are defined in such a way that their joining areas are aligned with the dead areas due to the presence of the Spaceframe structure. The module shape and the strip positioning at the joining sides were designed to provide an almost full coverage nevertheless. Moreover, to minimize the dead area within the module, adjacent strips are overlapped by about 2 mm (Figure 2.9).

The TOF module, which is shown with a schematic drawing in Figure 2.8, is a box that defines and seals the MRPC strip gas volume and supports the external front-end electronics and services (high voltage, gas, pulser). A 1.5 cm thick aluminium-honeycomb plate gives the mechanical stiffness to the chamber. A fibreglass 0.3 cm thick cover closes the gas volume connecting to the aluminium plate by means of sealing O-ring and screws. The inner surface of the fibreglass is covered with an aluminium layer for electromagnetic shielding (Faraday cage). Inside the module two plates are fixed perpendicularly to the honeycomb to support the strips. The MRPC are then attached to those plates at the required angle with plastic screws.

Holes that can accommodate feed-through for signal cables, high-voltage connectors, gas inlet/outlet and pulser inputs are machined in the honeycomb plate. Large printed circuit boards (PCBs), covering almost all the honeycomb surface, are glued to the plate. The PCB (also called Interface Card) provides the interface between the gas volume and front-end electronics: on the external side it houses the connectors where the front-end cards are plugged into, while on the internal side there are the connectors for the flat-cables coming from the MRPCs. 17-23 cm long twisted-pair flat cables connect the strips with the Interface Card, each cable taking the differential signals of 3 pads.

In the gas volume the high voltage is distributed to groups of 3-4 MRPCs. The distribution occurs by means of a passive HV splitter which connects the MRPCs to the high-voltage connector. Positive and negative voltages are located at opposite sides of the module. A "pulser splitter" card located in the gas volume deals with pulser distribution: two lines per strip.

Pictures highlighting some details of a TOF module are shown in Figure 2.10.
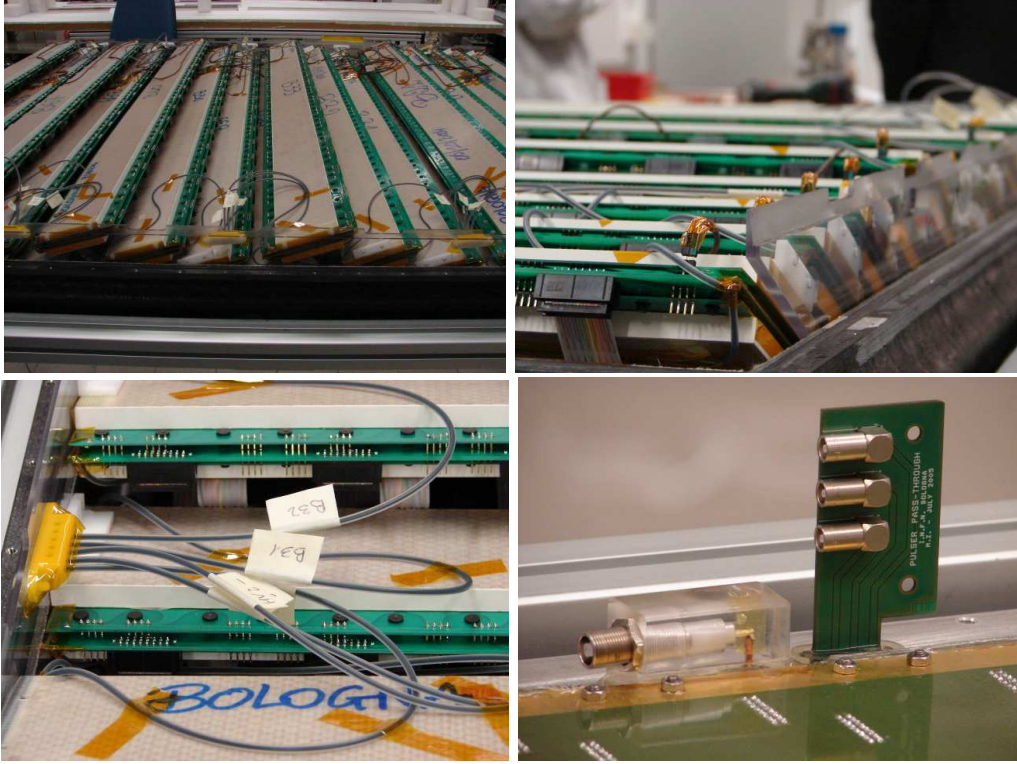
Figure 2.10: Pictures showing some details of an intermediate TOF module (top left): high-voltage connection, flat and pulser cable on a MRPC strip (top right); high-voltage distribution (bottom left); high-voltage and pulser connectors (bottom right).

2.3.3 The SuperModule

The modules with MRPCs inside were assembled at the INFN laboratories in Bologna, transported to CERN and put together to form SuperModules.

A schematic layout of a TOF SuperModule is shown in Figure 2.11. Five modules in a row (external, intermediate, central, intermediate, external) are aligned among themselves to lay in the same plane without gaps. Long aluminium beams bound them along their length with stainless steel screws, which fix the beams to the module honeycomb panel, on the opposite side of the gas volume. Transverse aluminium beams bound the modules at their joining area in the same way. The transverse beams at both sides of the external modules provide support for the readout crates, which are attached
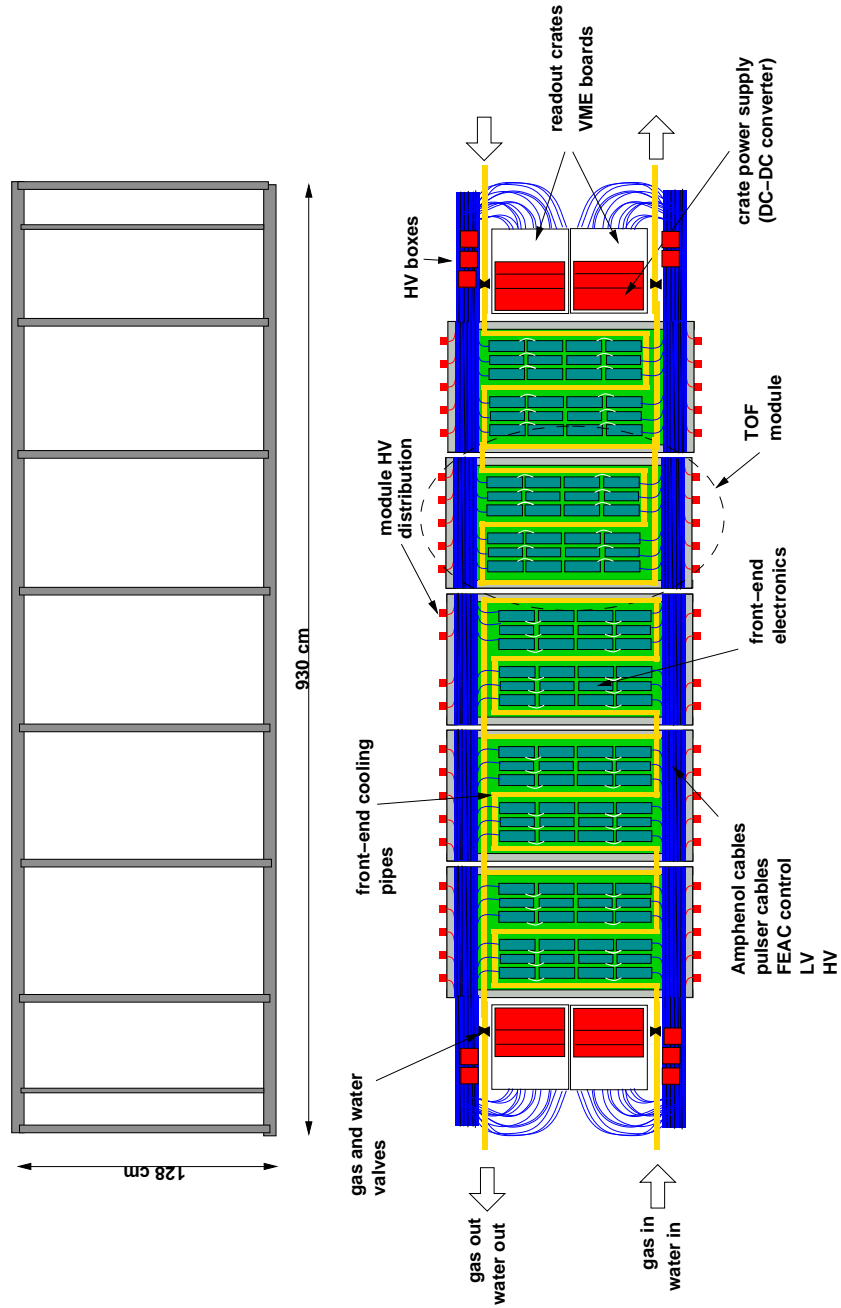
Figure 2.11: Schematic layout of a TOF SuperModule. See text in Section 2.3.3 for details.
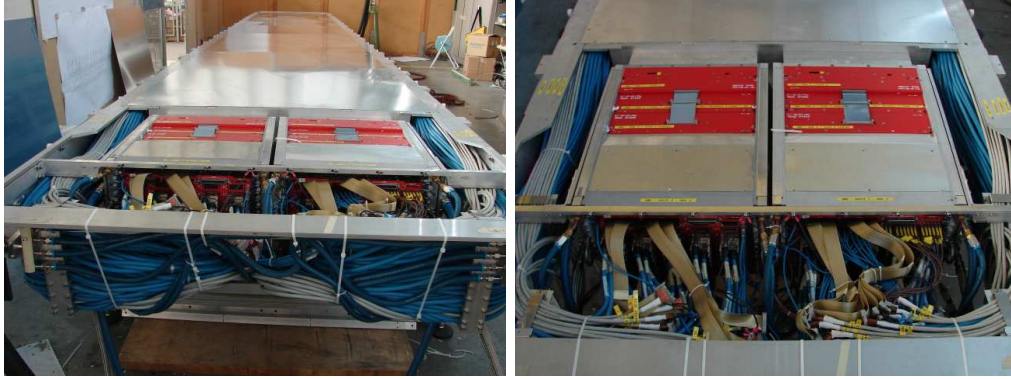
Figure 2.12: Fully assembled ALICE TOF SuperModule (left). Detail of the SuperModule "crate area" (right).

Cable / pipe	From	To
High voltage	SuperModule HV boxes	module HV input
Low voltage	Crate LV output	FEAC
Pulser	CPDM	module pulser input
Gas	gas distribution	module gas inlet/outlet
Water	water distribution	front-end cooling
Amphenol	FEA	TRM
FEAC control	FEAC	LTM

Table 2.2: Summary of cables and services of a ALICE TOF SuperModule.

in pairs to both ends of the structure. Readout boards (Section 2.4.2) are housed inside the crates as well as the DC-to-DC converter power supplies (Section 2.5.1).

The aluminium beams arranged in that way form five zones corresponding to the so-called "front-end area" of each module. Each zone is equipped with a copper serpentine pipe, supported by further aluminium structures, for front-end electronics cooling with water. Straight copper pipes are placed along the longitudinal aluminium beams, in the so-called "cable area", for gas supply. Both water and gas input/output are located on both sides of the SuperModule, in the "crate area". Independent water and gas circuits branch from the crate area to feed modules. Each segment is equipped with valves which provide modularity in the water and gas distribution.

All cables (high-voltage and low-voltage cables, Amphenol signal cables, FEAC[9] control cables, pulser cables) and services (gas and cooling pipes) are stretched in the cable area. Table 2.2 summarizes all these cables and the associated connections. The SuperModule HV distribution boxes (Section 2.5.2) as well as the water and gas distribution systems (Section 2.5.3 and 2.5.4) are fixed on the crates, sideways. In the same zone the water distribution system for crate cooling is located.

The front-end electronic FEA[10] cards are plugged into their connectors on the module interface card and fill the front-end area. Aluminum plates are attached to the FEAs to provide thermal contact with the water pipe serpentine for cooling purposes (Figure 2.16). The FEAC cards, also fixed in the front-end area (Figure 2.16), distribute the low voltage to FEAs through flat cables and collects trigger signals (Section 2.5.1 and 2.4.3): six groups of two daisy-chained FEAs are managed by a FEAC. A 0.15 cm thick aluminium cover close the volume housing the front-end electronics.

In Figure 2.12 some pictures of a fully assembled SuperModule are shown.

2.3.4   The custom crate

Four water-cooled VME custom crates (SY2390[11]) are installed on each SuperModule (Figure 2.13 and 2.21). They are designed to host the TOF readout electronics (Section 2.4.2) and the DC-to-DC converter low-voltage power supplies (Section 2.5.1). Heat-exchangers are attached to the side-walls in such a way that water circulates to dissipate the heat from the boards by thermal contact[12].

Each crate contains a VME64x bus and allows for the insertion of up to 12 VME boards in the front side. A large printed circuit interface card on the bottom provides the low-voltage distribution from the power supplies to readout and front-end electronics as well as other connections. A private bus, realized on the VME P2 connector, allows for remote control of VME board status and powering operations.

The crates are installed in pairs (right- and left-crate) at the ends of the

---

[9]Front-End Analogue Control (FEAC) card. See Section 2.4.1.

[10]Front-End Analogue (FEA) card. See Section 2.4.1.

[11]Produced by CAEN S.p.A.

[12]A commercial thermoconductive paste is used in the interface of the crate walls and the boards, which are equipped with a "card-lock" system to guarantee optimal contact.

Figure 2.13: Front view of the ALICE TOF crate with 10 TRM boards installed.

SuperModule. Right-crates contain one DRM[13], one LTM[14], one CPDM[15] and 9 TRMs[16], filling the slots from 1 to 12. In left-crates another TRM is installed in place of the CDPM.

The whole system has been tested to work in a 0.5 T magnetic field under moderate radiation. Moreover, special attention has been used in designing the crate in order to allow maintenance operation on both readout boards and power supplies.

2.4 Electronics

As all modern detectors for nuclear and subnuclear particle physics, the ALICE TOF detector makes wide use of electronics to interface with the de-

---

[13]Data Readout Module (DRM). See Section 2.4.2.
[14]Local Trigger Module (LTM). See Section 2.4.3.
[15]Clock and Pulser Distribution Module (CPDM). See Section 2.4.2.
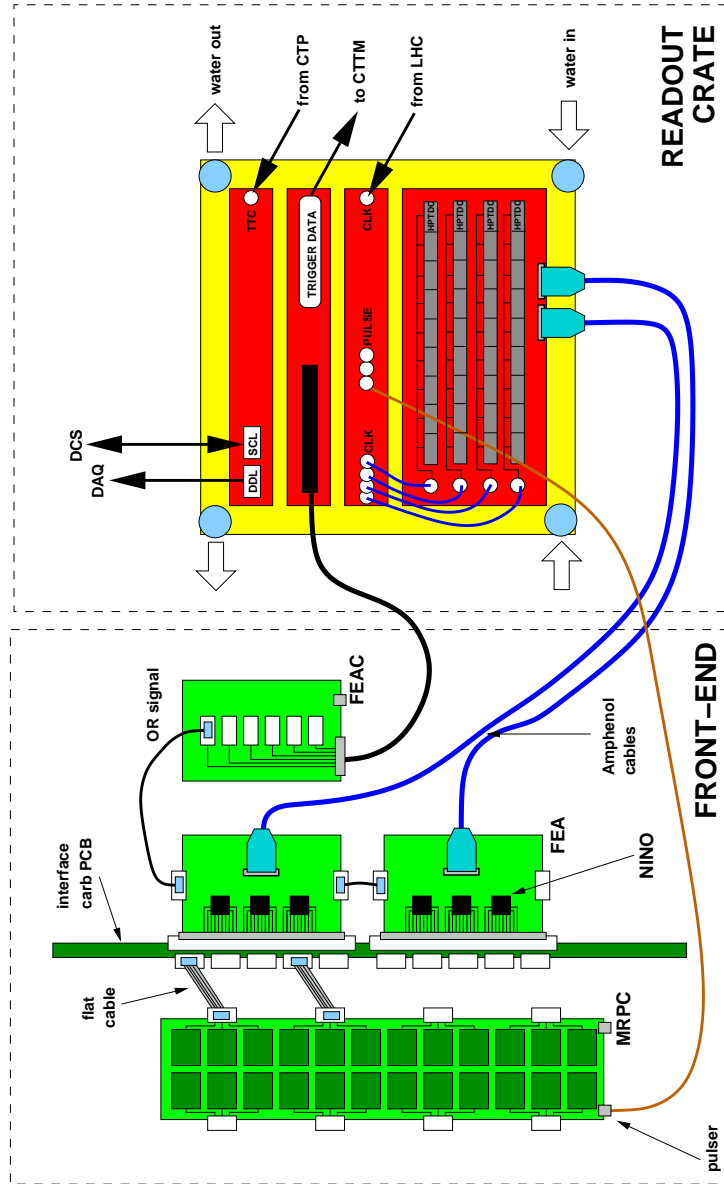[16]TDC Readout Module (TRM). See Section 2.4.2.

Figure 2.14: Schematic drawing of the ALICE TOF electronics. The readout system housed in the crate is shown on the right (Section 2.4.2), while the front-end electronics is on the left (Section 2.4.1). The readout boards in the crate, from top to bottom: DRM, LTM, CPDM and several TRMs. More details on the functioning can be found in Section 2.4.

tecting elements (MRPC). This is the aim of front-end electronics, described in Section 2.4.1. In complex detector systems like ALICE, the detectors have also to deal with experiment-wide central systems (data acquisition, trigger) which collect and distribute necessary information for physics purposes. This is done by the readout system, which is described in details in Section 2.4.2. Since MRPC is a fast-response device, TOF can provide the experiment with triggers. The associated electronics is listed in Section 2.4.3.

In Figure 2.14 a schematic layout of the TOF electronics is shown. The differential signals generated on the MRPC pads by the avalanche process are transferred through flat-cables and the module interface PCB cards (Section 2.3.2) to the front-end electronics. The NINO ASIC[17], hosted on the FEA card, amplifies and discriminates the analog signal. Afterwards, the signals are sent to the HPTDC[18] through special shielded cables[19] (optimized to preserve the signal integrity) for digitization and readout happens in the TOF VME crate (Section 2.4.2). At the same time, the FEA card derives an "OR" signal for trigger purposes which is first collected in the FEAC cards and then elaborated in the LTM. Data from the LTM are sent to the CTTM[20] for further trigger processing (Section 2.4.3).

Table 2.3 summarizes the relevant electronic devices and chips used for the whole detector and for the single SuperModule.

2.4.1 Front-End Electronics

For the full exploitation of the excellent timing properties of the Multigap Resistive Plate Chamber (MRPC), front-end electronics with special characteristic has been designed. The FEA card hosts the NINO ASIC chips for amplification/discrimination of the MRPC signals. The FEAC card acts as a service card for front-end electronics.

NINO ASIC chip

The NINO ASIC chip [137], fabricated with 0.25 μm CMOS technology, is an 8-channel amplifier and discriminator chip. It has been specifically developed to match the requirements for the ALICE TOF MRPC-strip detector:

---

[17]Application Specific Integrated Circuit (ASIC).
[18]High-Performance Time-to-Digital Converter (HPTDC). See Section 2.4.2.
[19]Amphenol skewclear cables.
[20]Cosmic and Topology Trigger Module (CTTM). See Section 2.4.3.

Device	Quantity / SuperModule	Total quantity
NINO	1092	19656
FEA	364	6552
FEAC	32	576
HPTDC	1140	20520
TRM	38	684
Custom crate	4	72
DRM	4	72
LTM	4	72
CPDM	2	36
ACM		5
CTTM		1

Table 2.3: Relevant electronic devices and chips used for the ALICE TOF detector. The quantity installed on a SuperModule and the total quantity for the whole detector are quoted.

- differential input, to profit from the differential signal from the MRPC;

- fast amplifier, with less than 1 ns peaking time;

- input charge measurement by Time-Over-Threshold (TOT) for time-slewing correction.

The NINO ASIC encodes the charge of the input signal into the width of the output signal (Time-Over-Threshold). No further readout electronics is needed to measure the charge. To match the width requirements of the HPTDC[21] a pulse stretcher increases the pulse width by 10 ns[22].

The NINO ASIC is a very low power-consumption (40 mW/channel) chip, a factor 10 less than the commercial discrete amplifier/discriminator solution used for the detector prototypes[23], and it is very compact (2 mm × 4 mm), thus reducing the size of the front-end card. Moreover, it has differential

---

[21]The HPTDC can only measure both leading and trailing edges of an input pulse for widths greater than ~ 6 ns.

[22]The pulse width before stretching varies between 2 ns and 7 ns.

[23]A solution based on MAXIM 3760 (amplifier) and MAXIM 9691 (discriminator) was used to test the first MRPC prototypes before the introduction of the NINO ASIC.
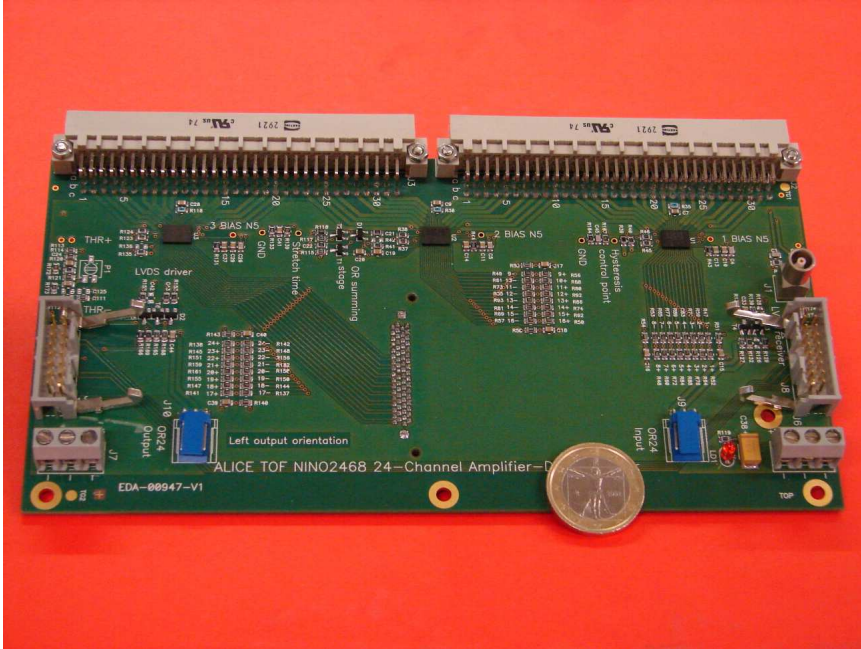
Figure 2.15: The Front-End Analogue (FEA) card with the NINO ASIC chips used by the ALICE TOF detector.

input and it is differential throughout, leading to an increased sensitivity and increased immunity to cross-talk.

Front-End Analogue (FEA) card

Three NINO ASIC chips for a total of 24 channels are hosted on the Front-End Analogue (FEA) cards. A picture of the FEA is shown in Figure 2.15. These cards are mounted directly on the TOF module Interface Card (IC) printed circuit board (Section 2.3.2 and 2.3.3).

The card collects the output signals from the NINO chips and connects them to the HPTDC chips through 2-5 metres long 24-pairs Amphenol cables[24]. Moreover, it forms a 24-channel OR output signal for trigger purposes (Section 2.4.3).

The FEA card receives from the FEAC card the low voltage (2.5 V) and an external threshold voltage (set by the LTM) to set the differential

---

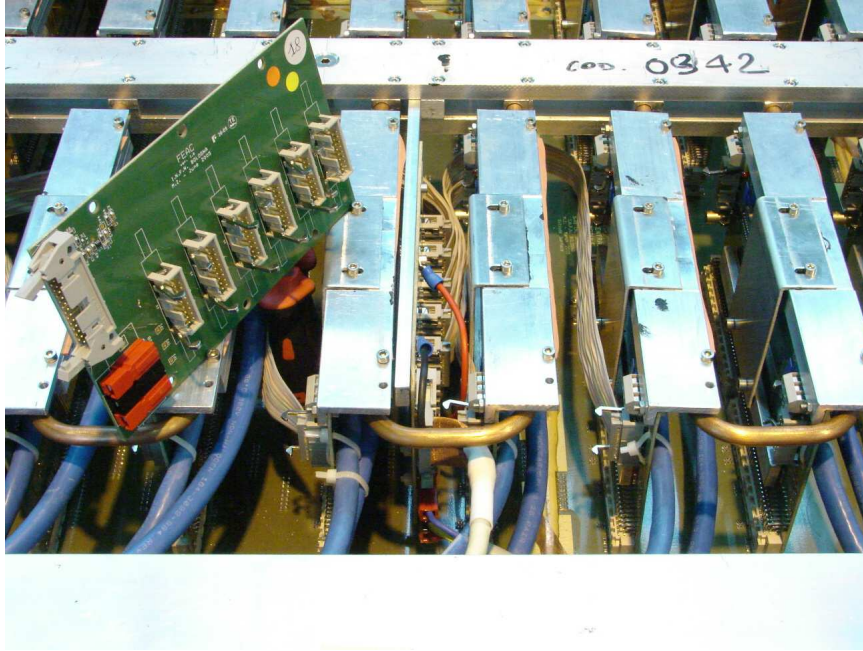[24]Amphenol skewclear cables with SCSI VHDCI connectors.

Figure 2.16: The Front-End Analogue Control (FEAC) card. A not-yet connected card is shown on the left. In the middle of the picture, between two FEA cards, it is possible to see a FEAC in its final position. The picture also shows the front-end cooling system (serpentine and FEA heat dissipators).

threshold of the NINO discriminator circuit[25].

Front-End Analogue Control (FEAC) card

The FEA Control (FEAC) card, shown in Figure 2.16, serves 12 FEA cards with the required low voltage and threshold voltage. It is equipped with a temperature sensor to monitor the temperature of the region of the TOF SuperModule which houses the front-end electronics. Moreover, it has been designed to provide the LTM with a voltage monitor line along with a temperature monitor line as well as to collect the OR signals from the FEA cards. The OR signals are sent to the LTM for trigger purposes through a

---

[25]The threshold of the discriminator is adjustable in the range $10-100$ fC with an applied threshold voltage $0-1.6$ V.

dedicated cable.

2.4.2 Readout system

In Figure 2.14 a schematic layout of the readout crate is shown. The TRM, which houses and performs the readout of the HPTDC chips, is the main data producer. The LTM, besides trigger functions, also produces data for front-end monitoring. The DRM receives trigger information from the central trigger processor (CTP) and propagates it to TRMs and to HPTDCs. Then it performs the readout of the data available in the boards and sends them to the central data-acquisition system. Moreover it interfaces with the Detector Control System (DCS) for electronics configuration and monitoring. The common LHC clock distribution to HPTDCs is done by the CPDM which also generates the test pulse to MRPCs.

High-Performance Time-to-Digital Converter (HPTDC)

The High-Performance Time-to-Digital Converter (HPTDC) ASIC chip [138, 139] has been developed by the microelectronics group at CERN and designed as a general-purpose TDC for LHC experiments. The HPTDC works using a 40 MHz clock to fit with the LHC bunch-crossing rate. Different working mode resolutions are obtained from the 40 MHz clock, but for TOF MRPC signal digitization only the Very High Resolution Mode (VHRM) is used[26]. In this mode the chip is a 8-channel[27] TDC with 24.4 ps LSB[28]. The HPTDC has multi-hit[29] functionalities which allow to select hits at a given offset with respect to the trigger time, within a user-programmable time window.

A relevant feature of the HPTDC is the signal leading- and trailing-edge detection capability. This allows Time-Over-Threshold (TOT) measurements of the MRPC analog signal for time-slewing correction by measuring the width of the digital signal from the NINO (Section 2.4.1). On the other hand, the minimum time between two consecutive time measurements is a

---

[26]The HPTDC version 1.3 is used.

[27]In the other modes the HPTDC can handle up to 32 channels.

[28]A specific set of calibration constants for each chip is needed in VHRM. This allows to online correct for Integral Non Linearity (INL) effects.

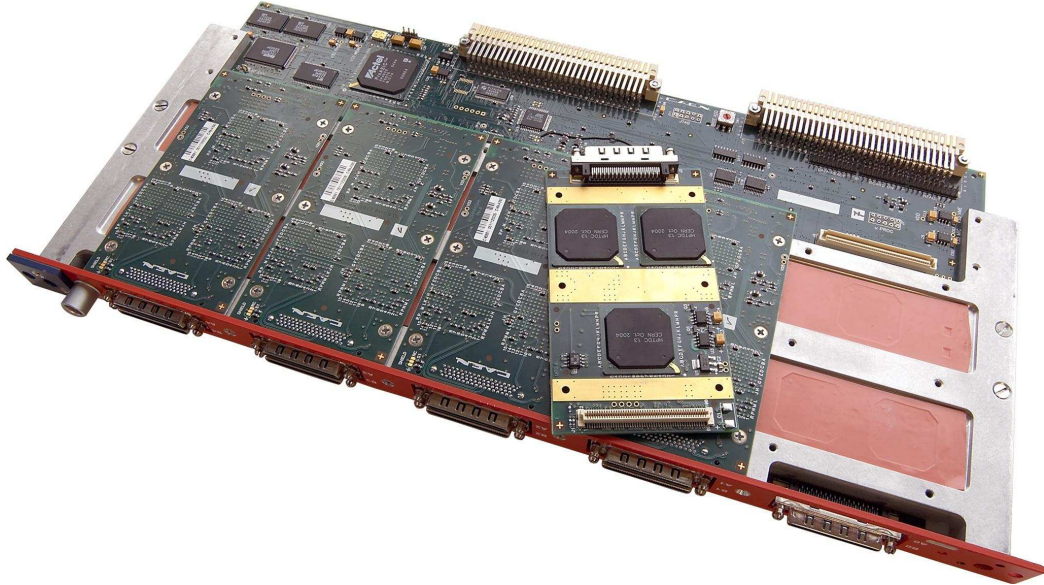[29]We call "hit" the time measurement encoded by the HPTDC in a 32-bit information (word).

Figure 2.17: The TDC Readout Module (TRM). In the picture a piggy-back hosting 3 HPTDC chips is removed from the board. It is possible to notice the mid-plane of the board which provides the proper cooling to the HPTDCs.

critical parameter of the HPTDC: according to the manual this value is "typically 5 ns (guaranteed 10 ns)". Therefore the FEA cards provide the TOT signal with a minimum width of 10 ns (Section 2.4.1). It is worthwhile to mention that in VHRM the HPTDC cannot provide "paired" measurements (i.e. packing in a single 32-bit word the leading edge and the width measurement of the signal): two 32-bit words (hits) are needed. This would result in a nearly factor 2 increase of the required bandwidth and of the TOF raw data size. To overcome that, a custom packing is performed by the TRM together with other checks on HPTDC data.

TDC Readout Module (TRM)

The TDC Readout Module (TRM) [140–142] is a 9U VME slave card whose aim is to readout time information digitized by the HPTDCs. The TRM is the basic block of the ALICE TOF readout system which has a total of 684 TRM boards. Each TRM (Figure 2.17) hosts 30 HPTDC (a

solution with 10 identical 3-HPTDC piggy-backs is used) chips organized in two separate parallel readout chains, for a total of 240 TDC channels. Special attention has been used to guarantee the needed cooling of HPTDCs. The VME interface is implemented by a FPGA[30] which also acts as Readout Controller, Event Manager and online Data Processor.

The basic functionalities of the TRM board can be summarized analyzing the workflow. When a Level-1 trigger signal arrives the board distributes it to each HPTDC as trigger tag. Then the Readout Controller moves the time-matched hits from the HPTDC buffers to two coupled SRAMs[31], handled by the Event Manager. Finally a Level-2a signal starts the transfer of the event to the output buffer of the board. A Level-2r assertion makes the Event Manager discard the event instead. Between Level-1 and Level-2 trigger signals, the FPGA provides data packing and online data compensation.

The FPGA provides data compression (merging leading- and trailing-edge measurements in a single word) and online data compensation for Integral Non Linearity (INL) of the HPTDC [138, 139] accessing chip-specific calibration constants stored on the board.

Data Readout Module (DRM)

Each ALICE TOF custom crate is equipped with a Data Readout Module (DRM), a 9U VME master card. The DRM acts as the main interface between the central ALICE data acquisition/trigger system and TOF electronics.

The main task of the DRM is to read TRM and LTM data on the VME backplane accessing their output buffers. The data, once collected, are arranged[32] following the data format common to all ALICE detectors and sent through the DDL[33] optical link [134, 143]. A specific feature of the board allows to duplicate the data being sent over the DDL on a dedicated staging RAM, which can be accessed through the Slow Control Link (SCL). This allows for external online data monitor and processing without interference

---

[30]Field Programmable Gate Array (FPGA).

[31]Two coupled SRAMs are used to mimic a dual port RAM.

[32]The ALICE Common Data Header, which defines the experiment-wide common data format, is prepended to DRM data which contain LTM and TRM data.

[33]The ALICE Detector Data Link (DDL) is a 200 MB/s, full duplex, multi-purpose optical-fibre link. It has been designed to cover the needs for data transfer between the detectors and the data-acquisition system.

to the readout and data-acquisition workflow.

Another important task of the DRM is to provide an interface with the ALICE trigger system. The board reads and decodes trigger signals and messages (trigger data) received through the TTC[34] optical link. Part of the trigger information is stored in the data to be sent over the DDL for further consistency checks. Level-1 and Level-2 triggers as well as other control signals (i.e. bunch-crossing reset) coming from the ALICE central trigger system are notified through the VME backplane to all boards in the crate. Furthermore, the DRM has a set of auxiliary connectors used for specific functions. As an example, the board sends to the ACM[35] the BUSY signal[36].

The Slow Control function deals with the configuration and control of the detector electronics. A Slow Control optical Link is installed on the DRM to allow VME access for these purposes. A major task of the SCL link, besides electronics configuration, concerns monitoring of both detector and electronic components a well as of the data being recorded. The temperature of the VME boards are read through the SCL link. The same applies for monitor temperatures and voltages of the front-end electronics, as recorded by the LTM.

Finally the DRM allows to program the FPGA of the boards in the crate. This feature is provided by an ARM[37] CPU-based general purpose single-board computer (A1500) with Ethernet interface, mounted as a piggy-back card in the DRM. Furthermore, it receives a PULSE signal from the ACM and drives the CPDM pulse generator, used for detector monitoring and calibration.

Clock and Pulser Distribution Module (CPDM)

The main aim of the Clock and Pulser Distribution Module (CPDM) is to distribute the LHC clock to the VME boards installed in the ALICE TOF VME crates. One CPDM feeds two neighbouring crates, placed at one side of the TOF SuperModule. It has to be pointed out that a dedicated clock

---

[34]Timing, Trigger and Control (TTC) system for the LHC. A TTCrx ASIC, which has been developed by the CERN Microelectronics Group, is installed on the DRM.

[35]Auxiliary Control Module (ACM).

[36]The BUSY signal inhibits further triggers from being generated by the ALICE central trigger processor during readout.

[37]The ARM architecture (previously, the Advanced RISC Machine) is a 32-bit RISC processor architecture widely used in embedded designs.

distribution has been used for TOF detector in order to guarantee the lowest possible time-jitter when received by the HPTDC chips.

The CPDM receives the LHC High-Quality clock via optical fiber and splits it into 24 LVDS clock signals which are then delivered to the boards through dedicated cables. The clock distribution guarantees the time synchronization among all TOF electronics (i.e. LTM synchronization for trigger coincidences) and high-performance in time resolution, adding a negligible (17 ps) contribution to the global time resolution.

The second task of the CPDM is to generate the pulser signal for calibration and monitoring purposes (see Section 2.3.1).

Auxiliary Control Module (ACM)

Five 6U Auxiliary Control Modules (ACMs) are installed in a commercial VME crate[38] in the ALICE trigger area[39]. Each module has 16 RJ45 inputs to handle BUSY and PULSE signals. BUSY signals from the DRMs are elaborated to generate the global BUSY signal to the CTP. The PULSE signal is sent to the DRMs to assert CPDM pulse generation. Two spare lines are available for two more signals.

2.4.3 Trigger system

The architecture of the ALICE TOF trigger uses a two-layer structure based on 72 VME (9U) boards, the Local Trigger Modules (LTM), and a single large-size board, called Cosmic and Topology Trigger Module (CTTM), to handle the information coming from the LTMs. The TOF detector provides fast trigger signals to the ALICE Central Trigger Processor (CTP) and will contribute to the Level-0 and Level-1 trigger decision [144].

Local Trigger Module (LTM)

The Local Trigger Module (LTM) [144] is a 9U VME custom board[40]. The first layer of the TOF trigger system is made of 72 LTMs, each housed in one of the TOF VME crates. Four LTMs are needed to process the data produced by one TOF SuperModule.

---

[38]Produced by Wiener.
[39]Below the Muon Spectrometer arm.
[40]Produced by CAEN S.p.A.

The aim of the TOF LTM is to act as an interface layer between the front-end electronics and the CTTM, which is the TOF central trigger board. Each LTM is connected to 8 FEAC cards, each collecting the OR signals from a group of FEA cards, through eight cables whose average length is ~ 4 m.

The LTM is equipped with commercial delay units (3D3418-0.25) programmable through the VME interface. These Programmable Delay Lines (PDLs)[41] allow to compensate for the relative time shifts among the 3456 trigger input signals. The LTM makes use of two FPGAs: one used for control purposes (low voltage and temperature monitor, threshold setup of the front-end electronics and PDL setup), the other one to handle the 48 trigger input signals. The trigger FPGA is fully programmable through the VME interface. This makes the TOF LTM trigger layer really powerful, with 72 independent computing units.

Data from the 72 LTMs are sent to the CTTM through 60-metres long cables[42], each transmitting 24 signals and the sampling clock. A special cable has been designed in collaboration with the Amphenol Company, coupled to a Centronics 50-poles connector.

The LTM has been also designed to setup the thresholds to the FEA cards, sending through the FEACs a programmable voltage set by Digital-to-Analog Converters (DACs) mounted on the LTM boards. Moreover, the board will monitor both temperatures and low-voltages of the connected FEAC cards thanks to a set of Analog-to-Digital Converters (ADCs); this information is part of the TOF data payload.

Cosmic and Topology Trigger Module (CTTM)

The Cosmic and Topology Trigger Module (CTTM) [144] forms the second layer of the TOF trigger scheme. It is a king-size 78×41 cm^2 electronic motherboard (Figure 2.18) made to receive and elaborate the 1728 data bits from the 72 LTMs. Due to the large number of input signals (3456) and the large number of cables to be connected[43] a very large motherboard with 3

---

[41]The PDLs have been tested to work in a 0.5 T magnetic field with a ~ 100 Hz/cm^2 hadron exposition. Neither Single Events Upset (SEU) nor latch-up have been detected for a ~ 450 Gy absorbed dose (corresponding to more than 10 times the experiment's life). The magnetic field did not affect the PDL performance [145].

[42]A long R&D has been performed to ensure safe transmission of LVDS signals along 60 m cables.

[43]The input cables are connected on the back side of the motherboard.

Figure 2.18: The large Cosmic and Topology Trigger Module (CTTM) with its three piggy-back boards which host the FPGAs.

piggy-back boards, each hosting a FPGA, has been designed[44].

The aim of the CTTM is to elaborate a Level-0/Level-1 trigger decision on the basis of the data coming from the LTMs. The seven output signals feed the ALICE CTP (Central Trigger Processor) inputs using the LVDS standard. The trigger logic implemented in the CTTM FPGAs has the goal to select events on a multiplicity (i.e. pp minimum bias) and on a topology (i.e. pp jets) selection basis. Moreover, the implementation of quasi-vertical and back-to-back coincidences allows for cosmic-muon trigger

---

[44]The maximum number of user I/O pins for the FPGA available on the market is ~ 1200. Because of this limitation, the input signals are shared among two FPGAs to take a pre-trigger decision. The final trigger decision is then elaborated by the third FPGA.

Device	Quantity / SuperModule	Total quantity
FEAC	32	576
A1395	8	144
A1396	4	72
Custom crate	4	72
A3485A Power (three-channels)		12
A3485 Service (single-channel)		4
SY1527		4

Table 2.4: Relevant devices used for the ALICE TOF detector low-voltage system. The quantity installed on a SuperModule and the total quantity for the whole detector are quoted.

selection, which proved to be very useful during the detector commissioning. The trigger logic is programmable by configuring the three FPGAs through the VME interface implemented on the boards.

2.5 Services

In this section the services used by the ALICE TOF detector are described. They comprise low-voltage and high-voltage systems as well as the gas and cooling distribution systems. All the services have a modular design which allows to operate on small parts of the detector without interference to the rest. The control and monitoring operations are managed by the Detector Control System (DCS). The DCS is based on PVSS[45] to interface to all TOF detector subsystems [146].

2.5.1 Low-Voltage system

A schematic layout of the TOF Low-Voltage (LV) system is shown in Fig. 2.19. An original design has been adopted which is based on delivering to the electronics the power at relatively "high" voltage (48 V) using power supplies located outside the L3 magnet. Inside the magnet the 48 V voltage is converted, using DC-to-DC converters, to the required voltages very close

---

[45]A SCADA (Supervisory Control And Data Acquisition) system selected by CERN as the common platform for LHC experiments.
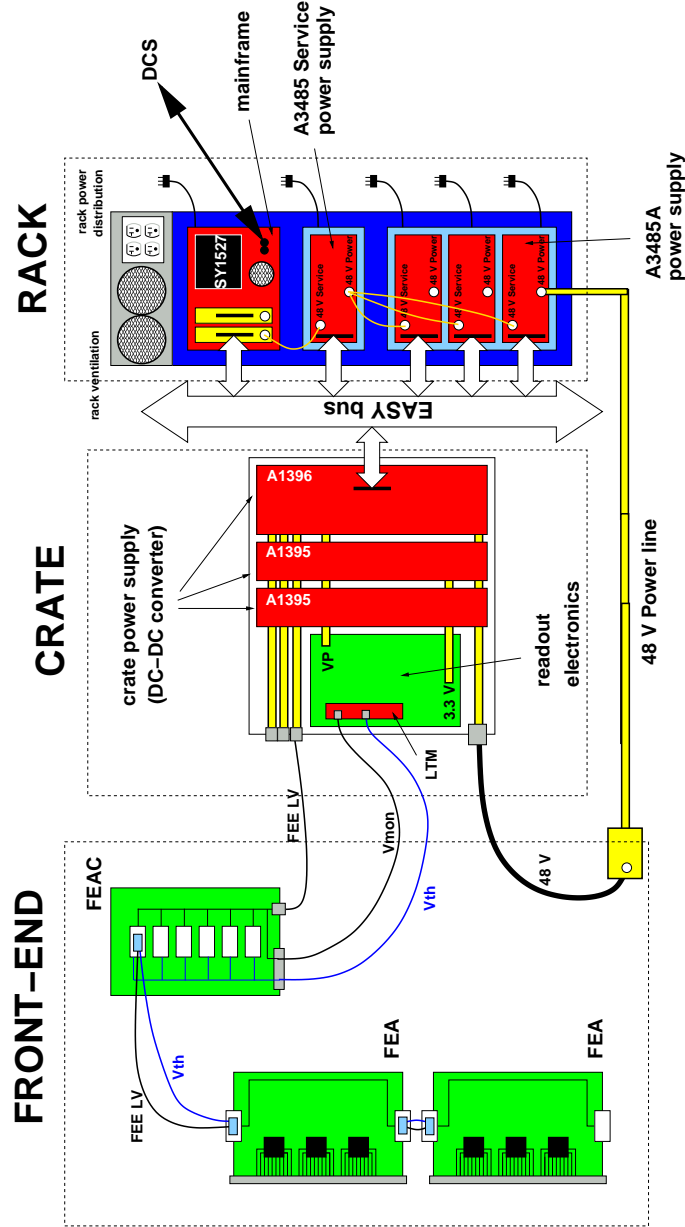
Figure 2.19: Schematic drawing of the ALICE TOF low-voltage system layout. Not all components and connections are shown. See text in Section 2.5.1.

Figure 2.20: One of the four ALICE TOF rack low-voltage subsystems with the SY1527 mainframe, the A1395-Service and three A1395A-Power power supplies.
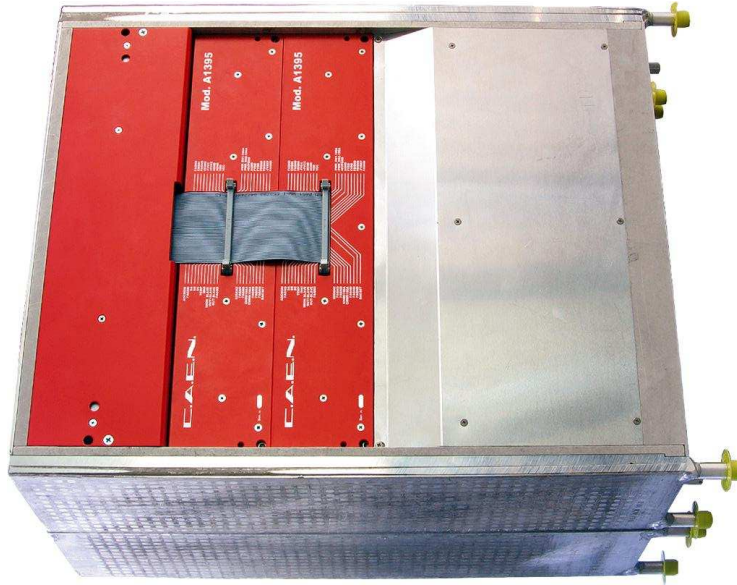

Figure 2.21: Top view of the ALICE TOF crate with the DC-to-DC converter power supplies installed: from left to right the A1396 and the two A1395s.

to the electronics. The DC-to-DC converters have been designed to work in a hostile environment, with a significant magnetic field (0.5 T) and moderate radiation level (1.2 Gy/10 years).

The LV system can be divided into two main zones: the rack LV system, located in the cavern outside the magnet, and the crate LV system, attached to the SuperModule.

The rack LV system is segmented into 4 independent subsystems each composed of a group of 19″-wide racks and several power supplies (Figure 2.20). All racks are equipped with a ventilation system to provide an adequate cooling to the power supplies and circuit-breakers for electrical protection. Each LV subsystem has a SY1527[46] mainframe to interface with the DCS for remote control and monitoring. Two A1676A "branch controllers" are installed in the mainframe to provide all devices with communication through the EASY bus[47]. A special power supply (A3485 Service), hosted in a single-channel unit, supply the 48 V service voltage required for communication to the subsystem. The service voltage is also provided to 18 crates inside the magnet along with EASY communication through control cables which enter the magnet. The main power supplies are three-channel units (A3485A Power), each channel being connected to a crate pair (left and right) through power cables which enter the L3 magnet. Three main power units are used for each LV subsystem for a total of 9 power channels.

Inside the magnet 72 DC-to-DC converter power supplies are installed in the TOF crates (Figure 2.21). Each crate power supply receives 48 V power voltage, service voltage and communication from the external LV system and is composed of a set of DC-to-DC converting devices: one A1396 and two A1395 boards. The A1396[48] has a GEneral COntroller (GECO) to interface with EASY communication for remote control and monitoring of the crate channels. It derives the LV for the front-end electronics (11 3.0 V, 7 A channels) and the VME bus (5 V, 7 A channel) and the volt-

---

[46]The CAEN SY1527 system is a commercial mainframe designed to house different boards with different functions. The high-voltage system of TOF makes use of this device as well.

[47]EASY (Embedded Assembly SYstem) is a CAEN low-voltage power supply designed for LHC experiment requirements (magnetic field and radiation tolerant). The A1676A branch controller remotely controls several "EASY crates" through the EASY bus. The same layout has been used for TOF power-supply communication.

[48]The A1396 board is a custom power-supply board made by CAEN S.p.A. for the ALICE TOF detector.

Device	Quantity / SuperModule	Total quantity
Module HV distribution	48	864
HV boxes	10	180
A1534P		16
A1534N		16
SY1527		2

Table 2.5: Relevant devices used for the ALICE TOF detector high-voltage system. The quantity installed on a SuperModule and the total quantity for the whole detector are quoted.

ages used for Actel FPGA programming[49]. The two A1395[50] boards work in parallel (master/slave) to supply the power required by readout electronics (Section 2.4.2). A single 3.3 V channel (200 A) is derived by the A1395s from the input power. It has to be pointed out that, despite a single 3.3 V channel is used for readout electronics, the VME boards are remotely controlled through the LV system thanks to a private bus; it is possible to switch on/off every single board.

The front-end electronics is connected to the crate power supply through 2-5 metres long cable, running along a half SuperModule. Each FEE LV channel ($\sim$ 2.7 V) feeds a FEAC card which in turn is connected to 12 FEA cards (Section 2.4.1). A total of 8 FEACs receive power from one crate, saving 3 spare FEE LV channels. Finally each FEAC receives from the LTM a threshold voltage, used in the FEA to setup the discriminator circuit (Section 2.4.1), and sends to the LTM a voltage monitor line (Section 2.4.3).

Table 2.4 summarizes the relevant devices used for the low-voltage system of whole detector and of the single SuperModule.

2.5.2 High-Voltage system

The TOF MRPC strips operate with a typical differential high voltage of ± 6.5 kV and are low-power devices (a few 10 nA/strip) with respect to

---

[49]All VME boards installed in the crate host an Actel FPGA which can be remotely programmed through the DRM. Special voltages (+16.3 V and -13.5 V) are required for this purpose.

[50]The A1395 board is a custom power-supply board made by CAEN S.p.A. for the ALICE TOF detector.
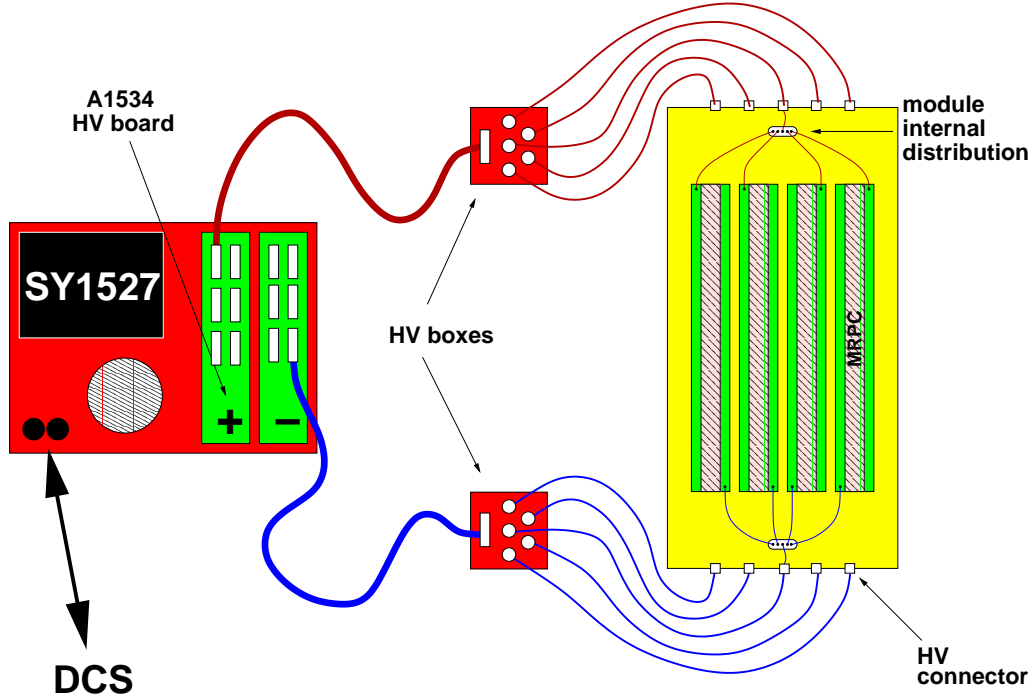
Figure 2.22: Schematic layout of the ALICE TOF high-voltage system. Only the basic elements of the system are shown. See text in Section 2.5.2 for details.

standard RPCs. A schematic layout of the High-Voltage (HV) system is shown in Fig. 2.22.

Standard high-voltage boards have been selected for the TOF HV system. They are housed into two SY1527 mainframes (Figure 2.23), located in the ALICE Counting Room 4 (CR4)[51]. The mainframe provides the interface with the DCS for remote control and monitoring of single-channel parameters (on/off, current, limits, trip, ...). 32 A1534[52] positive/negative HV modules, equally divided among the mainframes, are used for a total of 192 channels (including 12 spares). Two A1534 boards (A1534P and A1534N) feed the HV to 6 TOF modules (up to ±8 kV, 200 μA each channel). About 100

---

[51]The ALICE Counting Room 4 (CR4) is located in the main shaft of the experimental area, four floors underground.

[52]The A1534 is a CAEN commercial board with 6 HV floating channels. The output voltage range is 0-8 kV (200 μA maximum output current) with 0.5 V monitor resolution.
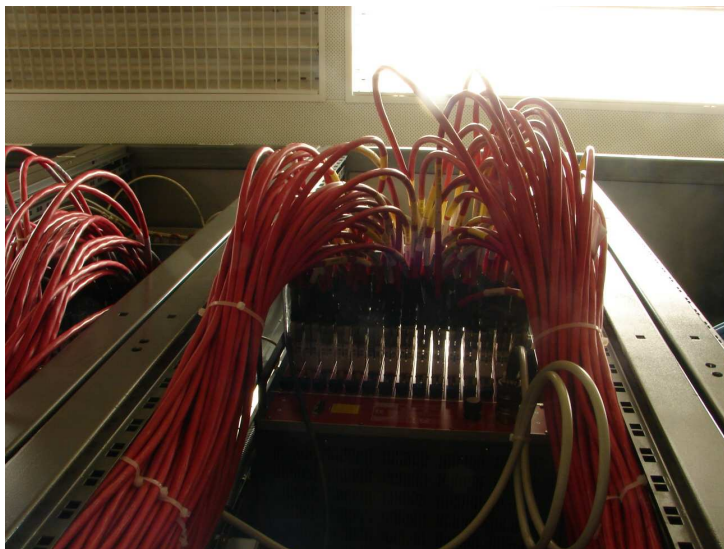
Figure 2.23: Back side of one of the SY1527 mainframes used for the high-voltage system with the cables connected to the high-voltage boards.
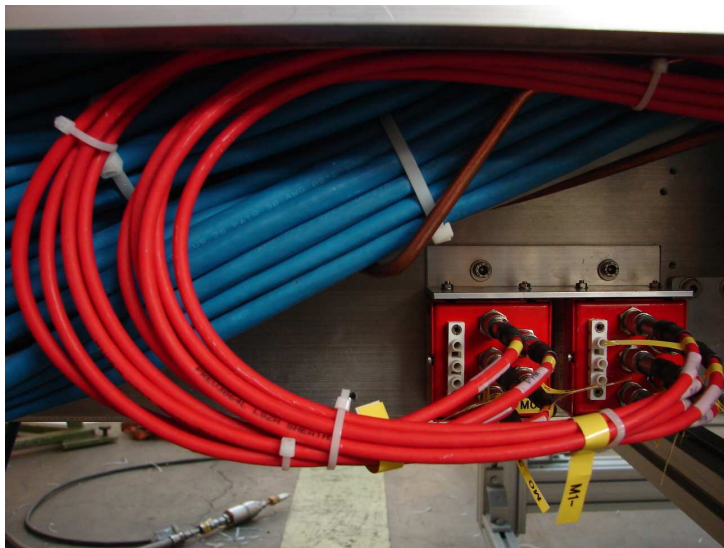

Figure 2.24: The SuperModules HV distribution boxes installed with cables going to the modules.
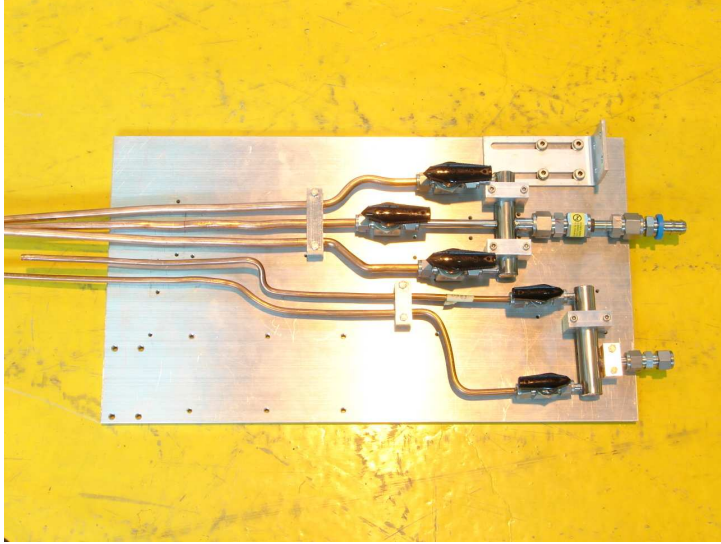
Figure 2.25: The gas and front-end water distribution system installed on TOF SuperModules near the crates. The valves to open/close the circuits are shown.

metres long cables, running from the CR4 to inside the magnet, connect the HV board outputs to the SuperModule HV distribution.

Inside the magnet a TOF SuperModule is provided with HV from CR4. A set of 10 passive HV boxes is located on both ends of the structure, sideways (Figure 2.24, Figure 2.11, Section 2.3.3). Each box receives the HV from one channel and splits it into 5 outputs. Two boxes (positive/negative) are used to feed a TOF module, that is two HV channels, through 2-5 metres long cables. The HV is then taken inside the module via "pass-through" HV connectors to the internal HV distribution which connects 3-4 MRPC strips (Figure 2.8, Section 2.3.2).

Table 2.5 summarizes the relevant devices used for the high-voltage system of whole detector and of the single SuperModule.

2.5.3 Gas system

The gas volume of the TOF detector is contained in 90 gas-tight boxes, the modules, for a total of about 18 m^3. A non-flammable freon-rich gas mixture containing $C_2H_2F_4$, i-C_4H_{10} and SF_6 (90%, 5% and 5%) is used. In

spite of the small volume of the detector, a closed-loop circulation system is used with a total flow rate of about 1 m³/h. Fresh-gas flow rate is about 0.02 m³/h to renew the mixture. The system is designed to provide the TOF detector with gas at working overpressure < 3 mbar.

Part of the gas system is located on surface in a dedicated building (gas mixing unit, purifier and gas recovery plant). The recirculation system is located in the main shaft of the experiment, below CR4. The final two distribution racks (top and bottom) are installed in the cavern at mid-height of the L3 magnet to best equalize the gas pressure for upper (top rack) and lower (bottom rack) sectors. 36 gas circuits branch from the racks to feed the SuperModules. Each gas segment is equipped with a flow measurement device for DCS monitoring. Two circuits are used for a SuperModule, reaching both sides of the structure. At the SuperModule level gas distribution among the modules occur: the circuit splits into subsegments. One subsegment feeds one module and is equipped with a valve to open/close the circuit (Figure 2.25, Section 2.3.3).

2.5.4 Cooling system

Proper cooling of front-end and readout electronics is needed to prevent damages/fire and to satisfy the temperature requirements of the ALICE central region (detector surface below 25°).

As all TOF electronics is located inside the L3 magnet water cooling is mandatory. The TOF cooling plant is placed inside the ALICE cavern at ground level. It has been designed to cool water down to about 15° C in a closed-loop circuit. It provides remote control and monitoring via DCS interface. An external water circuit ("chilled water") cools the hot water ("cooling water") coming from the electronics, without mixing. The cooling water is then divided into 12 independent circuits and sent with a pressure of about 2 bars to the detector. 6 "loops" are used to cool the TOF crates, each dealing with 6 half SuperModules (12 crates). The same segmentation is used for front-end electronics.

The special design of the TOF crate allows to cool the electronics housed in it by thermal contact with the walls (Section 2.3.4). Special attention has been used for heat dissipation while designing the readout electronics. It has to be kept in mind that a lot of HPTDC chips (up to 300) and the DC-to-DC converters are at work inside a crate, therefore cooling is an important issue

(a crate pair consumes about 1 kW) (Section 2.4.2).

Less crucial is the heat dissipation of the front-end electronics. The NINO ASIC is a low power consumption device, nonetheless water cooling is needed as the chip number is huge (more than 1000 NINO/SuperModule). Copper water pipes provide cooling to the front-end electronics (Section 2.4.1), with an independent circuit serpentine equipped with valves for each module (Figure 2.25, Figure 2.11, Section 2.3.3).

Chapter 3

Construction and tests

3.1 MRPC-strip mass production

During two years of MRPC mass production for the ALICE TOF array, about 1700 MRPC (Multigap Resistive Plate Chamber) strip detectors have been constructed at the INFN laboratories in Bologna (Figure 3.1), including some spare detectors.

To simplify, automate and speed up the production, a series of tools and procedures were developed. As an example, a washing/drying system has been used to clean the glasses used to define the MRPC gaps. The system consisted of an ultrasound tank, two rinsing water tanks, a water filtering complex and a oven, and allowed to clean and dry up to $\sim$ 100 glasses at the same time. Another improvement in the production rate was achieved with the construction of two semi-automatic machines[1]. They were built to run the fishing-line spacer across the width of the strips and could arrange a layer of spacer in only a few minutes.

The construction procedures were established during the construction of the MRPC prototypes, focusing in details on all the steps which, starting from single components, led to the final device. As a matter of fact, the production rate proved the effectiveness of these procedures which enabled

---

[1]The fishing-line machines were equipped with stepper motors driven by a computer numerical control (CNC). The layout of the fishing-line fibre layers was setup by programming the machine movements via a commodity PC. This allowed to easily implement also the "staggered" layout using the same machines.

Figure 3.1: The laboratory for MRPC strip production at the INFN in Bologna (picture by Antonio Saba).

to reach the maximum rate of 8 MRPCs completed per day[2]. Moreover, thanks to the clear assembly instructions, the construction technique resulted rather simple. A description of the assembly procedures can be found elsewhere [147].

As already pointed out in Sections 2.1.1 and 2.3.1, the TOF MRPC strips are based on commercially available components. This is clearly an advantage because, since most of the materials comes from the industrial production, their quality should already be well under control. Nevertheless, all materials and components used to build a MRPC were checked and selected before starting the assembly of a single detector. Moreover, every single chamber underwent a long set of quality checks. This has guaranteed the uniformity in the production and in the detector performance. A set of quality assurance procedures has been established for this purpose which also comprises specific

---

[2]The production rate was not constant during the two years of MRPC mass production because other activities had to be carried out in parallel. As an example, people had to be trained before being able to build the detectors and to perform the quality assurance tests. Moreover, when the TOF modules production started, the MRPC production rate slightly decreased. The maximum rate of 8 MRPCs per day was reached before starting the module assembly, in the last period of the construction.
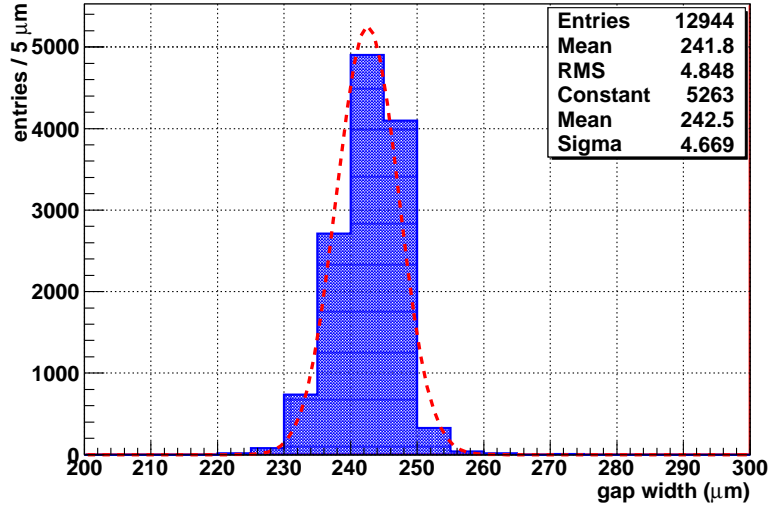
Figure 3.2: MRPC-strip gas-gap width measurements.

tests that have been performed on smaller samples. They are outlined in the following sections, but a detailed description of their implementation can be found in [148]. Thanks to all these procedures only a fraction of about 1.5% of the MRPCs produced was rejected.

3.1.1 Quality assurance tests

The great challenge of the MRPC-strip mass production was to guarantee the excellent performance obtained with the detector prototypes [149]. Moreover, uniformity of the performance among all produced detectors was another major goal. A set of quality assurance procedures has been developed for these purposes; these have been applied both to the single components and to the whole assembled MRPC detectors [150].

Components

All glasses used to build a MRPC have been cleaned in an ultrasound bath, rinsed and dried. The rigid components of the chambers (i.e. honeycomb panel and printed circuit boards) where checked for planarity in order to reject those which were not planar enough and those which had shown
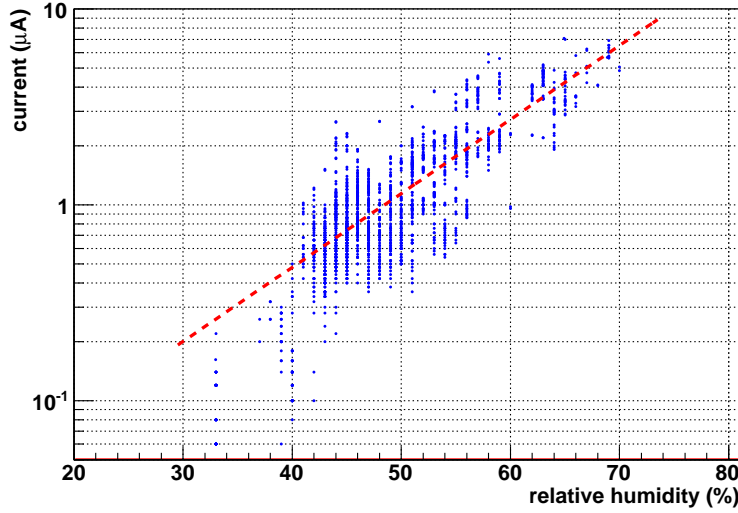
Figure 3.3: MRPC current measured during high-voltage test in air at
± 3 kV as a function of the relative humidity.

construction faults. The resistive coating which covers the external surface
of the MRPC outer plates (HV electrodes) has been measured and monitored
with time. Measurements in five different positions have been done on each
"painted" glass and recorded in a database to ensure good uniformity of the
paint. Only glasses with a standard deviation of the five measurements σ be-
low 25% of the mean value μ ($\sigma/\mu < 0.25$) and with mean resistivity within a
preset range have been used; studies have shown that acceptable mean values
range from about 2 MΩ/□ to about 25 MΩ/□. Then, groups of four glasses
with very similar characteristics have been selected for each MRPC in order
to guarantee the highest uniformity within the same detector.

Assembled detectors

After the MRPC assembly procedure, the global outer plate resistance
was measured again to ensure the integrity of the electrodes themselves. A
breaking of the glass or a bad contact with one or both of the high-voltage
pads would have show an infinite resistance[3]. Since a large number of solder-

---

[3]Although the breaking of a MRPC electrode glass would have caused a MRPC to be
rejected, in most cases the chamber functioning is still guaranteed. The high voltage is

ings (more than 1600) were welded by hands to complete a MRPC strip, the quality of the solder points (cathode-anode connecting pins and flat-cable connectors) must be checked. This was performed by applying a reference voltage and comparing the measured values with the expected ones. Short-circuits as well as bad solderings could be identified and fixed immediately. The gas-gap widths have been measured by means of a high-resolution analog CCD camera coupled to a microscope in different positions along the strip and in both stacks (Figure 3.2). Both the check of solderings and the measurement of gap widths have been performed by semi-automatic procedures. Finally, high-voltage tests have been done applying up to ± 3 kV to the electrodes in air and measuring the relative humidity during the test (Figure 3.3); the measured currents are strongly correlated to the relative humidity: negligible current values result for MRPCs tested in a dry environment. High-voltage supply was controlled through a SY2527[4] mainframe and positive/negative commercial HV boards. All these measurements have been stored in a database.

It is worth noticing the remarkable uniformity achieved in the construction of the detectors, which is especially stressed by the narrow distribution of gas-gap widths (Figure 3.2). In fact, the r.m.s.[5] of this distribution is $\sim 5~\mu$m which includes, besides the fishing-line width, also the resolution of the microscope-CCD acquisition system.

3.1.2 Cosmic-ray tests

During MRPC construction, some of the produced detectors underwent cosmic-ray tests. Three chambers at a time were randomly selected and exposed to cosmic rays at the INFN laboratories in Bologna[6]. The test facility would allow for the simultaneous test of up to 5 detectors, but two reference ones have been kept fixed in all tests for a direct comparison of the performance measured in the facility. These reference MRPCs, previously tested at the CERN PS during Summer 2004, also allowed to carry out a sort

---

applied on both edges of the electrodes, thus a glass breaking does not necessarily imply a loss in electric field. However, if the glass breaks in different positions, there could be a region without field.

[4]Commercially available device, produced by CAEN S.p.A.

[5]Root mean square.

[6]Cosmic tests have also been carried out on a few detectors which have shown construction defects. They have demonstrated to have the same high performance, nevertheless.
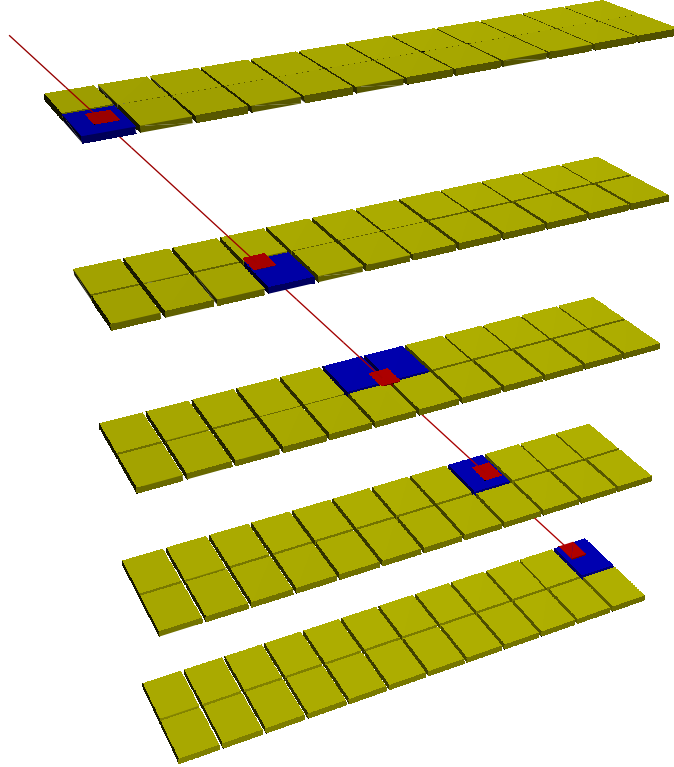
Figure 3.4: Event display of a cosmic ray recorded within the MRPC test facility in Bologna.

of ageing test in our laboratory, since they were kept active inside the gas mixture for more than 2 years. In fact, they were tested again at the CERN PS in November 2006, showing the same excellent performance obtained in the previous test beam [151].

Experimental setup

The experimental setup consisted of a gas-tight aluminium box, containing the detectors, and a readout system. The aluminium box, which defined the gas volume and provided the required connections with the external services (high voltage, front-end electronics), allowed to house up to 5 MRPC strips in a stack. The gas mixture used during these tests was the standard one ($C_2H_2F_4$/i-C_4H_{10}/SF_6, 90%/5%/5%) and the detectors were operated

HV = 13 kV Th = 250 mV

Mean	99.04
RMS	0.3721

HV = 13 kV Th = 250 mV

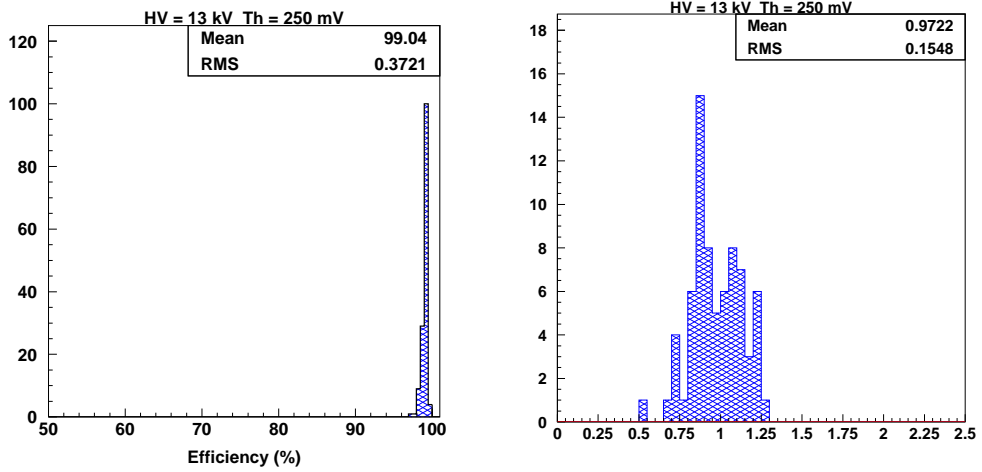| Mean	0.9722
RMS	0.1548

Figure 3.5: Efficiency (left) and normalized time resolution (right) measured in the MRPC cosmic-ray facility in Bologna. The time resolution has been normalized to the resolution of the reference MRPCs, measured to be about 50 ps at the test beam.

at ± 6.5 kV.

A readout electronics based on the HPTDC chip[7] was used for time digitization of the signals. The trigger to the system was provided by the MRPC themselves through the LTM prototype[8]. Five NINO ASIC Front-End Analogue (FEA) cards[9] were used to amplify/discriminate the differential signals coming from the MRPCs, each attached to a different strip, for a total of 120 readout channels.

Results

The data were collected and recorded on a LINUX PC used also for monitoring purposes. It is worthwhile to say that during data analysis the

---

[7]A previous version of the readout system was based on commercially available CAMAC boards. The last and more widely used readout system was based on the prototypes of the ALICE TOF TDC Readout Module (TRM).

[8]Like the readout system, the LTM prototype has replaced the old trigger coincidence, based on CAMAC boards.

[9]In the previous version of the facility five prototype front-end cards were used, based on discrete amplifier/discriminator components (MAXIM).

tracking was performed using only the spatial information provided by the MRPC themselves, thus with limited precision (Figure 3.4). The results in terms of measured efficiency and resolution obtained with a sample of MRPC strips are shown in Figure 3.5.

3.1.3 Test beam results

During the autumn of 2006 a final test of a sample of double-stack MRPC (Multigap Resistive Plate Chamber) strips, randomly chosen from two years of mass production, was carried out at the CERN Proton Synchrotron (PS) facility. The results on the performance of the MRPCs coupled to the final front-end and readout electronics are presented, together with other measurements.

Experimental setup

The experimental setup was located at the PS-T10 beam line. A 7 GeV/c negative beam (mainly pions and muons) was tuned to perform the measurements with minimum ionizing particles (MIP). A trigger area of ~ 1 cm^2 was defined by the coincidence of two pairs of crossed scintillator finger counters, placed upstream and downstream the detector under test. The reference time, needed for time-resolution studies, was provided by two fast scintillator bars with 30 ps resolution. Each scintillator bar ($2 \times 2 \times 10$ cm^2) was equipped with two photomultipliers, so the reference time was computed as the mean of the four measurements.

The MRPC strips under test were put inside a gas-tight aluminium box which could host a stack of up to 5 detectors. The box, which provides the required interface between the devices, high voltage and front-end electronics, was installed on a moving frame in such a way that the beam crossed all five strips. This allowed to perform the measurements on five detectors at a time. The moving structure enables to remotely displace the aluminium box with respect to the beam position, thus allowing to perform position scans without entering the experimental area[10]. The detectors were fed with high voltage through the box which was filled with the standard gas mixture ($C_2H_2F_4$/i-C_4H_{10}/SF_6, 90%/5%/5%).

---

[10]The mechanical frame used to support the box was equipped with stepper motors. It allowed for remote control of the moving with millimetric accuracy.
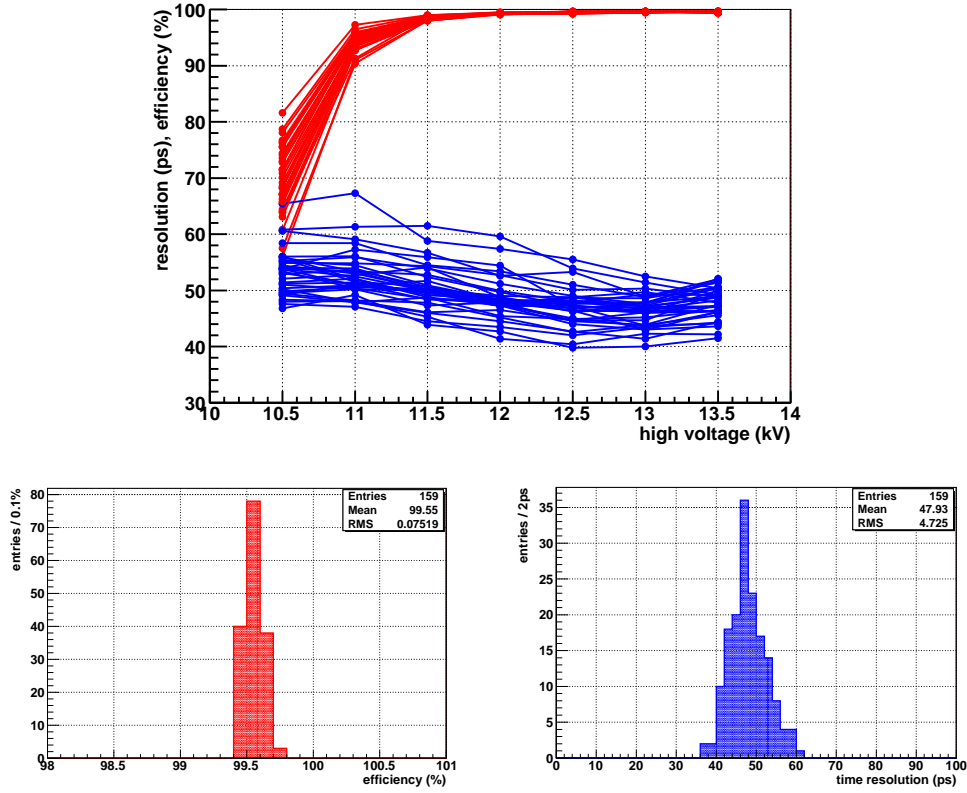
Figure 3.6: Efficiency and time resolution measured at CERN PS beam line. High-voltage scan (top). Efficiency (bottom left) and time resolution (bottom right) at a fixed high voltage of 13 kV.

The readout of the signals from the MRPCs has been performed using the final front-end and readout electronics through the complete readout chain. Five NINO ASIC FEA cards were used to amplify/discriminate the differential signals from the strips and one FEAC was used to provide them with the low voltage and threshold voltage (Section 2.4.1). The final TOF VME custom crate (Section 2.3.4) was used to host the readout boards. A TDC Readout Module (TRM) with HPTDC chips was used to readout both MRPC and reference scintillator signals[11] and a LTM board provided the

---

[11]A NIM-to-LVDS converter board has been used to interface the output of the discriminators used for the photomultipliers and the TRM.

front-end electronics with a programmable voltage to setup the discriminator threshold (Section 2.4). Both the readout system and data acquisition were controlled by a LINUX PC through a V2718[12] VME bridge-board installed in the crate.

Results

Several MRPC channels were tested varying the applied high voltage to measure efficiency and resolution. The results are shown in Figure 3.6. These measurements allowed to select the best working voltage at 13 kV. More pads have been then tested with fixed high voltage and the results are also presented in Figure 3.6. Very good performance has been measured, with efficiencies higher than 99% and mean time resolution better than 50 ps. Moreover, the devices have shown an impressive uniformity in the performance, reflecting the characteristics of the whole mass production.

The data collected varying the applied high voltage have also been analyzed in order to evaluate the time-shift as a function of the applied high voltage. The following correction functions were introduced and applied to the data

$$
\begin{aligned}
f(TOT, HV) &= f_{slew}(TOT) + f_{HV}(HV) & (3.1) \\
f_{slew}(TOT) &= S_1\, TOT + S_2\, TOT^2 + S_3\, TOT^3 & (3.2) \\
f_{HV} &= K_1\, HV + K_2\, HV^2, & (3.3)
\end{aligned}
$$

where TOT is the Time-Over-Threshold measurement and HV is the high-voltage value. A global fit on the data returned the function parameters S_i and K_i. Special attention has been used to evaluate whether the same time-amplitude (Time-Over-Threshold) correction function applies to different HV data. The results are shown in Figure 3.7 confirming also that a unique time-slewing correction function can be used at different high-voltage values (i.e. gain factor). Moreover, the time-shift has been measured as a function of the applied high voltage. The same analysis has been performed on data collected

---

[12]The V2718 is a commercially available VME master module produced by CAEN S.p.A. The connection between the V2718 and a standard PC takes place through an optical fibre cable interfaced by a PCI controller card A2818, also produced by CAEN. Some special modifications have been done on the V2718 board to send triggers to the TRM boards, in order to mimic the DRM board.
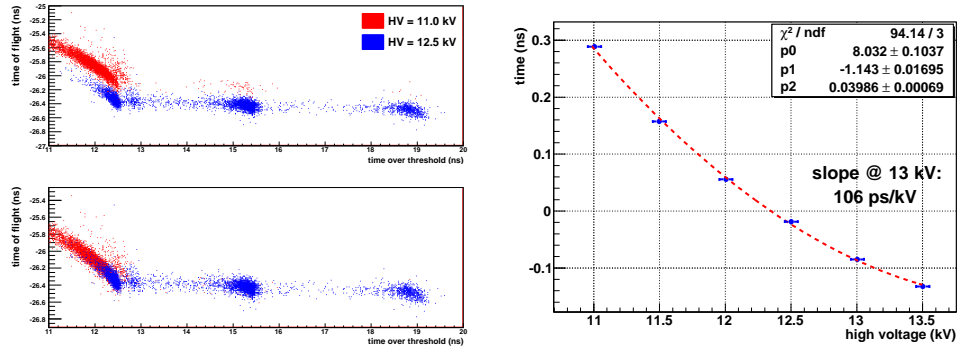
Figure 3.7: High-voltage time-shift measured at CERN PS beam line: Time-Amplitude (Time-Over-Threshold) correlation at different high voltage before (top left) and after (bottom left) correcting for high-voltage time-shift; time as a function of the applied high voltage (right).
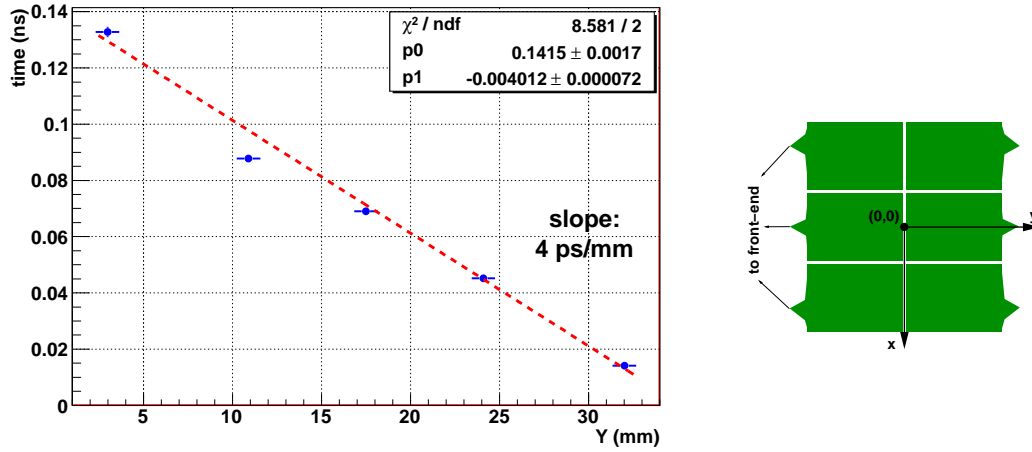

Figure 3.8: Vertical scan of one pad. The measured time is shown as a function of the beam position (time-walk).
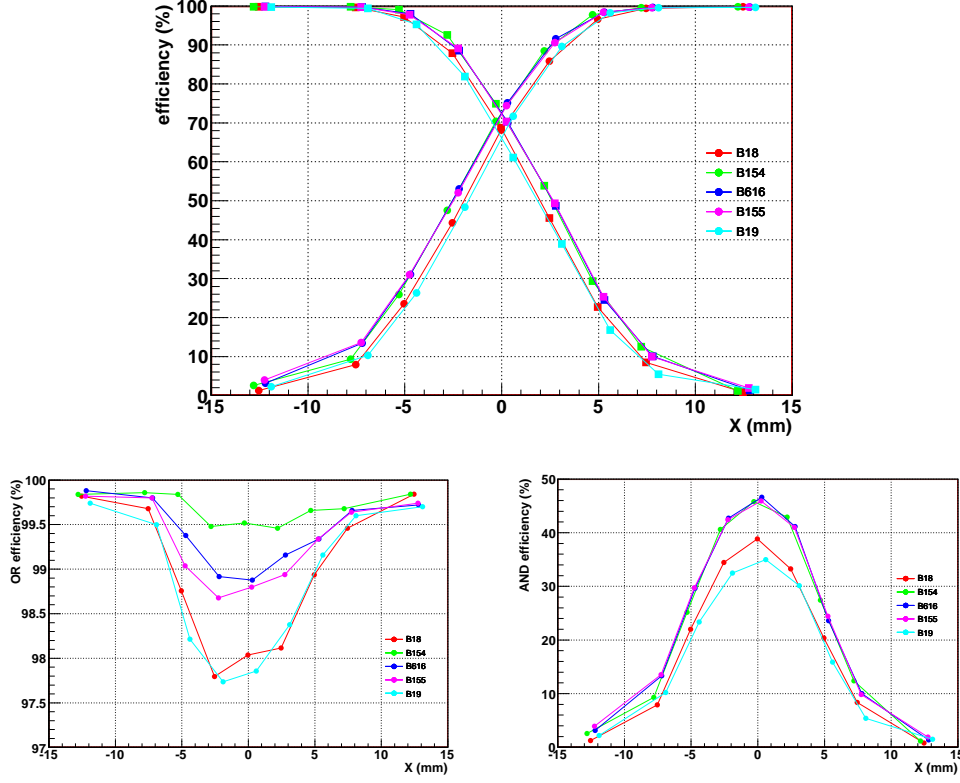
Figure 3.9: Horizontal scan of two neighbouring pads: single-channel efficiency (top); OR efficiency (bottom left); AND efficiency (bottom right). Position zero is located between the pads.

at fixed high voltage varying the beam position in the vertical direction, across the length of the strip (Figure 3.8).

Finally, a horizontal scan along the length of the strip has been performed moving the beam spot from one pad centre to the neighbouring one (Figure 3.9). When looking at these results one should keep in mind that the trigger area was of about 1 cm^2, thus an ultimate conclusion on border effects, which are connected to the avalanche footprint, cannot be taken. Nonetheless, it should be noticed that high efficiency > 98% is attained also in between two pads when considering the OR of the two channels; this makes the TOF MRPC strip a detector with practically no dead area.

3.2 Module construction

The assembly of the 90 modules which form the ALICE TOF array was carried out at the INFN laboratories in Bologna. Spare modules have been also produced, filling them with the spare MRPCs.

The TOF modules are described in details in Section 2.3.2. The steps which led to the construction of a module can be divided into two sets: the assembly of the module itself, that is the empty gas-tight box, and the installation of the MRPC strips inside the gas volume. Quality assurance procedures have been established to control both processes by checking single components and the behaviour of the fully assembled device. Tested modules were brought to CERN where SuperModule assembly has been done. To ensure that no damage occurred during the transport operation over about 600 km, further checks were performed at the arrival at CERN. Eventually, the final global check with cosmic rays was performed in a dedicated test facility to validate the detector functioning.

3.2.1 Quality assurance tests

A set of quality assurance procedures has been established also for TOF modules. The goal is to guarantee the perfect functioning of the MRPC strip detectors arranged inside the module box as well as to guarantee good mechanical (gas-tightness) and electrical (to avoid discharges) performance. The tests have been performed in Bologna to check both the single components and the modules after the MRPC insertion. Since the modules have been all brought to CERN for the further assembly procedure, other tests have been performed there.

Tests performed in Bologna

All printed circuit boards, which interface the gas volume with the front-end electronics, were glued on the aluminium backbone of the modules. They were tested before gluing to check the electrical connections and were checked again after gluing to ensure that no glue had covered the connector pins. An electronic device has been constructed to semi-automatize this process.

Gas tightness is a major requirement for the TOF modules, though the chambers work at atmospheric pressure. Gas leakage measurements were
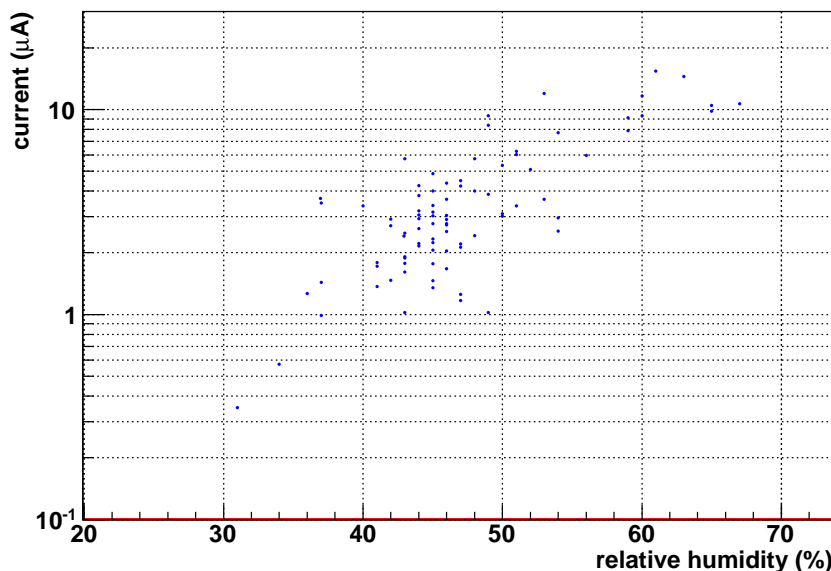
Figure 3.10: Module current measured during high-voltage test in air at ± 3 kV as a function of the relative humidity.

performed on each module and were repeated several times: after the assembly of the module box itself, after the installation of the MRPCs, after the transport at CERN and before assembling the SuperModule. The tests were performed by increasing the pressure of the volume of about 10-20 mbar (with respect to the atmospheric pressure) and measuring with a barometer the rate with which the overpressure decreases. The maximum accepted rate of leakage was 1 mbar/h per module, corresponding on average[13] to about 0.17 l/h per module. A mean value of ~ 0.2 mbar/h was achieved, with most of the modules well below this value.

The high-voltage connectors, which bring the high voltage inside the gas volume, represent another potentially weak point of a module. They are glued onto the aluminium plane in such a way that a copper wire, surrounded with a certain amount of insulating plastic, can enter the gas volume. The wire passes very close to the module ground-voltage plane (the aluminium plane),

---

[13]Different module types have different gas volumes being about 240 l, 200 l and 93 l for external, intermediate and central modules, respectively.

therefore an electrical discharge could occur in the presence of construction defects. Firstly, a high voltage of 8 kV was applied to all HV connectors, without connecting any MRPC, to check the electrical strength of the insulators. Secondly, after connecting all the MRPCs to the high-voltage distribution system, described in details both in Section 2.3.2 and 2.5.2, a further test up to $\pm$ 3 kV in air is performed. In Figure 3.10 the results of the module high-voltage test in air are shown; the measured currents depend on the humidity of the laboratory, as already pointed out for the MRPCs (Section 3.1.1).

The capacity of each MRPC was measured before installing it inside the modules and connecting it to the high-voltage system. When all MRPCs were in place, the capacity was measured through the high-voltage connector, which groups the MRPCs in clusters of 3-4 detectors. The measured capacity had to be the sum of the single detector capacities. Any deviation indicates that some connection has not been properly done.

Finally, all the connections from the MRPC readout pads to the interface card connector, which houses the front-end card, have been tested at the module completion. A pulse test signal was sent inside the module to the MRPC pulse line (Section 2.3.1) which makes the readout pads generate an output signal. The output signal is then collected through the complete chain by a front-end electronic card plugged into the interface card connector to evaluate the connection status. Also in this case, a semi-automatic facility enabled to speed up the test.

Tests performed at CERN

At the arrival of a module at CERN this was immediately checked to evaluate accidental damages occurred during the transport. Gas tightness, MRPC group capacity and pulser measurements were performed again before the final test with cosmic rays occurs. Once the module has been tested it was flushed with the final gas mixture and installed on a big frame, the cosmic telescope, together with other four modules. In case no room was available on the cosmic structure because the test on the previous batch of modules was still ongoing, the module was put on a storage frame waiting for the cosmic facility.

The module Cosmic-Ray Test Facility (CRTF) is described in details in the following section. The analysis framework and technique and the results obtained with a batch of five modules are discussed as well.

3.2.2   The cosmic-ray test facility

The last test on TOF modules is performed at CERN in a fully equipped Cosmic-Ray Test Facility (CRTF) with the complete electronic chain used in the experiment. A description of the CRTF is also given in [152].

Experimental setup

The module test facility was mainly made of a big frame which can host a stack of up to 5 modules, that is a complete TOF-sector. The frame was equipped with two scintillator layers, each of them made of an array of the new generation START counters [153, 154] to provide trigger information to the data acquisition (Figure 3.12). Figure 3.11 and 3.13 show a picture and a scheme of the facility, respectively.

The most important feature of the CRTF was that it allowed to study the TOF module performance in the same conditions of the ALICE experiment: all the systems were in their final version, from the high- and low-voltage distribution systems to the complete electronic readout chain (Figure 3.12). In particular, concerning the electronic side, the CRTF was made of[14]:

- 90 FEA (Front-End Analogue) cards with three NINO ASIC chips each;

- 10 FEAC (FEA Controller) cards to distribute low voltages and thresholds to the FEA cards;

- a VME custom CRATE with water cooling system;

- a CAEN V2718 optical VME bridge to access the VME bus;

- a LTM (Local Trigger Module) card to set FEA thresholds and read FEA OR signals;

- a CPDM (Clock and Pulser Distribution Module) to distribute the clock to the TRMs;

- 9 TRM (TDC Readout Module) cards with 30 HPTDC (High-Performance Time-to-Digital Converter) chip each,

---

[14]A detailed description of the electronics used during these tests can be found in Section 2.4.

Figure 3.11: The big cosmic-ray frame with 5 TOF modules and the signal cables which go from the FEA cards to the readout electronics.
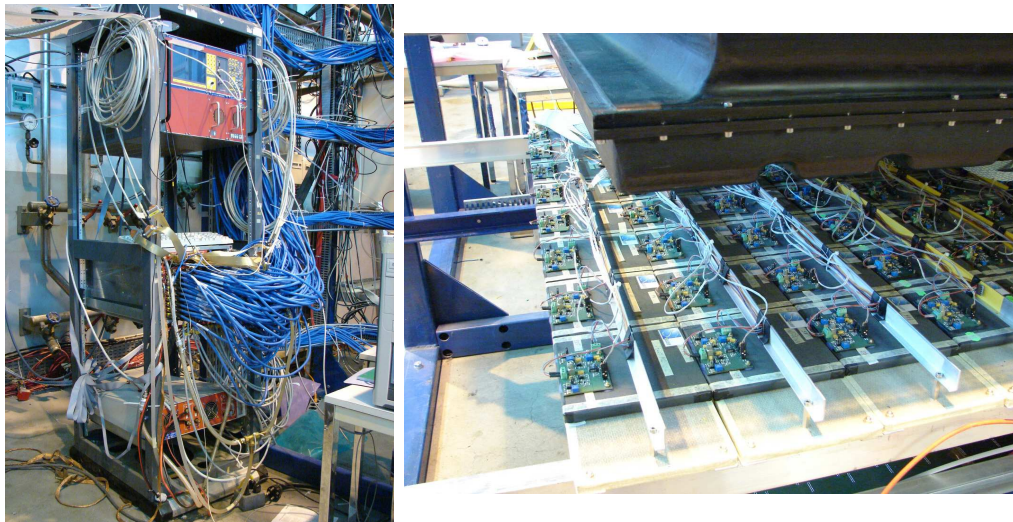
Figure 3.12: The CRTF readout electronics with signal cables plugged in the TRM boards (left). The lower trigger plane with the array of START scintillator counters (right).

and allowed to test simultaneously up to 2160 readout channels, that is 25% of a TOF sector channels. The data acquisition (DAQ) and the online monitoring systems were managed respectively by DATE v5.16 and MOOD, both used in ALICE, running on a LINUX (SLC3) PC equipped with a PCI optical link.

Analysis framework

The TOF module geometry with tilted MRPCs required the development of a simple basic structure able to analyze the data collected with the CRTF in its different configurations. The three kinds of modules were fully reproduced in their geometrical aspects and put into the CRTF analysis framework: this provided, for instance, information on the spatial position of all the channels; therefore further complicated tracking algorithms were not needed. Indeed, because of the cleanliness of the recorded events, the tracks were reconstructed by using the linear regression method in three dimensions. The developed framework also allowed to find the particle impact point on the chamber under test, that is the channel crossed by the cosmic ray, if any. Despite the complicated geometry of the CRTF this could be

Figure 3.13: Scheme of the CRTF showing the position of TOF modules and of the START trigger scintillator layers.

achieved thanks to the addition of a Track-Propagation Engine (TPE) inside the analysis framework. Once a track is reconstructed the TPE propagates it through the simulated geometry and finds all the crossed active areas. Figure 3.14 shows an event display of a recorded cosmic-ray event within the analysis framework.

An important feature of this framework consisted in its accurate representation of the CRTF, that is the module geometry. This allowed to evaluate the behaviour of the test facility by simulating cosmic-ray events and analyzing them in the same fashion of the effective recorded events. It has to be noticed that the only tracking system inside the CRTF were the modules themselves and that their space resolution is limited by the channel size: 2.5×3.7 cm^2. The track reconstruction has been done using only 4 layers with roughly 1 cm space-resolution each and no information from the module under test was used for tracking. This led to a impact point resolution of ~ 0.5 cm which is not so small. By simulating cosmic events in a fully efficient CRTF provided a measurement of space-resolution effects on the efficiency and allowed both to predict the effective results and to compare them with the simulated ones.

Results

During July 2006 the modules of the second TOF sector, called Super-Module 2 (SM2), were tested in the CRTF. The data taking took about 15
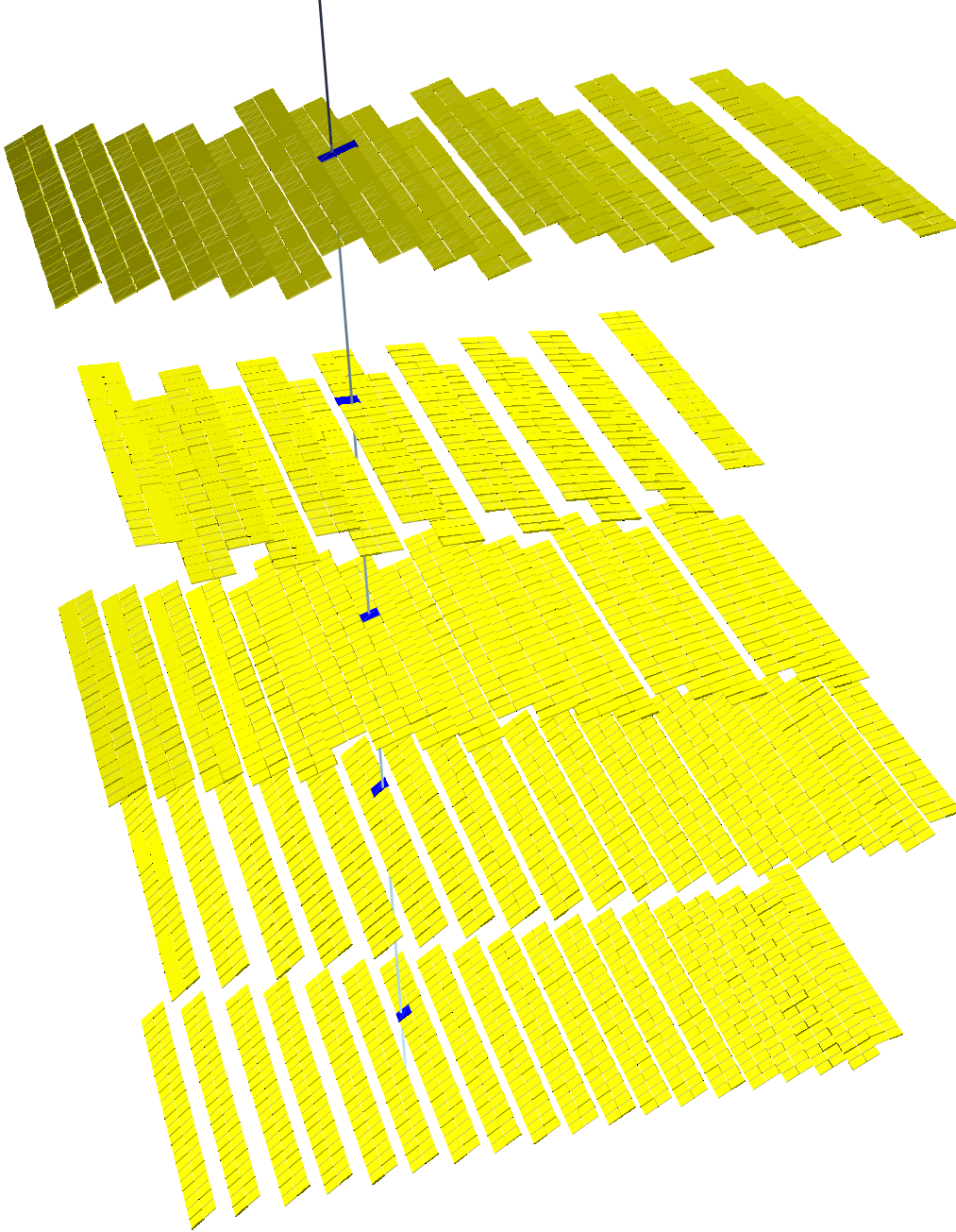
Figure 3.14: Event display of a recorded cosmic-ray event in the CRTF within its analysis framework. The tiny dark shaded areas represent the fired channels, while the straight line represents the reconstructed particle track.
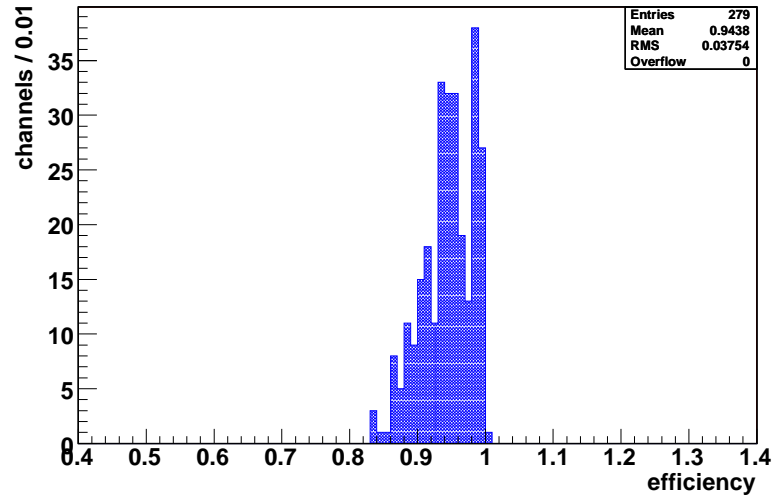
Figure 3.15: Results of real cosmic events on an intermediate module (TI3). Only the measured efficiencies of the tested channels with at least 100 reconstructed events are shown.
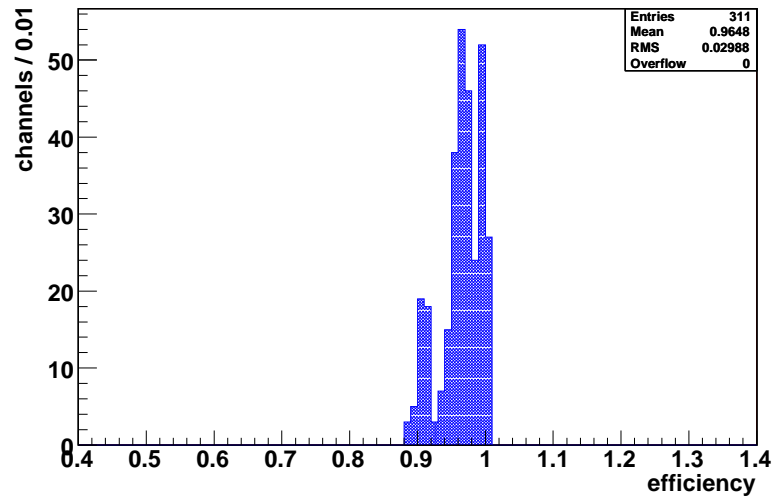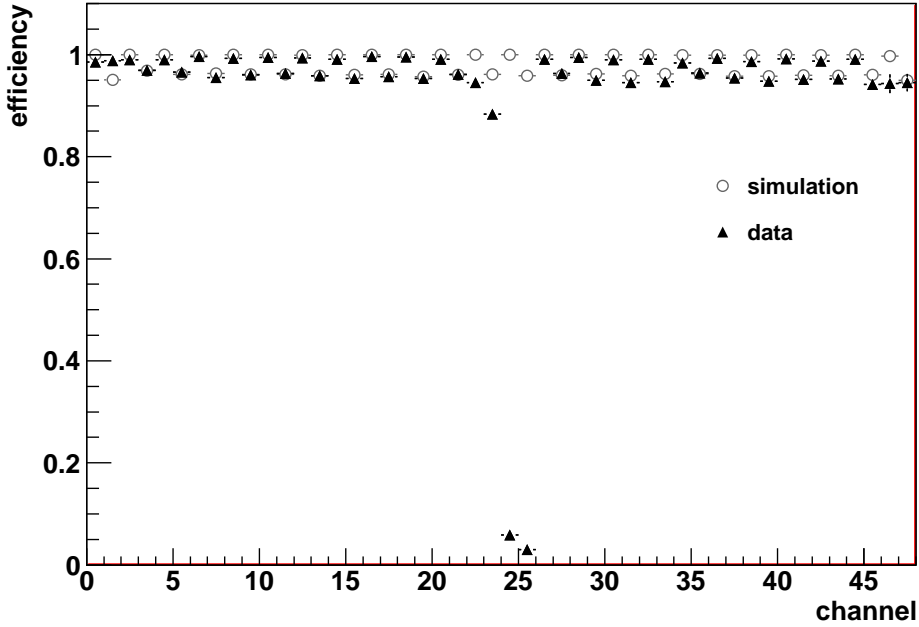

Figure 3.16: Results of simulated cosmic events on an intermediate module (TI3). Only the measured efficiencies of the tested channels with at least 100 reconstructed events are shown.

Figure 3.17: Efficiency measurements of a single (half) MRPC strip within the module CRTF which highlights an efficiency loss in two channels due to a badly plugged in front-end card. Both real- and simulated-data results are shown, indicating their good agreement.

days and more than 5 million cosmic-ray events were collected. The modules were fluxed with a gas mixture of 93% $C_2F_4H_2$ and 7% SF_6 and the high voltage was set to 13.5 kV on all of them. Table 3.1 shows the module positions, according to the CRTF scheme in figure 3.13, and the tested module names, where TE, TI and TC stand rispectively for TOF-External, TOF-Intermediate and TOF-Central module. The efficiencies of all the tested channels were computed and the mean module efficiencies $\bar{\varepsilon}_{data}$ are reported in Table 3.1. Figure 3.15 shows the efficiencies of the tested channels of an intermediate module (TI3).

The analysis framework was also used to study the behaviour of a fully efficient test facility by simulating 10 million cosmic-ray events which were analyzed in the same way as the effective recorded data. The efficiencies

Module	Name	$\overline{\varepsilon}_{\mathrm{data}}$ (%)	$\overline{\varepsilon}_{\mathrm{simulation}}$ (%)	$\widetilde{\varepsilon}_{\mathrm{module}}$ (%)
0	TE3	78.8 ± 0.4	83.2 ± 0.4	94.7 ± 0.7
1	TE4	92.1 ± 0.3	93.6 ± 0.2	98.4 ± 0.4
2	TI3	94.4 ± 0.2	96.5 ± 0.2	97.8 ± 0.3
3	TC2	97.7 ± 0.2	99.2 ± 0.1	98.5 ± 0.2
4	TI4	90.5 ± 0.2	92.7 ± 0.3	97.6 ± 0.4

Table 3.1: Summary of the results on the SM2 modules. Their positions in the CRTF, names and efficiencies (mean data efficiency, mean simulation efficiency and estimated efficiency) are reported.

of all the channels in the simulated facility were computed and the mean module efficiencies $\overline{\varepsilon}_{\mathrm{simulation}}$ are reported in Table 3.1. Figure 3.16 shows the efficiencies of the tested channels of the same intermediate module (TI3) and has to be compared with figure 3.15. The agreement between recorded and simulated data is quite good. The good agreement between real data and simulated data is clearly evident in Figure 3.17, where the measured efficiencies of a half MRPC-strip channels are reported; the observed behaviour is well reproduced by the simulation.

Both the results of the mean efficiencies obtained from real data taking and of the mean efficiencies obtained from the simulation were used to evaluate the effective module mean efficiencies. Since in the simulation the active areas were assigned a 100% efficiency their measured performance $\overline{\varepsilon}_{\mathrm{simulation}}$ gives a quantitative means to obtain an estimate of the effective module mean efficiency $\widetilde{\varepsilon}_{\mathrm{module}}$. The effective module mean efficiencies $\widetilde{\varepsilon}_{\mathrm{module}}$ were estimated simply via

$$\widetilde{\varepsilon}_{\mathrm{module}} = \frac{\overline{\varepsilon}_{\mathrm{data}}}{\overline{\varepsilon}_{\mathrm{simulation}}} \tag{3.4}$$

and the results are shown in Table 3.1.

3.3   SuperModule assembly

The last step which led to the completion of the ALICE TOF detector was the assembly of the 18 SuperModules. Five modules are grouped in a rigid aluminium structure, which ensures the mechanical robustness necessary to handle and install the detector inside ALICE. A comprehensive description of the SuperModule structure has been already given in Section 2.3.3.
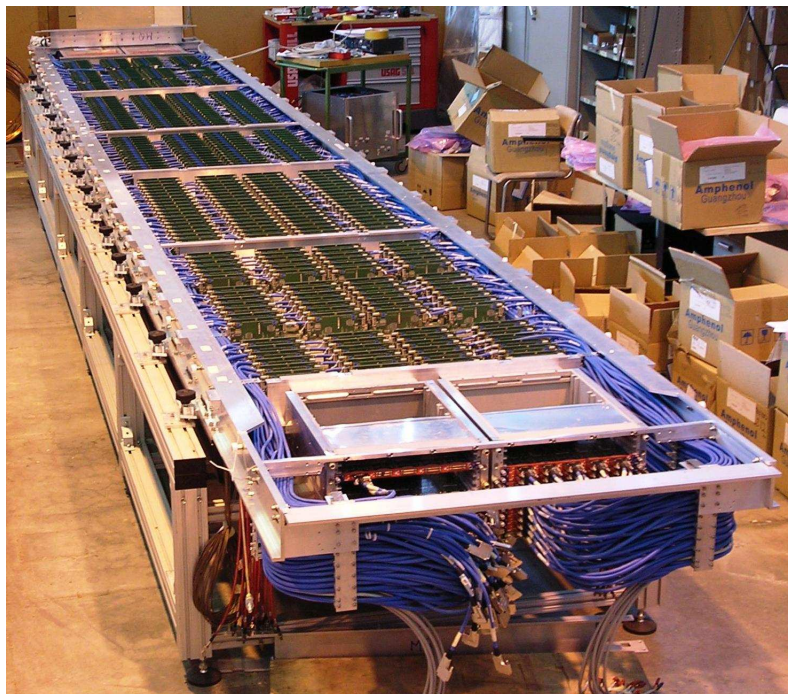
Figure 3.18: A TOF SuperModule during the assembly on the support frame.

The assembly of TOF SuperModules was carried out at CERN, where TOF modules were delivered after completion. Two special frames have been constructed to support the modules during the assembly procedure and to support the whole structure before moving it. They allowed the construction and test of two SuperModules at the same time. Another set of frames has been used to store the SuperModules after finishing all the quality assurance tests. They allowed to store up to 8 TOF sectors waiting for the installation in the experimental area. Figure 3.18 shows a SuperModule during the construction laid on the assembly frame.

3.3.1 Quality assurance tests

The first quality check on SuperModules was applied well before the actual start of the structure assembly. Gas tightness of the five modules was checked as soon as the modules were put on the assembly frame. The
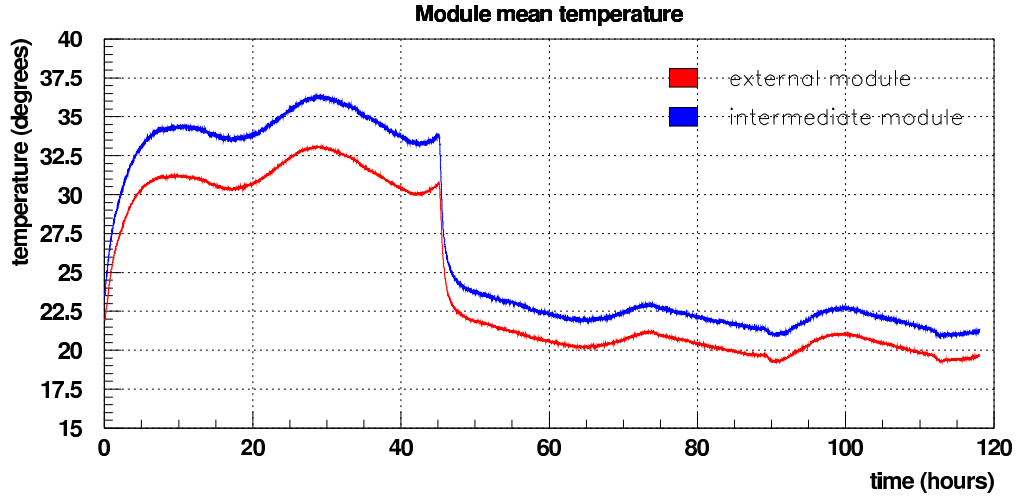
Figure 3.19: Front-end temperature measurements (ambient temperature around 24° C) in two modules mounted on a SuperModule. The step down took place at the same time the cooling was turned on (input water at 16° C).

construction of the SuperModule started only if all modules showed a leakage below 1 mbar/h. Gas tightness checks were repeated every time a new part of the gas-distribution system was mounted on the structure and ended with a global check of the SuperModule leak rate, when the full structure was assembled and ready for moving.

Pressure tests have been performed both on front-end electronics and readout-crate water-cooling systems. They were filled with a water pressure of about 10 bars, checking that no water was leaking from the pipe joints. Moreover, tests monitoring the temperature of the front-end electronics have been done to check its behaviour with water cooled by an external refrigerating system. This allowed to emulate realistic experimental conditions indicating that the system satisfies the ALICE requirements of staying below 25° C (Figure 3.19).

All cables have been tested before the installation. Special attention has been used measuring trigger-cable delays for trigger time-alignment purposes, while the Amphenol signal-cable lengths were known. It has to be remarked that during the SuperModule assembly all the used cables were labeled and traced in order to keep memory of the nominal delays introduced by them.
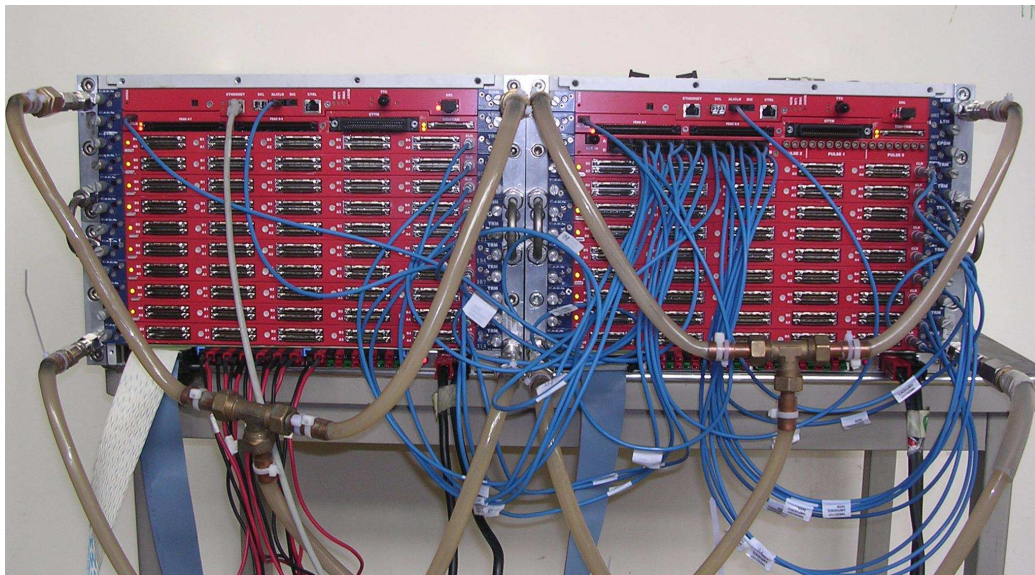
Figure 3.20: Two ALICE TOF custom crates under test in the crate test facility.

This helped a lot in calibration procedures. Front-end electronic cards have been tested and traced as well, and the same has been done for the low-voltage and threshold-voltage settings.

One of the most important quality checks is the validation of the custom crates and the readout electronics. They were performed before installing the crates on the structure. A dedicated facility has been set up for this purpose, as described in the following section. Lastly, once the SuperModule assembly is over, the final global checks apply, namely pulser, noise and data acquisition tests, discussed in Section 3.3.3.

3.3.2   Crate test facility

All readout crates have been deeply tested before installing them on the SuperModules. A dedicated test facility has been used to test a fully equipped crate pair.

The crate test facility includes all the services needed to safely power on and control crates and electronics. A refrigerator unit was used to provide the required cooling. The system allowed to quickly connect a new crate pair

thanks to special connectors. The water flow and temperature used were the ones foreseen for the experimental operation. Power supply was provided to the crates by a small version of the low-voltage system, using the same layout described in Section 2.5.1. To emulate the load of the front-end electronics passive resistors were connected in correspondence of the crate low-voltage output channels. To control the crates and the readout electronics, a LINUX PC was configured with the required applications.

The first check aimed to quickly verify the correct functioning of the crate. The power-on sequence was controlled, with special attention to low-voltage and current values which were compared with the expected ones. All channels were controlled, including both the unused ones and the programming voltage.

The readout electronics underwent a set of tests while installed in the crate. The DRM board interfaces the crate with the external systems, therefore all its functionalities must be perfectly working. They include, besides communication and control within the crate, also remote programming of the FPGAs which are hosted on each VME board. A scan of the VME bus was performed to detect accidental faults which would result in corrupted data transmission. The full check of the HPTDC features, for instance programming and readout, validates the TRMs inside the crate[15].

As a final check, before being accepted, all crates underwent a long-term test. The fully powered crate pair was burned in and stressed for at least one week (Figure 3.20).

3.3.3   Data acquisition test: pulser and noise

Data acquisition tests allow to fully check most of the functionalities of the SuperModule. The low-voltage system must be operative to power on and monitor both front-end and readout electronics. Water cooling is also mandatory to avoid damages.

The readout system was connected to the LINUX PC used in the crate test facility through the DRM SCL link for configuration and data collection. Data were collected from pulser and noise runs.

Pulser tests aim to check the full electronic chain of a TOF SuperModule: from the MRPC pickup pads to the HPTDC channels. A test signal is gen-

---

[15]All TRM boards have been tested in a separate test facility to check their functioning and measure their time resolution.
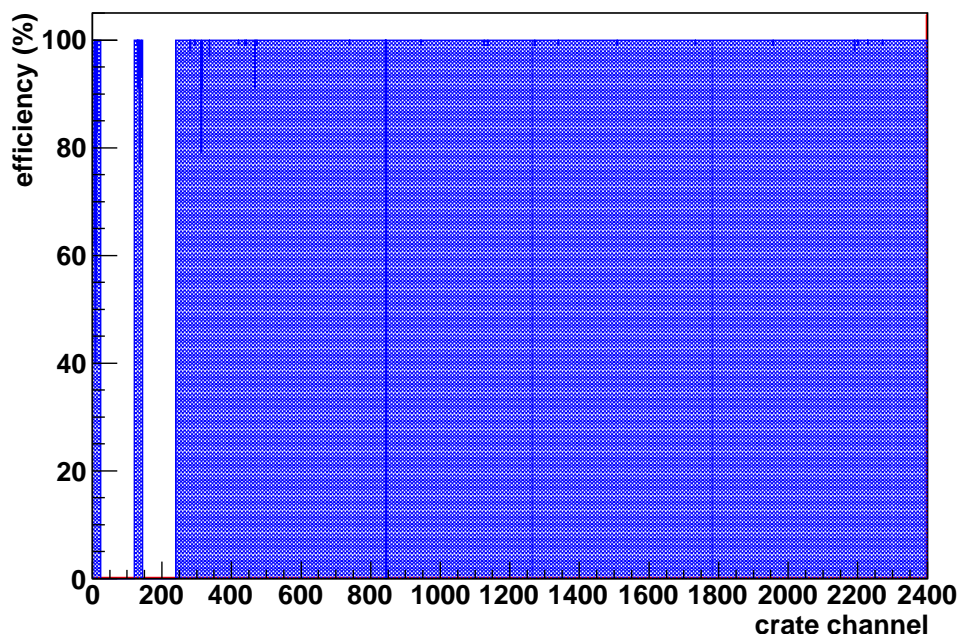
Figure 3.21: Pulser efficiency of the readout channels in a left-crate. Notice that only 48 over 240 channels of the first TRM (inserted in slot 3) are actually connected to a MRPC, as signaled by the large inefficiency gaps between channel 0 and 239. On the contrary, the inefficiency located in proximity of channel 825 is actually due to one dead channel.

erated by the CPDM, injected into the MRPC pulse lines and used as trigger for the readout system. The MRPC pads in turn reply with an induced signal recorded by the system. The presence of hits in correspondence to MRPC channels signals the correct functioning of front-end and readout electronics. Moreover, they reveal that the electrical connection is correctly done. In Figure 3.21 a typical result of a pulser test is shown. The efficiency of the readout channels in detecting the pulse-induced signal from the MRPCs is computed with respect to the number of test pulses.

Noise runs were performed to evaluate the electronic noise of a Super-Module. The front-end electronics was powered and thresholds were set up to the nominal value. No high voltage was applied to the MRPC detectors. The readout system was configured to scan a large time-window in order to
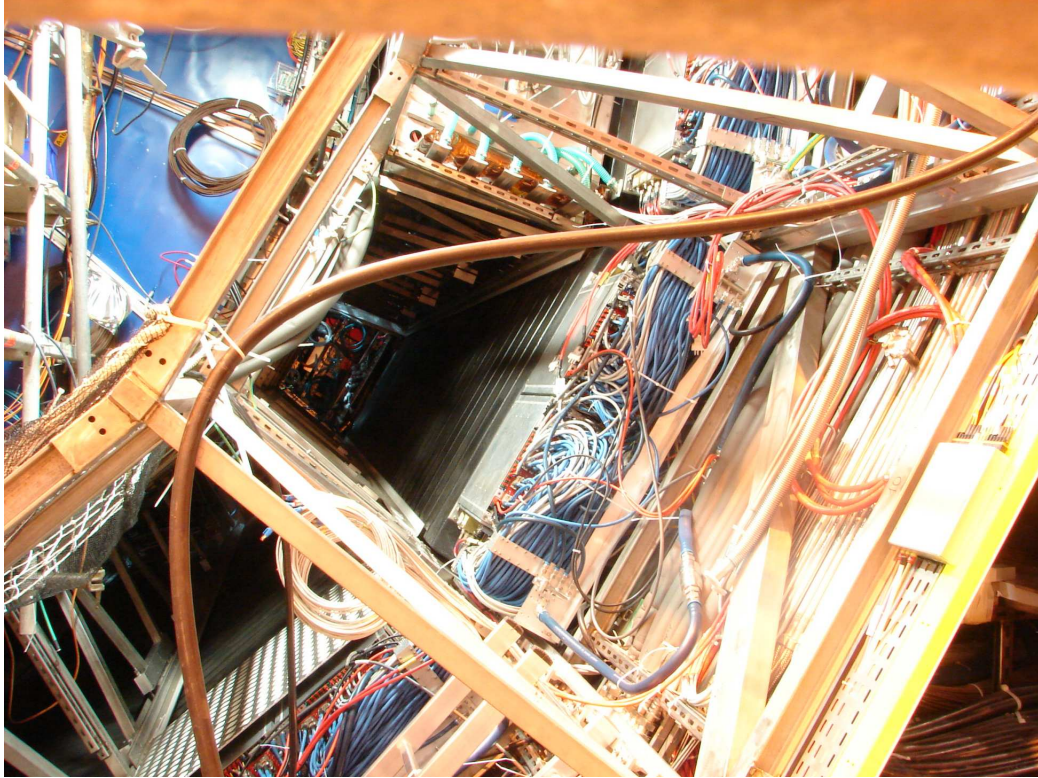
Figure 3.22: A TOF SuperModule installed inside the ALICE Space-frame.

reduce the number of events. An integrated time-window of 1 s was collected to obtain a noise sensitivity of the order of 1 Hz.

These tests, coupled with the online Data Quality Monitor (DQM) tools described in Section 3.4, allowed to quickly identify bad plugged-in electronic cards or cables. Moreover, they have demonstrated to be very useful also for detecting faults in the VME readout boards.

3.3.4   Installation

All 18 ALICE TOF SuperModules have been installed inside the ALICE Spaceframe (Figure 3.22). The installation, started in October 2006, finished in April 2008 and all services are currently connected.

3.4 Data Quality Monitor (DQM)

All the steps which led to the construction of the ALICE TOF detector were strictly followed by a set of quality assurance procedures, as widely underlined in this Chapter. Data readout of the detector is in most cases the last among the tests and provides more insight into the detector itself. While the detector is taking data, both during tests and physics runs, a check of the data quality is needed. For this purpose some monitoring tools have been developed. They have been used since the beginning of TOF commissioning and they have also been successfully used during the first global data-taking of ALICE.

3.4.1 The DQM tools: MOOD and AMORE

The online data quality monitoring is an important part of the ALICE data acquisition (DAQ) software framework[16] [155]. DQM allows to quickly detect faulty conditions or bad detector configurations during data-taking. Moreover, it is also necessary in order to have a quick look at the detector behaviour during detector commissioning.

For these purposes two online monitoring applications have been developed: MOOD (Monitor Of Online Data) and AMORE (Automatic MOnitoRing Environment) [156, 157]. MOOD has been designed to be an interactive application mostly devoted to detector debugging by detector experts. On the contrary, AMORE's design has been chosen to be automatic in order to easily notify the shift crew when something goes wrong. Figure 3.23 and 3.24 show a screenshot of MOOD- and AMORE-TOF modules, respectively.

Both AMORE and MOOD are written in C++ and they are based on the ROOT framework [158] which provides the Graphical User Interface (GUI) and the analysis tools such as histograms and graphs. The use of the DATE monitoring library provides the needed interface to the DAQ system and therefore to the raw-data stream.

Since MOOD and AMORE are applications with a modular structure in which classes containing detector-specific functionalities are loaded at run-time, specialized "modules" have been developed in order to monitor the TOF raw data stream produced in a wide set of test environments [159, 160].

---

[16]DATE (Data Acquisition and Test Environment), the data acquisition package used in ALICE, allows for online data quality monitor through dedicated routines.
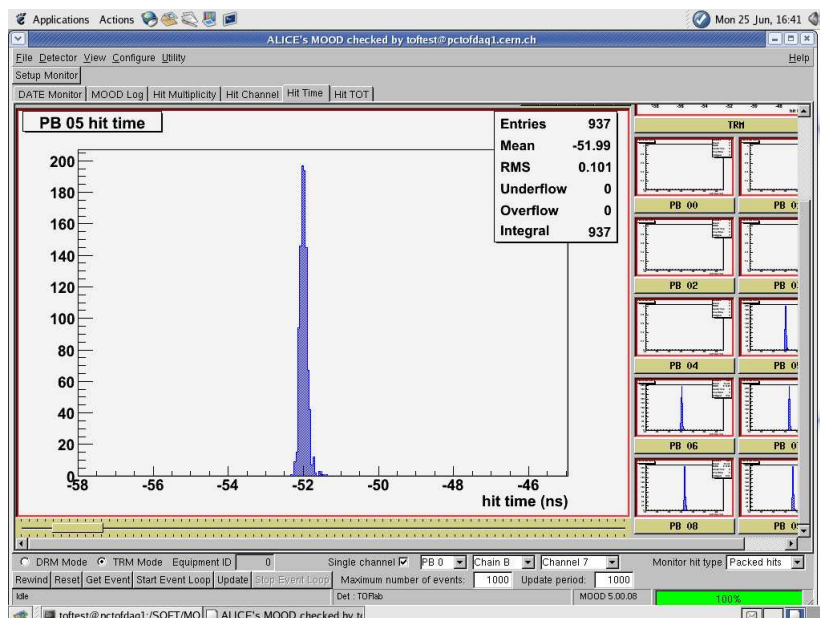
Figure 3.23: Screenshot of the MOOD-TOF module used during November 2006 test beam at CERN PS. The main histogram shows the online time distribution of a channel under test. The r.m.s. allows for a prompt evaluation of the time resolution.

All TOF modules share a fast and error-safe[17] decoder and a light interactive GUI to present in a set of online histograms the detector status.

The ALICE TOF data quality monitor was included among the quality assurance procedures a few years ago, when the module cosmic-ray test facility (Section 3.2.2) was starting taking data. All the relevant quantities needed to check detector and electronics status have been identified in order to make the monitoring tools fully satisfying the requirements. In the following section some of the features provided are presented.

3.4.2 Monitoring TOF data

---

[17]The ALICE TOF decoding routines have been developed in order to detect data inconsistencies. This functionality prevents unpredictable decoder behaviour due to wrong or corrupted data.
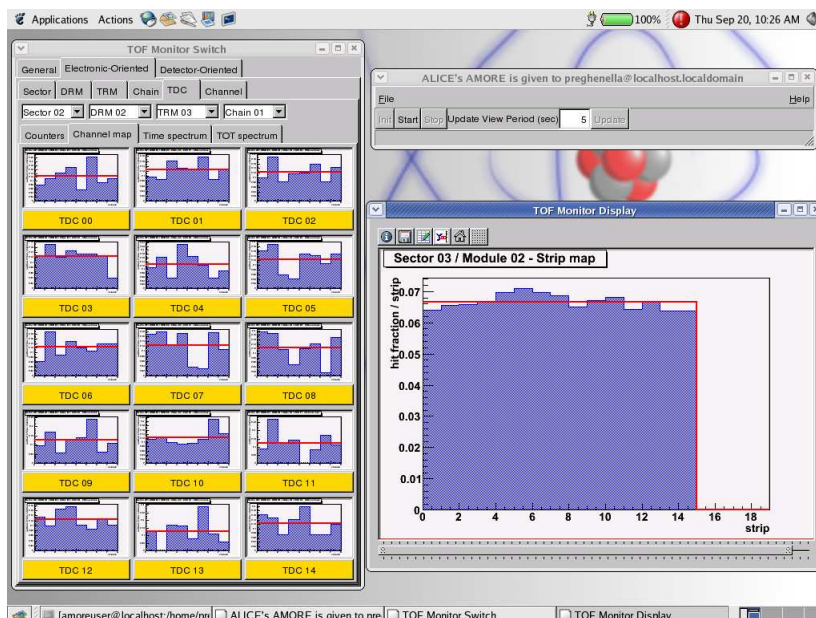
Figure 3.24: Screenshot of the AMORE-TOF module. The left frame acts as a histogram selector to display histograms in the display frame (bottom-right frame). The small window in the top-right corner is the AMORE framework control frame.

Test beam

During the November 2006 test beam on production MRPCs at CERN PS (Section 3.1.3) the data-taking has been continuously monitored. A dedicated MOOD module has been developed to deal with the specific experimental setup, focusing only on the relevant parameters. First of all, it showed to be very helpful in finding the beam position with respect to the MRPC readout pads. It also allowed to promptly evaluate the time resolution of the channel under test by looking at the root mean square of the online time distribution (Figure 3.23). In addition, it has been set up to compute the time resolution of the reference scintillator system.

Cosmic-ray test facility

The online monitoring of the data produced by the module cosmic-ray test facility (Section 3.2.2) was a key issue. A MOOD-TOF module has been
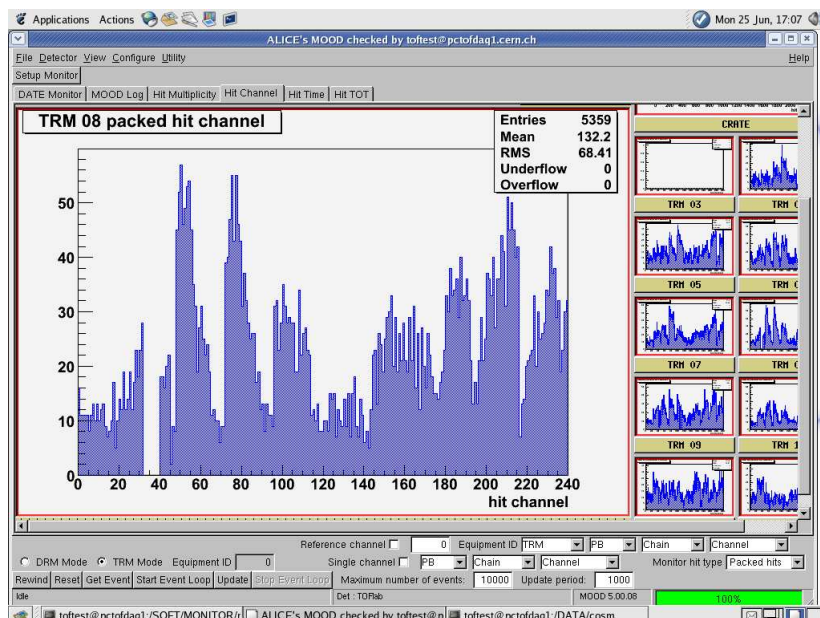
Figure 3.25: Screenshot of MOOD-TOF module while monitoring the module cosmic-ray test facility. The hole in the channel distribution (8 consecutive inefficient channels) signals a faulty TDC chip.

used and it has been continuously monitoring the data-taking since the first cosmic-ray run. MOOD has demonstrated to be able to detect bad configurations of the readout electronics (user-related) as well as faulty conditions (electronics-related), as reported in Figure 3.25, 3.26 and 3.27. This allowed to understand and fix the problems and therefore to restore as soon as possible the data-taking to collect data with the highest quality. Moreover, the careful observation of the online histograms enabled to evaluate the functioning of a module while exposed to cosmic rays without the need of further analysis. Some dead and noisy channels have been discovered in this way and promptly fixed.

Tests on SuperModules

The data acquisition tests performed on TOF SuperModules after their assembly, already mentioned in Section 3.3.3, were also monitored by MOOD. As a matter of fact MOOD has shown its capabilities signalling the presence
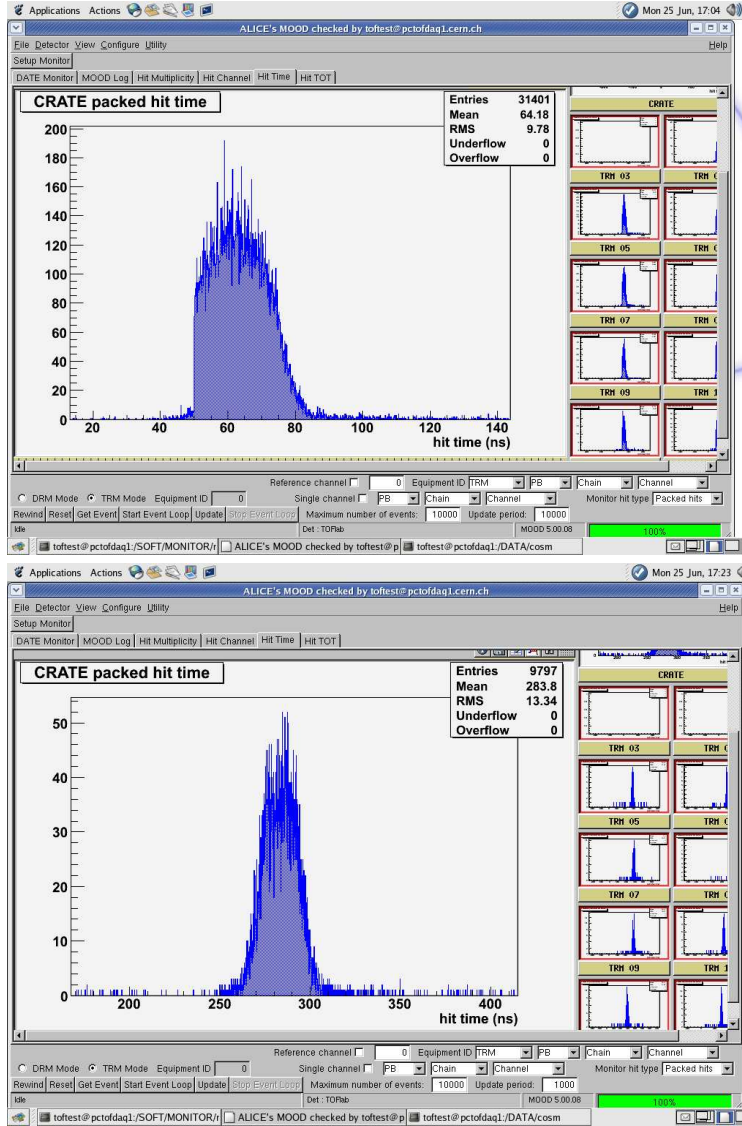
Figure 3.26: Screenshots of MOOD-TOF during cosmic-ray data-taking at CERN. The sharp cut in the time distribution (top) is due to a bad configuration (human-related) of the readout electronics (bad setup of HPTDC hit-selection window) which causes efficiency loss. The correct settings restore the quality of the data (bottom).
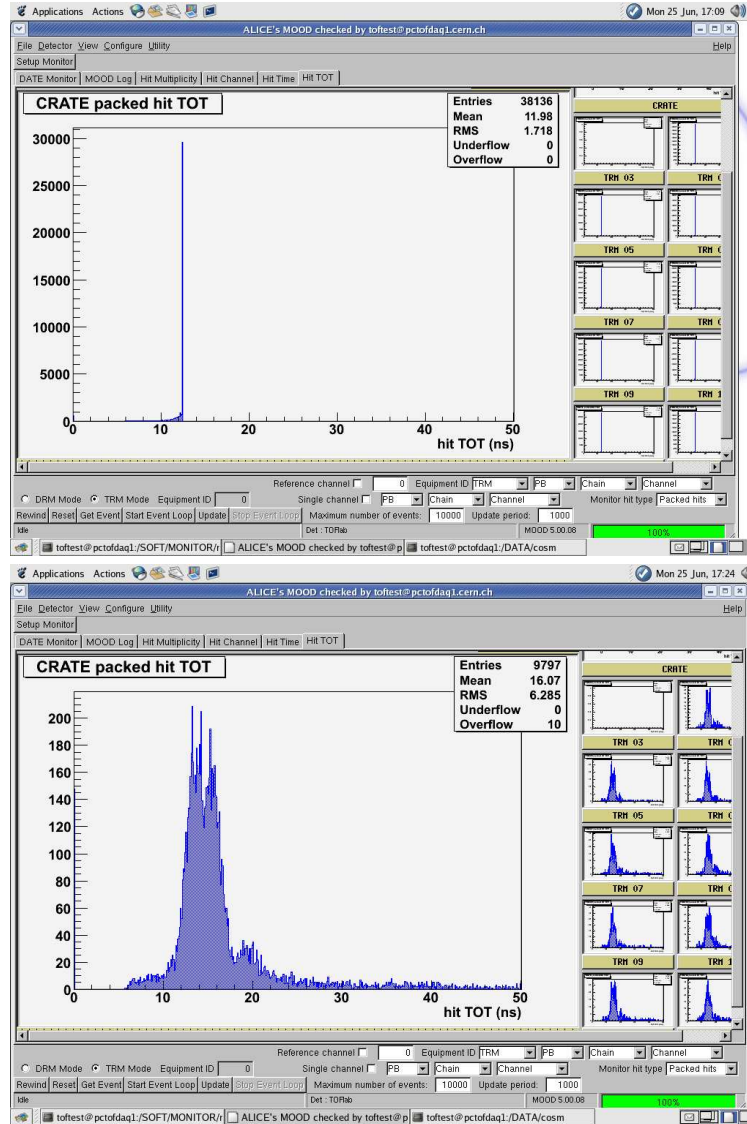
Figure 3.27: Another example of bad configuration of the readout electronics of the cosmic-ray test facility (top). The Time-Over-Threshold (TOT) spectrum is truncated around 12.5 ns with respect to the correct spectrum (bottom). This was due to a wrong setup of the TRM data compression.
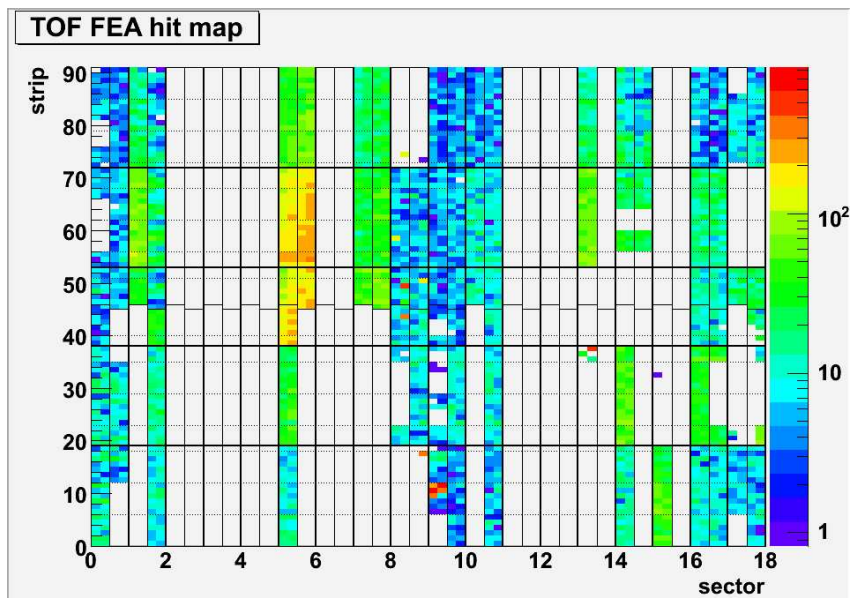
Figure 3.28: Online monitor histogram which shows the number of hits recorded by different parts of the TOF detector.

of bad plugged-in front-end cards or cables when need; it also helped locating the problems to fix them. Moreover, MOOD is equipped with a set of parameters which are dedicated to readout electronics monitoring. CRC[18] check and data consistency control, for instance, allow during readout to deeply probe the status of the electronics. Indeed, faults in the VME readout boards have been encountered, understood and fixed.

Commissioning with cosmic rays

The first ALICE global runs with cosmic rays took place in December 2007. Both AMORE and MOOD monitored the data produced by TOF and showed the first cosmic-muon signal recorded by TOF and triggered by ACORDE (Figure 4.2). With MOOD it was even possible to compute single-channel noise rates online by sending random triggers to the system (Figure 4.4). More features have been included both in AMORE and MOOD to fit with the requirements of an experiment-wide data-taking. Among them

---

[18]Cyclic Redundancy Check (CRC) is a generic method used to detect accidental alteration of data during transmission.

it is worth mentioning the trigger-selection capability, which selects only events recorded with a certain trigger condition, and the noise detection and filter to automatically detect and suppress noisy channels. A typical online histogram to monitor the data recorded by the TOF detector is shown in Figure 3.28. Notice that some parts of the TOF detector were not taking data in the reported example due to some low-voltage problems encountered during Summer 2008 and presently solved.

Whatever has been said about MOOD modules actually also applies to AMORE modules since everything but the automatic features is based on MOOD modules. The stronger use of MOOD with respect to AMORE for the time being is only due to the need of an interactive framework while commissioning and debugging the system.

Chapter 4

Commissioning with cosmic rays

4.1 First data-taking experience

During December 2007 the first global data-taking of ALICE with cosmic rays has been carried out. Two half-sectors of the TOF detector have been used to join the global runs: Sector-00 and Sector-08. Several TOF Super-Modules were already installed in ALICE at that time, but only the latter were available with all the needed services to correctly collect data.

The TOF geometrical configuration which characterized this commissioning phase, shown in a schematic drawing in Figure 4.1, was not optimal with respect to the used trigger configuration: the ACORDE single-muon trigger. The two sectors, according to the ALICE sector numbering as indicated in Figure 4.1, are located in such a way that only almost horizontal particles could cross both of them. Unfortunately, these events were not included in the ACORDE acceptance and were not triggered. Nonetheless, the sectors considered as independent detectors were sufficiently matched by the trigger acceptance to foresee that at least a few particles triggered by ACORDE could hit them.

Despite the non optimal geometrical configuration with respect to the ACORDE acceptance, the TOF has detected cosmic rays triggered by ACORDE. Moreover, a few particles which traversed one of the TOF sectors producing easily recognizable tracks have been reconstructed.

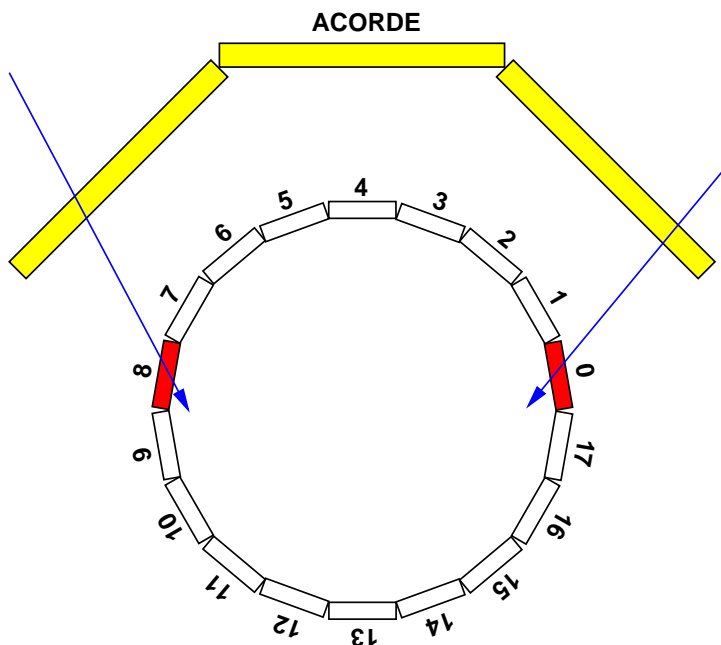As a further contribution to the first data-taking experience, noise mea-

Figure 4.1: Schematic drawing (not in scale) of the TOF geometrical configuration during December 2007 data-taking with cosmic rays.

surements were performed on the TOF detector, evaluating for the first time the background rate in the experimental environment. Noise measurements are actually an active part of detector commissioning and have been carried out continuously.

4.1.1 ACORDE single-muon trigger

Muons generated by primary cosmic rays in the atmosphere reach the ground level at the ALICE site. Before arriving in the underground cavern where the ALICE experiment is located, cosmic muons have to cross about 30 metres of rock. The typical rate for single atmospheric muons reaching the ALICE detector is relatively low, being about 4.5 Hz/m^2 on top of the magnet.

The ACORDE detector, a description of which can be found in Section 1.3.7, is located on top of the L3 magnet to enable cosmic-ray studies in ALICE. The ACORDE detector provides a fast Level-0 trigger signal to the
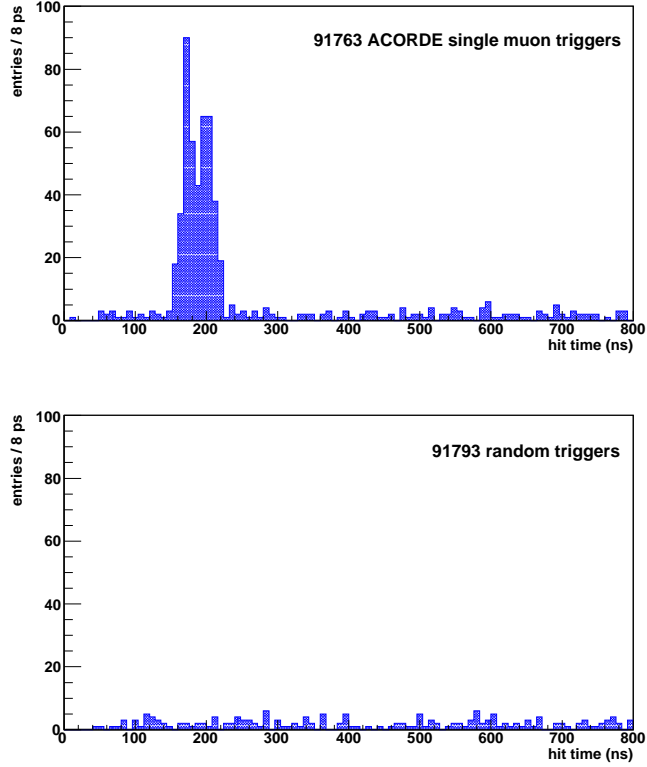
Figure 4.2: Hit time distribution measured during the first ALICE global cosmic run. A clear cosmic-muon signal is present when triggering the TOF detector with the ACORDE trigger while the signal disappears triggering randomly.

ALICE Central Trigger Processor (CTP) when atmospheric muons impinge upon the ALICE detector. This trigger signal was foreseen in ALICE for calibration and alignment procedures of the central detectors.

4.1.2 Evidence for cosmic-ray events

As already anticipated, during the first commissioning phase with cosmic rays, the Time-Of-Flight has detected muons triggered by ACORDE. Data correlated with the ACORDE trigger have been promptly seen on the online Data Quality Monitor (DQM) histograms, which provided the first evidence

for cosmic-muon detection by TOF inside the ALICE cavern.

Figure 4.2 shows how TOF has for the first time seen muons triggered by ACORDE: a clear peak is present in the hit-time distribution of the TOF detector when triggered with the ACORDE trigger, while the signal is not present when the detector is triggered randomly. Random triggers, also used for noise rate measurements as described in Section 4.1.4, allow to evaluate the detector background and confirm that the signal observed is actually related to the trigger configuration and not to the TOF detector itself.

4.1.3 Muon tracks within TOF sectors

The direct observation of cosmic-muon tracks would have strongly reinforced the results presented in the previous section.

Since only TOF Sector-00 and Sector-08 were recorded during the first commissioning phase with cosmic rays (December 2007), muons triggered by ACORDE could no be detected simultaneously by both sectors, thus preventing any study based on time-of-flight measurements. Moreover, the Time-Projection Chamber (TPC) was not participating in the global runs during that commissioning period and the matching of reconstructed tracks with TOF signals was not possible.

However a few particles had the correct angle to traverse several MRPCs of the same sector and the ultimate evidence that the TOF detector has seen cosmic rays triggered by the ACORDE single-muon trigger was the reconstruction of such tracks. An example is shown in Figure 4.3. The particle has passed across the sector width, traversing several MRPC strips. All the 17 MRPCs which have been hit by the particle have released a signal, therefore the detector efficiency must be high.

Despite several similar tracks have been found in ACORDE triggered data, they are quite rare events and not enough statistics has been collected to perform any quantitative study on TOF performance. Attempts to evaluate detector efficiency and resolution using such events pointed towards good performance of the detector, but no significant results have been obtained.

On the contrary, besides the further evidence for muon detection, this kind of events allowed to check the correspondence between readout channels and detector pads confirming the correct mapping implemented in the ALICE offline software framework (AliRoot). Moreover, the reconstructed tracks were often long enough to be shared among different modules and
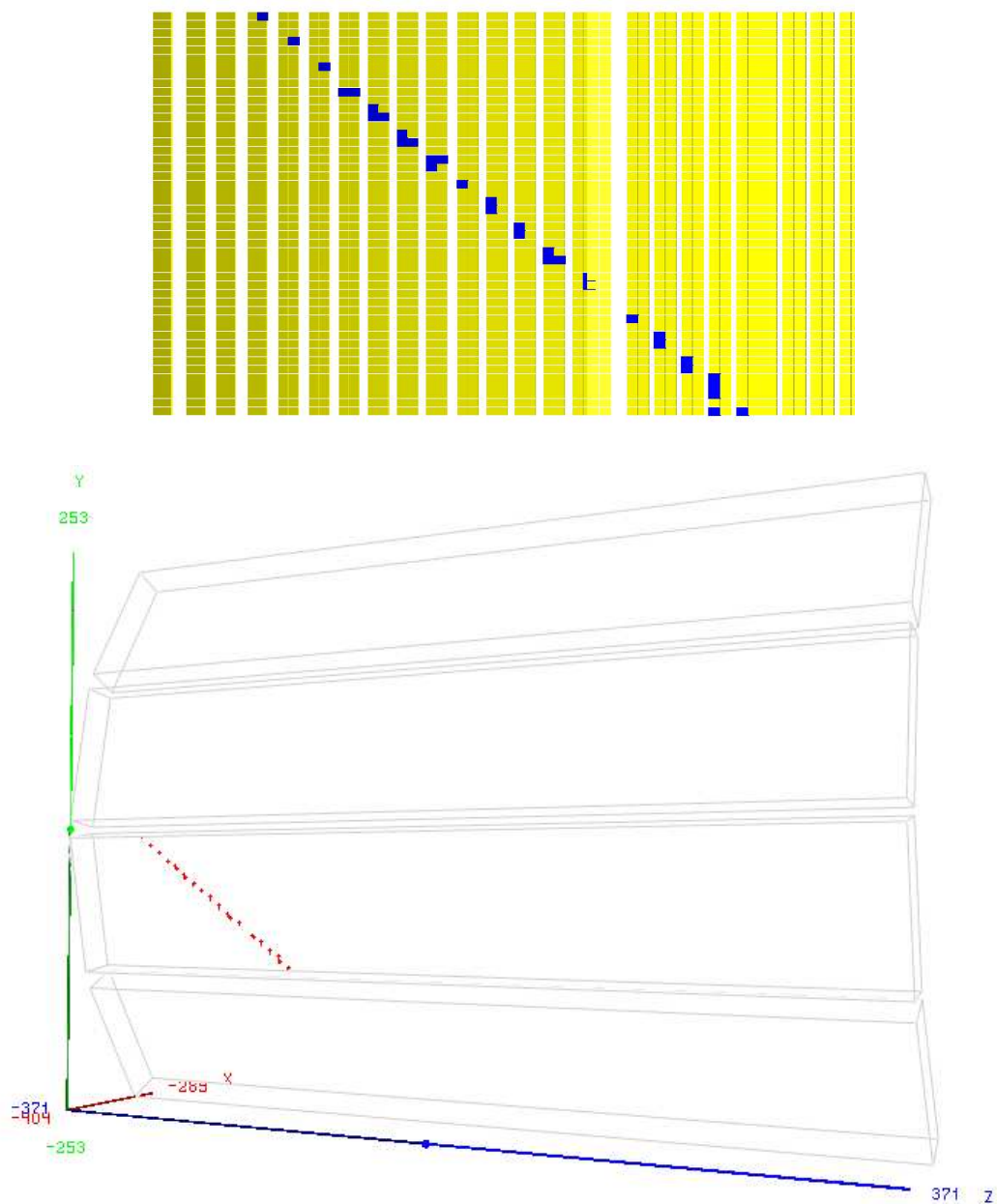
Figure 4.3: Event display of a cosmic muon traversing many strips in a TOF sector. The track passes across the sector width and hits, moving from left to right, first an external module then an intermediate one. Moreover, since the pickup pads along the length of a MRPC strip are shared among two crates, the track was recorded by different readout boards.
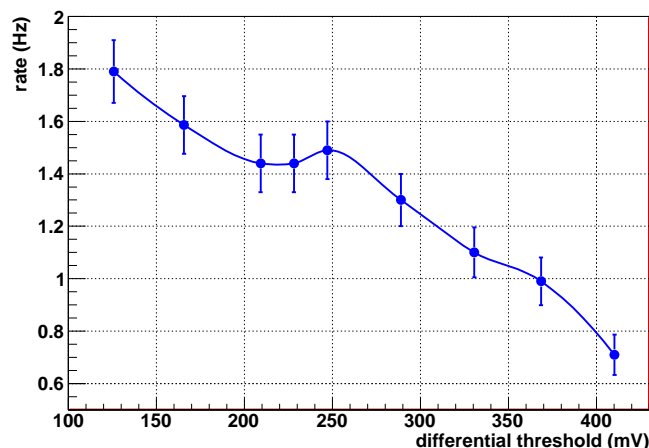
131

Figure 4.4: Single-channel noise rates as a function of the front-end discriminator circuit threshold. At a nominal threshold setting of 190 mV (November 2006 test beam) the noise rate is about 1.5 Hz.

crates, like in the example. This was the evidence that at least part of TOF readout electronics is well synchronized among itself, since each crate is an independent readout unit[1].

4.1.4   Noise rate measurements

Noise rate measurements on the TOF SuperModules installed in the experimental area have been done. In order to perform these measurements the detector was operated in STANDALONE mode, which is one of the running modes[2] defined in the ALICE ECS (Experiment Control System)[3]. The STANDALONE mode makes a detector detach from the global trigger and data acquisition systems to set up an independent data-taking unit[4]. All

---

[1]It has to be reminded that the Data Readout Module (DRM), present as master board in all crates, acts as the interface between TOF readout electronics and the ALICE central systems. This makes the crate the smallest readout unit of the TOF detector.

[2]The normal running mode for physics data-taking in ALICE is the GLOBAL mode.

[3]The Experiment Control System (ECS) provides a unified and central point from where all operations are initiated and controlled.

[4]Concerning the trigger side, the signal transmission to each detector is mediated by a Local Trigger Unit (LTU), as it has been already said in Section 1.3.8. The LTU can
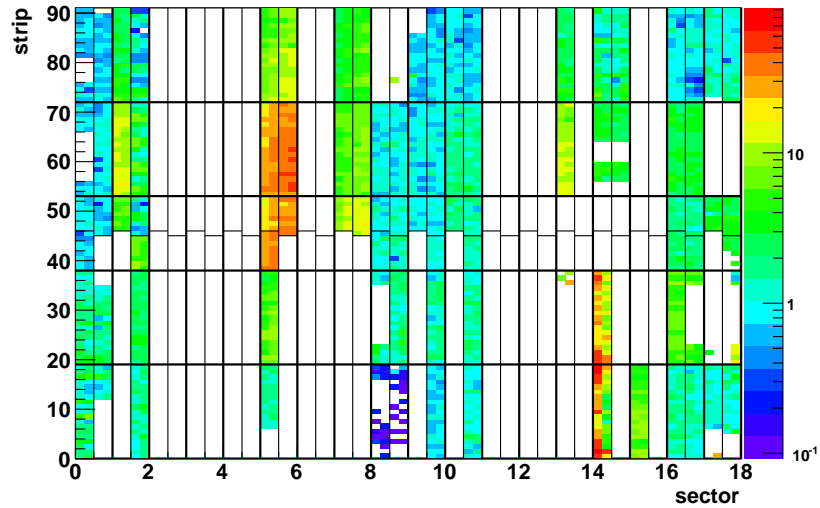
Figure 4.5: Noise-rate map recorded in September 2008. Not all the channels were active in the readout and some known problems were present. High rate in Sector-05 (strips 40-70) was due to low gas pressure, while in Sector-14 (strips 0-40) the thresholds were not correctly set. The low rate measured in Sector-08 (strips 0-19) was due to low high-voltage setup.
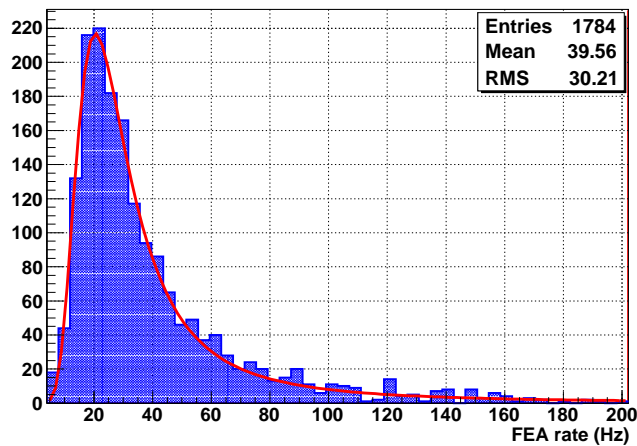

Figure 4.6: Front-End Analogue (FEA) card noise rate measured in September 2008. The mean FEA rate of about 40 Hz includes 24 channels and is in accordance with a single-channel noise of about 1.6 Hz. FEAs belonging to parts of the detector with known problems are not included.

the functionalities provided by the central systems (i.e. trigger generation and data recording) are guaranteed without interference with the other detectors. In fact, trigger type and rate can be set up in accordance to the detector needs as well as event building and data recording. Generally, the STANDALONE mode is used for debugging and test purposes.

Random triggers have been sent to the detector to drive the readout and data acquisition systems during noise runs. Since the generated triggers were not correlated with any physical event, the hits recorded within the HPTDC matching-window are only due to the detector noise and the environmental background (cosmic rays, natural radioactivity).

The single-channel noise rate r has been computed as

$$r = \frac{N_{hits}}{T_{integrated}},\qquad(4.1)$$

where N_{hits} is the single-channel number of hits recorded and $T_{integrated}$ is the integrated HPTDC time-window (T_{window}) over a given number of events (N_{events})

$$T_{integrated} = T_{window} N_{events}.\qquad(4.2)$$

A measurement of the single-channel noise rate has been performed varying the threshold of the front-end electronics discriminator circuit. As already pointed out, the LTM (Section 2.4.3) sets up the NINO ASIC differential threshold feeding the FEA with a programmable threshold voltage (Section 2.4.1). The results, which are based on data collected in the very first data-taking performed in December 2007, are presented in Figure 4.4. A mean single-channel noise rate of about 1.5 Hz was measured at the nominal threshold of 190 mV, which is better than the predicted value of about 5 Hz.

Further noise measurements have been performed at the fixed threshold of 190 mV including a larger number of readout channels. They are presented in Figure 4.5 and 4.6. Figure 4.5 shows a noise map based on data collected in September 2008. Some hot spots as well as cold spots could be identified in correspondence of known problems. Figure 4.6 shows the distribution of measured Front-End Analogue (FEA) card noise rates, when not in presence of known problems. The mean value (computed over more than 1700 cards, that is more than 40k channels) is about 40 Hz: this is the rate of 24 channels and is in accordance with a single-channel mean noise rate of about 1.6 Hz.

---

be decoupled from the CTP (Central Trigger Processor) for testing purposes and emulate trigger signals and sequences. This is what happens in STANDALONE mode.

4.2 TOF trigger commissioning

The ALICE TOF MRPC detector is a fast-response device, well suited for triggering purposes. The TOF trigger system, which has been already described in Section 2.4.3, contributes to the Level-0 and Level-1 trigger decision of the ALICE Central Trigger Processor (see also Section 1.3.8).

During the February–March 2008 commissioning period the TOF trigger system was fully operative. More SuperModules were provided with the needed services and could participate in the ALICE global data-taking. In particular, 8 sectors, corresponding to Sector-00, Sector-01, Sector-07, Sector-08, Sector-09, Sector-10, Sector-16 and Sector-17 where used to setup a coincidence in order to provide a muon trigger based on the TOF detector.

In the following sections a brief report on the first experience with the TOF trigger system is presented.
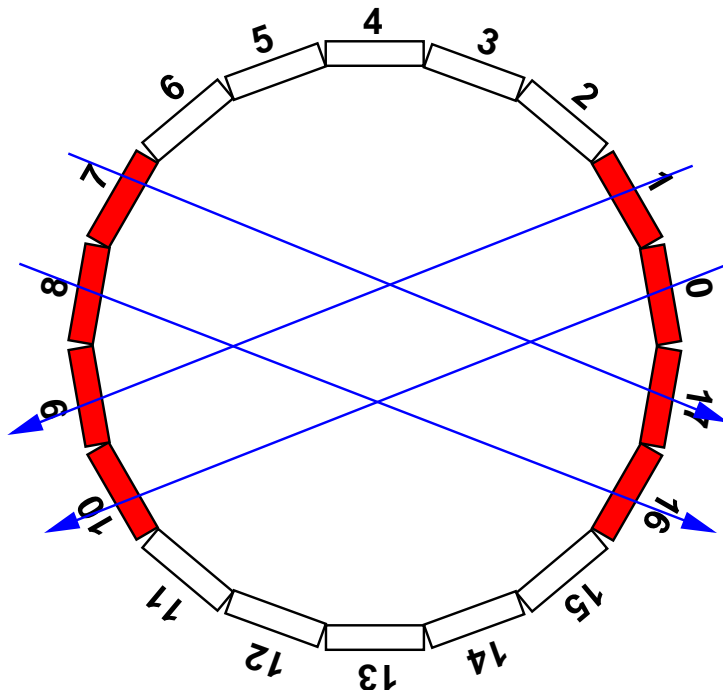
4.2.1 Standalone TOF trigger

The TOF cosmic-muon trigger described in this section was widely used during ALICE commissioning with cosmic rays. It is often referred to as the "TOF diagonal" muon trigger, because of the selection criteria used. Other trigger logics have been implemented for cosmic rays and used by other detectors for cosmic-ray data-taking. The diagonal trigger configuration was used for collecting the cosmic-ray data used for the studies presented in Sections 4.3 and 4.4.

The "TOF diagonal" trigger was set up to select cosmic muons traversing the ALICE central detectors following a diagonal trajectory. The following sector coincidences contributed to the trigger, as shown in Figure 4.7:

- Sector-00 and Sector-10;

- Sector-01 and Sector-09;

- Sector-07 and Sector-17;

- Sector-08 and Sector-16.

To evaluate the correct functioning of both the trigger logic and the read-out system, a first analysis has been done. A rough event selection on the data was performed using only the information coming from the TOF detector.
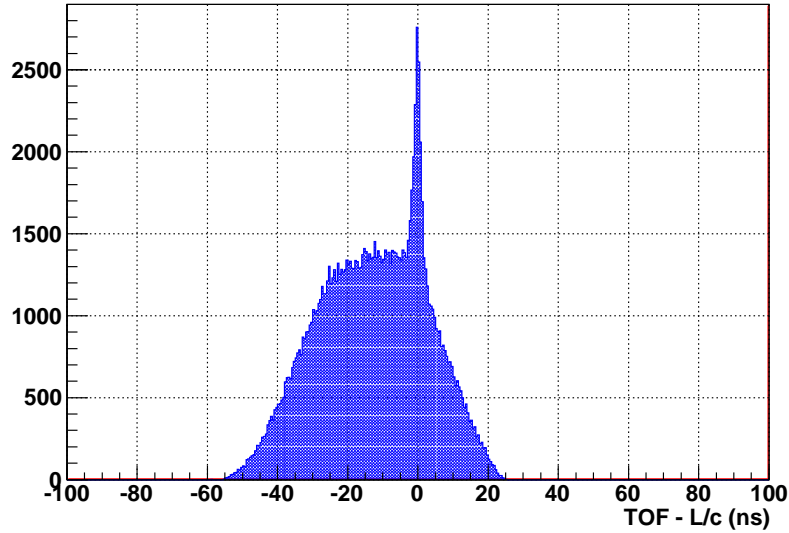
Figure 4.7: Schematic drawing of the TOF muon trigger configuration during February–March 2008 data-taking with cosmic rays.

The selected events must satisfy only one of the defined trigger conditions (e.g. "Sector-00 and Sector-10") with the further constraint that the event must contain only one hit per sector. This ensures that the selected events contain only two hits: the ones which have generated the trigger coincidence. At this point the analysis of the data is quite straightforward: the two hits are used to compute the time-of-flight between the two trigger sectors

$$TOF = t - t_{reference}, \tag{4.3}$$

where t and $t_{reference}$ are the time of the hits. Clearly, the choice of the reference time $t_{reference}$ has to be made in accordance with the physical content of the data. As an example, in case of the "Sector-00 and Sector-10" coincidence, the reference time must be provided by Sector-00: muon coming from the atmosphere cross Sector-00 before Sector-10.

The time-of-flight depends on the muon trajectory length, that is the distance between the TOF pads which have given the signal. Another quantity

Figure 4.8: Measured time-of-flight with respect to the expected value in events triggered by the TOF. The peak at zero signals that muons have been triggered.

was introduced to take into account the different trajectory lengths and put all the collected muon events on the same ground. This takes into account the expected time-of-flight, assuming that all selected muons travel at the speed-of-light

$$TOF - \frac{L}{c},\qquad(4.4)$$

where L is the distance between the TOF pads which have given the signal and c is the speed of light.

In Figure 4.8 the distribution of the measured time-of-flight with respect to the expected value L/c obtained from a rough analysis on TOF triggered data is presented. Cosmic muons crossing two different sectors have been triggered by the TOF detector and are represented by the clear peak at zero in the distribution. The measured time-of-flight is in accordance with the expected value and it is another clear evidence that the TOF readout electronics is correctly working and ready for physics data-taking.

The TOF detector is not a tracking device, therefore a trigger based only on TOF detector information cannot select muon events without introduc-
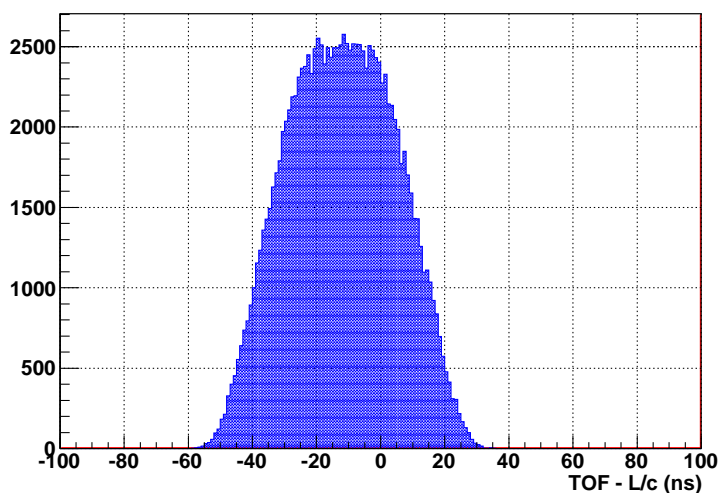
Figure 4.9: Simulation of the TOF trigger-coincidence logic. The shape reproduced the observed distribution of background events.

ing some background, as it can be noticed when looking at the distribution outside the muon signal. In fact, it is not possible to tell whether two TOF signals in coincidence have been actually generated by the same particle unless computing the time-of-flight and comparing it with the expected value. Unfortunately, this is not possible at the trigger level, since the only selection can be made on the basis of poor timing requirements to flag the coincidence as a valid trigger signature. The shape of the distribution outside the muon signal is related to the time window for the coincidence. A simplified simulation of the trigger logic reproduces the shape of the distribution of background events, as shown in Figure 4.9.

When looking at the distribution in Figure 4.8 it seems evident that the background rate is by far larger than the muon rate with this TOF trigger configuration. It has to be kept in mind, nonetheless, that the configuration aimed to select cosmic muons with large zenithal angles and that the flux of muons at large angles is low: the probability of having a good coincidence due to a very inclined muon (large angle) crossing both sectors is suppressed with respect to the probability of random coincidences due to two almost vertical muons. A quantitative evaluation of the expected ratio of good coincidences and random coincidences was not yet been made so far.
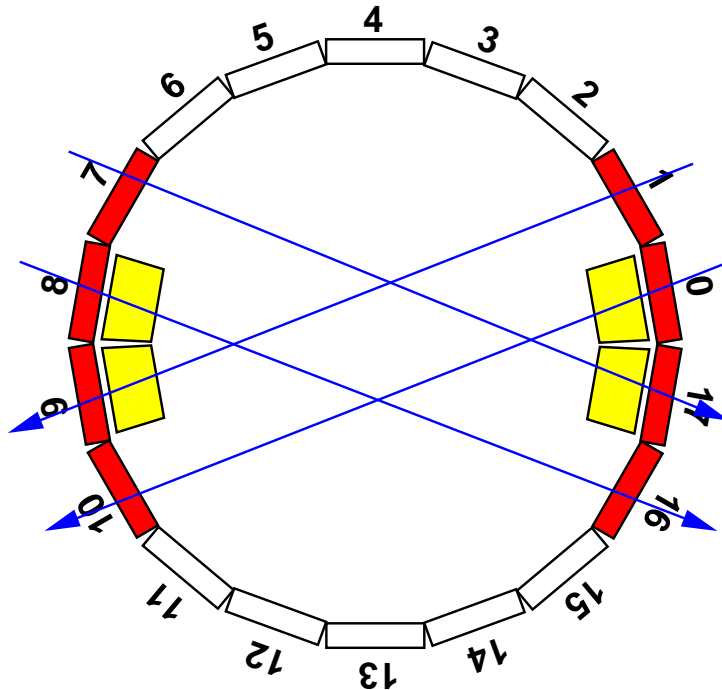
Figure 4.10: Schematic drawing of the TOF–TRD muon trigger configuration during February–March 2008 data-taking with cosmic rays. The TOF detector provides the Level-0 trigger while the TRD detector performs a higher-level event selection providing the Level-1 trigger.

4.2.2 TOF–TRD trigger sequence

The ALICE fast-logic trigger inputs are divided into two different levels: Level-0 and Level-1. Trigger signals from TOF are fast enough to contribute to the Level-0 trigger, while TRD signals are not. TRD signals may only contribute to the Level-1 trigger.

In ALICE a valid trigger condition requires a well-defined trigger sequence: a Level-1 trigger can be asserted only if a Level-0 trigger has been already sent. During the commissioning phase an improved trigger selection has been tested and achieved using the TOF triggers in combination with the trigger of the TRD detector. TOF trigger signals were used to provide the Level-0 selection while the TRD trigger performed a further selection asserting the Level-1 signal.

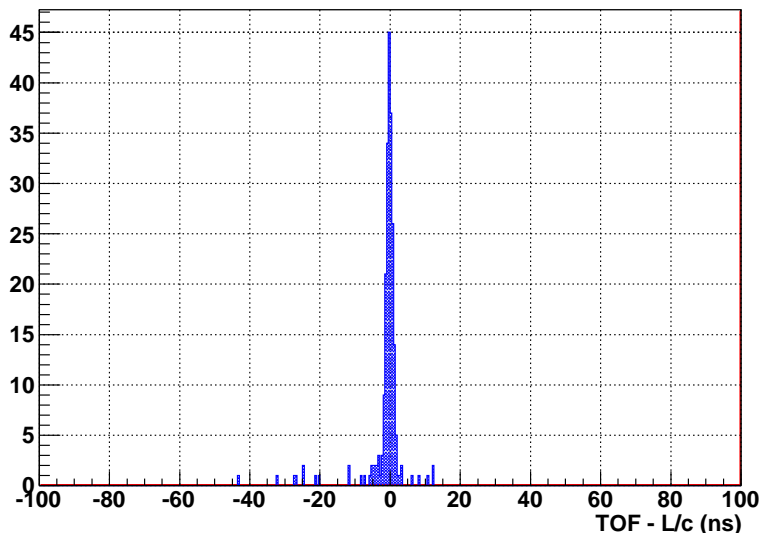The TOF trigger has been already discussed in the previous section. The

Figure 4.11: Measured time-of-flight with respect to the expected value in events triggered by the TOF–TRD L0–L1 trigger sequence. When combining TOF and TRD the background is strongly suppressed.

TRD detector has good tracking capabilities which enable to select among TOF triggered events only the ones in which a cosmic muon has actually crossed the TRD detector: this was indeed the aim of the TRD trigger. As a matter of fact, when combining TOF and TRD to provide a cosmic-muon trigger, the background events disappear almost completely, as shown in Figure 4.11: from the same rough analysis described in the previous section it clearly appears that the background rate is strongly suppressed.

4.3 Calibration with cosmic rays

The calibration of the ALICE TOF detector has been performed in a preliminarily way using cosmic-muon events collected during the global commissioning runs with cosmic rays. The TOF detector was not completely active during the data-taking, therefore only parts of the detector have collected cosmic-ray data.

It has to be said that the ultimate TOF detector calibration aims to

derive a set of parameters which should characterize the whole detector on a single-channel basis. Clearly, to obtain this level of accuracy, a very large statistics is needed since the number of readout channels is big (more than 150000 channels). It has been foreseen that to reach the optimal calibration level, about 10 million proton–proton collision events are needed.

Since beam–beam data are not yet available, cosmic rays give the opportunity to perform a first calibration of the detector. However, only a small number of muon tracks (~ 10000) have been reconstructed for TOF calibration purposes, which is by far insufficient for a channel-to-channel calibration. As a consequence, a smaller set of parameters has been used, identifying specific features which are common to different parts of the detector. A set of parameters were already known so far, while other parameters have been measured through the calibration procedure. In this way, a preliminary, though satisfactory calibration of the detector has been obtained even with a small number of tracks.

4.3.1 Event selection and track reconstruction

The data used to perform the calibration of the TOF detector with cosmic rays were collected over a long period of data-taking. The runs were selected among the ones recorded during September–October 2008 (runs belonging to the so-called LHC08d period), ranging over more than 15 days. The following selection criteria have been applied to find interesting runs, requiring that:

- both TOF and TPC were participating in the runs;

- a cosmic muon trigger was used for data-taking[5];

- the L3 magnet current was zero, that is there was no magnetic field;

- the runs have lasted more than 30 minutes.

The requirement of having TPC data is related to the need of having a tracking detector for muon-track reconstruction. The requested minimum

---

[5]Some test runs with unphysical triggers have been taken during LHC08d period, therefore they have not to be considered.

run duration of 30 minutes is arbitrary, but it is a reasonable value to guarantee a good run quality. This assumption is based on the fact that a "bad" run would have been stopped after a few minutes of data-taking. No specific selection on the trigger has been applied. TOF triggers represent the largest fraction of selected events; TRD and SPD triggered events have been also used for this analysis and no distinction among different trigger signatures has been done.

Event selection and track reconstruction are based on simple requirements which only rely on TOF and TPC cluster information: no other detectors have been used. In the ALICE offline software framework, a cluster is defined to be the data structure which contains the relevant information needed for track reconstruction, decoded from the raw data. Clusters in general allow to retrieve the spatial information through the geometrical description of the detector and in particular to obtain detector-specific quantities (for instance, hit time and Time-Over-Threshold are TOF specific information available from clusters).

Two steps are done to obtain from the data muon events well suited for calibration: the selection of candidate tracks and the reconstruction of real muon tracks, as described in the following paragraphs. About 11000 muon tracks have been reconstructed and selected for calibration over a total of about 2 million of events collected in 137 hours (5.7 days) of actual data-taking. As it can be noticed, the selection efficiency is low, being mainly related to the trigger efficiency in selecting adequate events for TOF calibration purposes. Most of the events have been triggered by the TOF muon trigger which was configured to select almost horizontal muons, as already pointed out in Section 4.2. Moreover, since the aim of this reconstruction is to obtain the best muon tracks for calibration purposes, the applied quality cuts further reduce the number of reconstructed tracks.

Candidate track selection

The selection of candidate-muon tracks is based only on TOF information. TOF clusters are combined to form pairs of clusters which have to satisfy one of the coincidence requirements reported in Table 4.1[6].

---

[6]These requirements have been applied in order to limit the number of possible cluster combinations to the ones which would result in good candidate-muon tracks. Candidate tracks which do not cross the TPC volume cannot be reconstructed and therefore are not
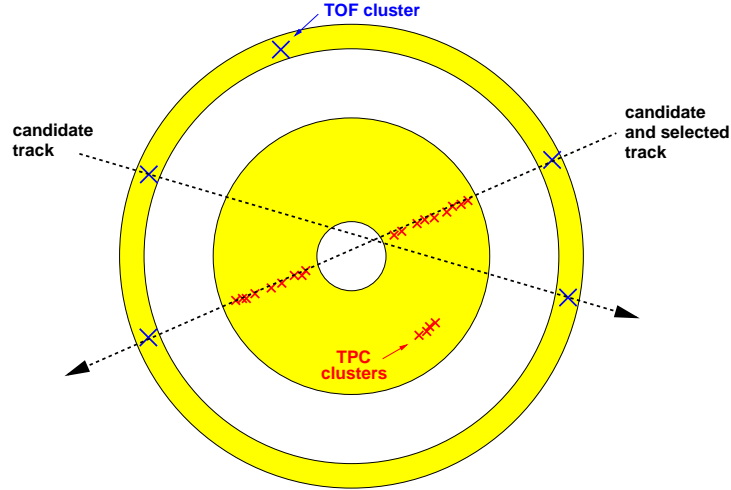
Figure 4.12: Schematic drawing of the muon reconstruction technique used for TOF calibration with cosmic rays. See text in Section 4.3.1 for more details.

Reference-sector clusters will be used to retrieve the reference time and the time-of-flight is computed between the reference and the other sector. No further constraints have been used to limit the maximum number of clusters in a sector in the same event. On the contrary, the limit of one cluster per strip was imposed in order to only select isolated clusters.

Selected cluster pairs define the candidate muon tracks (Figure 4.12) which are further processed in the track-reconstruction step.

Muon track reconstruction

The candidate muon track trajectory is defined using the spatial information of the TOF cluster pair to be the straight line connecting the two clusters in three dimensions (Figure 4.12). To evaluate whether a candidate track corresponds to an actual cosmic muon which has crossed the TOF detector, the information from the TPC is used, namely the spatial information of all the TPC clusters in the event.

The distance between the candidate track line and the TPC cluster point is computed in three dimensions for all TPC clusters. Clusters which are

---

considered.

Reference sector	Other sector
Sector-00	Sector-09
Sector-00	Sector-10
Sector-01	Sector-08
Sector-01	Sector-09
Sector-01	Sector-10
Sector-07	Sector-00
Sector-07	Sector-17
Sector-07	Sector-16
Sector-08	Sector-17
Sector-08	Sector-16

Table 4.1: Sector-coincidence requirements used for candidate-muon track selection.

correlated to the candidate track should lie close to its trajectory at about the same distance (Figure 4.12), while for non-correlated clusters the distances should be distributed almost randomly. Correlated clusters, which can then be associated to the candidate track, form a quite narrow-peak structure in the distance distribution (Figure 4.13) and are well separated from non-correlated ones even in a non perfectly aligned geometrical description. A cluster is associated to the candidate track if its distance to the track is less than 10 cm.

The requirements for a candidate track to be selected as a reconstructed muon track are the following:

- high number of associated TPC clusters (more than 100 clusters);

- narrow associated cluster distance distribution (less than 1 cm root mean square).

In Figure 4.14 the event display of a reconstructed muon track is shown.

4.3.2 Calibration approach

The calibration procedure is based on the time-of-flight of the reconstructed muons, as measured by the TOF detector. Let us call t_{ref} the time measured by one of the TOF clusters associated to the track (see Section 4.3.1), which is used as reference time, and t the time measured by the
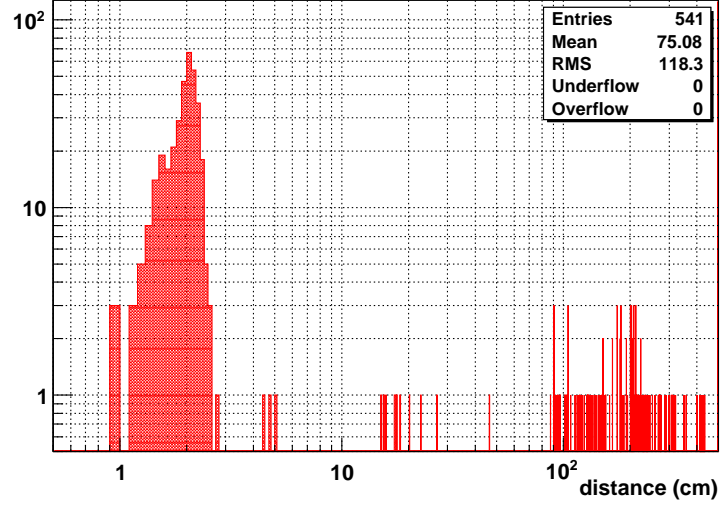
Figure 4.13: TPC cluster distance to candidate muon track for one candidate track. The distribution has a clear peak at small distances which signals that a high number of clusters are correlated to the candidate trajectory.

other cluster. The muon time-of-flight τ is measured via

$$\tau = t - t_{ref}. \tag{4.5}$$

The particle time-of-flight is related both to the particle speed and the trajectory length. Cosmic muons must be energetic enough to reach the ALICE detector underground[7], therefore we can safely conclude that they are relativistic particles traveling at the speed of light. The trajectory length L is computed as the distance in three dimensions between the associated TOF clusters. The expected time-of-flight τ_{exp} for a muon traveling at speed of light c over a trajectory of length L

$$\tau_{exp} = \frac{L}{c} \tag{4.6}$$

is used to define the deviation $\Delta\tau$ between measured and expected time-of-flight

$$\Delta\tau = \tau - \tau_{exp}, \tag{4.7}$$

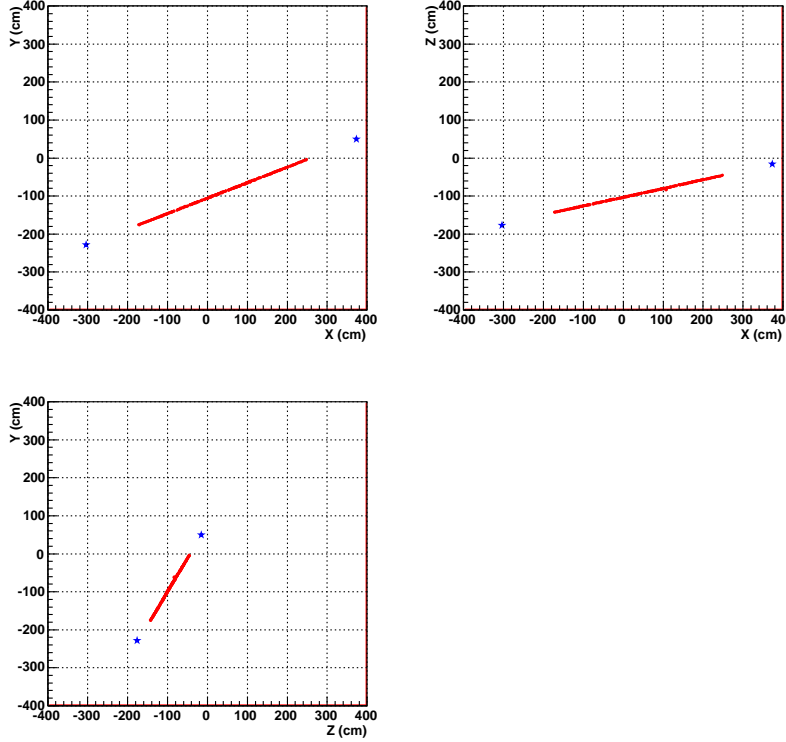[7]Atmospheric muons need an energy of at least 17 GeV to reach the ALICE hall.

Figure 4.14: Event display of a reconstructed muon track in three different views: front-view (top left), top-view (top right) and side-view (bottom left). Only the TOF clusters (blue) and the TPC clusters (red) associated to the track are shown.

which allows to put all muon tracks on the same level. On an ideally calibrated TOF detector $\Delta\tau$ must be, on average over all muon tracks, zero (provided that the muon speed is exactly c) and the width of the $\Delta\tau$ distribution must reflect the detector time-of-flight resolution.

Calibration parameters are then introduced to take into account any deviation of the time measured by the TOF detector with respect to the actual time. The details on the parameters used for the corrections are presented in Section 4.3.3 and 4.3.4. It is worth to anticipate that two different sets of parameters have been used: the so-called "nominal" and "unknown" calibration parameters. Both sets have been used to correct the data, but only the un-
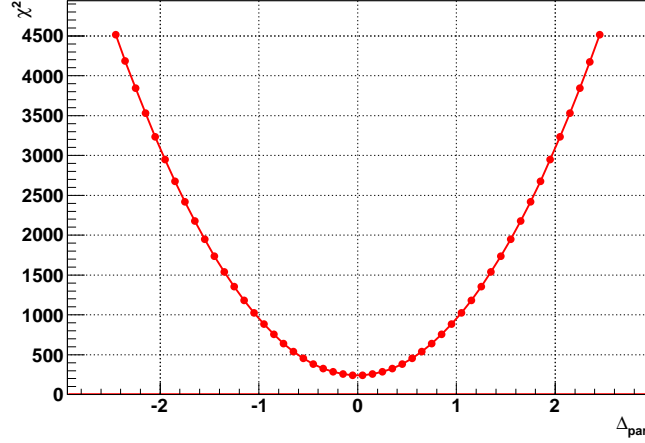
Figure 4.15: Example of the χ^2 values as a function of $\Delta_{par} = k - k_{min}$, where k is the value of one calibration parameter and k_{min} is the value of the parameter corresponding to the function minimum. The function has only one minimum corresponding to $\Delta_{par} = 0$.

known parameters have been determined through the calibration procedure, while nominal parameters, which are related to known detector hardware characteristics, have been kept fixed.

Let us introduce a generic correction function $F(\bar{r}, \bar{s})$ depending both on nominal and unknown parameters, being $\bar{r}$ and $\bar{s}$ respectively. The generic time t measured by the detector is then corrected via

$$\tilde{t} = t - F(\bar{r}, \bar{s}). \tag{4.8}$$

The corrected time $\tilde{t}$ is used to compute the corrected time-of-flight

$$\tilde{\tau} = \tilde{t} - \tilde{t}_{ref} \tag{4.9}$$

and the deviation of the latter with respect to the expected value

$$\widetilde{\Delta \tau} = \tilde{\tau} - \tau_{exp}. \tag{4.10}$$

The unknown calibration parameters $\bar{s}$ have been determined using a minimization approach. The function to be minimized has been defined as

$$\chi^2 = \sum_i \frac{(\widetilde{\Delta \tau_i})^2}{(\delta \tau)^2}, \tag{4.11}$$
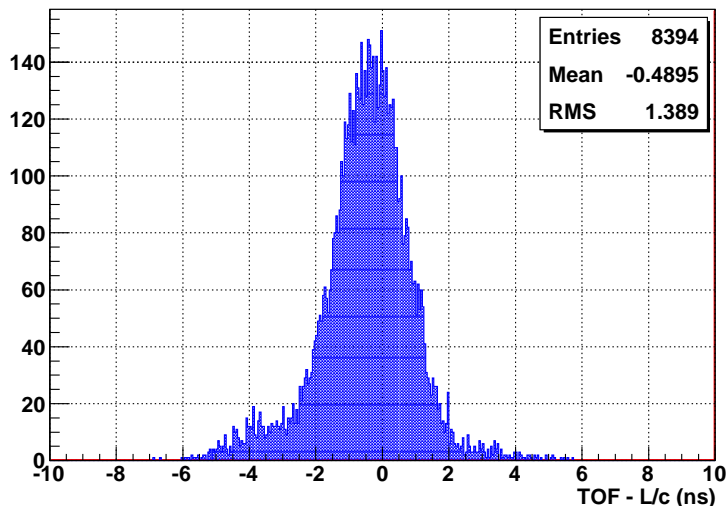
Figure 4.16: Deviation of the measured time-of-flight TOF with respect to the expected value L/c after applying the corrections obtained only from the nominal calibration parameters.

where $\delta\tau$ is the expected resolution for time-of-flight measurements and i runs over all muon tracks (Figure 4.15). A time-of-flight resolution of $\delta\tau = 113$ ps has been used for the calculations, considering a single-hit time resolution of $\delta t = 80$ ps[8]. The calculations to find the function minimum and to compute the value of the corresponding unknown calibration parameters have been performed using the MINUIT [161] minimization package.

4.3.3   Nominal calibration parameters

Some of the parameters which have been used to correct TOF data were already known from previous measurements and did not require to be determined: the "nominal" calibration parameters. Figure 4.16 shows the results obtained after correcting the data with only the nominal parameters.

---

[8]An overall time resolution of about 80 ps is expected for the ALICE TOF detector when taking into account all uncertainty contributions (i.e. detector intrinsic resolution, clock distribution, front-end and readout electronics).

Amphenol cable delay

The Amphenol signal cables connect the front-end electronics to the read-out electronics through 2-5 metres long cables (Section 2.4). They introduce a delay due to the propagation of the signals along the cables. The cable lengths were already measured before assembling the SuperModules and the position of the cables was traced in order to correctly associate to each read-out channel the corresponding cable length. The propagation speed over the cables was measured in laboratory to be (5.13 ± 0.03) ns/m and the delay $\Delta T_i^{Amphenol}$ introduced by the i-cable is subtracted to obtain the corrected time

$$\tilde{t} = t - \Delta T_i^{Amphenol}. \tag{4.12}$$

A check of the minimization approach of the calibration procedure (Section 4.3.2) has been done by using the Amphenol-cable propagation delay: it was allowed to vary as if it were an unknown parameter. The resulting value, corresponding to χ^2 minimum, was compatible with the measured propagation speed. This confirms that the minimization process used to obtain the calibration parameters is well under control.

Flat-cable and interface card delay

The flat-cables which bring the MRPC signals to the interface card inside the modules (see Section 2.3.2) introduce a delay which can be corrected. The flat-cable lengths range from 17 cm to 23 cm and have been traced during the assembly of TOF modules. No measurement of their propagation speed has been performed so far, therefore, as a first approximation, the nominal propagation speed of Amphenol cables can be used. In a more sophisticated approach the propagation speed can be set as an unknown parameter to be determined by the calibration procedure.

The module interface-card printed-circuit board (Section 2.3.2) joins with electrical connections the flat-cables and the front-end electronics. The length of the connection tracks on the board is known from its design and the propagation speed was calculated by means of a simulation of the board[9] to be about 6.9 ns/m.

---

[9]The calculations have been performed through a detailed simulation of the TOF module interface card using the HyperLynx (v7.7) simulator, being part of the Mentor Pads 2007 software for printed circuit board design.
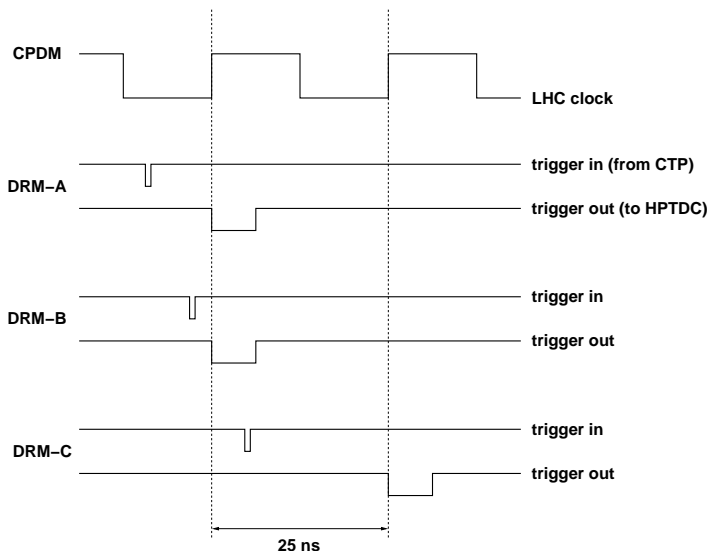
Figure 4.17: Scheme of the DRM trigger signal generation to TRMs and HPTDCs. Once the input trigger signal is received, the DRM generates an output trigger signal to the TRMs, synchronizing it with one edge of the LHC clock (here we suppose that a unique clock signal is used for all boards). In case of DRM-A and DRM-B the input signal is received within the same clock-cycle (bunch-crossing) therefore the output signal is generated simultaneously. DRM-C, on the contrary, receives the input trigger in the following clock-cycle, thus the output signal is synchronized with the following clock edge: it is generated 25 ns later.

Trigger fibre length

The trigger signal is brought to TOF crates through optical fibres. The length of the trigger fibres is not the same for all crates, therefore the trigger signal reaches different TOF crates in different times.

The trigger signal is received and elaborated by the DRM which in turn propagates it to the TRMs and to the HPTDCs. The propagation does not happen immediately after receiving the signal, but the output trigger is synchronized by the DRM with the LHC clock. For this reason, a sufficiently large length difference between two crates can make the two DRMs receive the trigger in two different clock-cycles and therefore make the two DRMs generate the output trigger to the HPTDCs in different clock-cycles (see Figure 4.17).
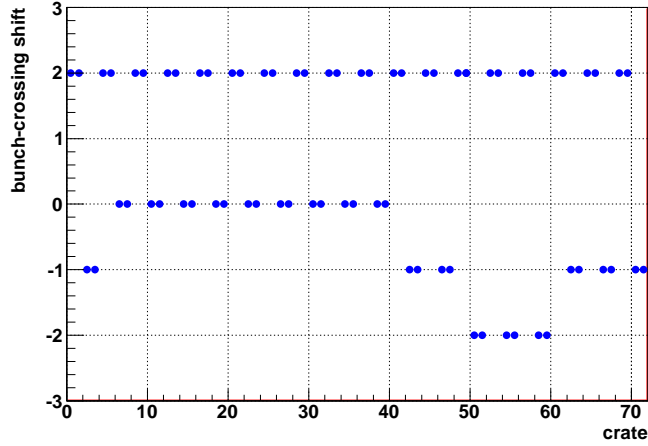
Figure 4.18: Measured crate clock-cycle differences (bunch-crossing shifts).

Let us suppose that two different DRMs, DRM-A and DRM-C, generate the output trigger to the HPTDCs, HPTDC-A and HPTDC-C, with one clock-cycle difference, that is DRM-C generates the signal about 25 ns after DRM-A[10]. HPTDC-C receives the trigger 25 ns after HPTDC-A, therefore it will start searching for matched hits opening the time-window 25 ns after HPTDC-A. Since the hit time is measured by the HPTDC with respect to the search-window edge, hits recorded by HPTDC-C are systematically displaced in time by 25 ns with respect to those of HPTDC-A, measuring 25 ns less.

This effect has been foreseen and measurements of the trigger cable lengths have been done in order to evaluate the differences in terms of clock-cycles (also called bunch-crossings) among different DRMs. The measured clock-cycle differences (bunch-crossing shifts) are reported in Figure 4.18. The values must be intended as relative clock-cycle differences with respect to an arbitrary reference.

The correction to TOF hits for this effect has been done as follows:

$$\tilde{t} = t + \Delta\nu_i \, T^{LHC}, \tag{4.13}$$

where $\Delta\nu_i$ is the measured clock-cycle difference for crate i, and T^{LHC} is the LHC clock period.

---

[10]The LHC clock period is about 25 ns.

It is worth mentioning that there are further plans to align all crates to eliminate the effect. This can be done by properly setting up the HPTDC latency window.

4.3.4 Unknown calibration parameters

As already pointed out, TOF calibration on a single-channel basis was not possible because of the lack of statistics. To overcome this problem, a small number of calibration parameters valid in general for all pads has been identified taking advantage of global features of the TOF detector. These parameters, which are called "unknown", have been calculated using the calibration approach described in Section 4.3.2.

Crate time-shift

One parameter has been assigned to each readout crate, as it is the smallest TOF readout unit. The value takes into account any further time-shift associated to the crate, which must be common to all boards installed in the crate. Relative time-shifts between different crates can be related to the LHC clock distribution: the clock is distributed to all CPDMs through optical fibres and the CPDMs in turn feed all the boards in the crates (Section 2.4.2). If fibres of different lengths are used to bring the clock to the CPDMs, they introduce a relative time-shift of the clock itself which results in different clock phases between different crates.

Let us suppose that two different CPDM boards, CPDM-A and CPDM-B, receive the LHC clock with a relative phase $\Delta\phi = 5$ ns, being CPDM-B behind CPDM-A, as presented in Figure 4.19. Both DRMs, DRM-A and DRM-B, associated with the crates receive the trigger at the same time. Before generating the output trigger towards the HPTDCs the DRMs synchronize it with the LHC clock, therefore DRM-A will generate the trigger before CPDM-B, since the clock edge of CPDM-B arrives 5 ns later. The HPTDCs receive the trigger in different times and this is propagated to the the data, as already pointed out in the case of the time-shift introduced by the trigger fibres in Section 4.3.3.

The time measured by one crate is corrected subtracting the measured time-shift
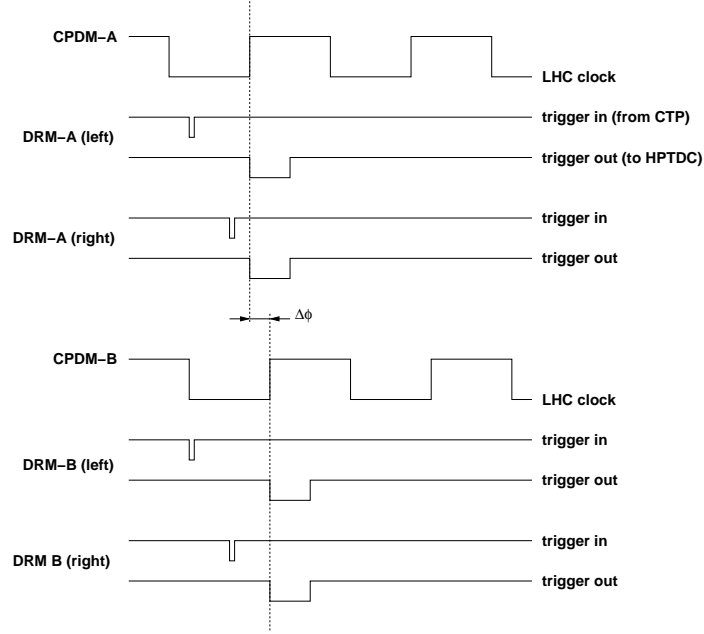
$$\tilde{t} = t - \Delta T_i^{crate}, \tag{4.14}$$

Figure 4.19: Scheme of the DRM trigger generation to TRMs and HPT-DCs. Two crate pairs A and B are equipped with one CPDM and two DRMs each. The clock phase between CPDM-A and CPDM-B is non-zero. Once the input trigger is received the DRM generates an output trigger to the HPTDCs synchronizing it with the clock. The clock seen by DRM-A and DRM-B is not the same therefore the output triggers are not generated at the same time even though the inputs have been received simultaneously.

where ΔT_i^{crate} is the time-shift associated to the crate i, and $i = 0, ..., 71$ is the crate index number of the hit to be corrected. Since not all crates were participating in the data-taking, not all 72 parameters could be determined. In Figure 4.20 the relative delays between different crates are presented. Since the clock distribution is mediated by the CPDM which serves a pair of crates, the time-shifts should be common for all crate pairs. This is, indeed, what is observed from the measured values: crate pairs share a common time-shift signalling that the effect is actually linked to the clock distribution. Nevertheless, despite only 36 parameters are enough to take into account this effect, the original solution with one parameter per crate was kept.
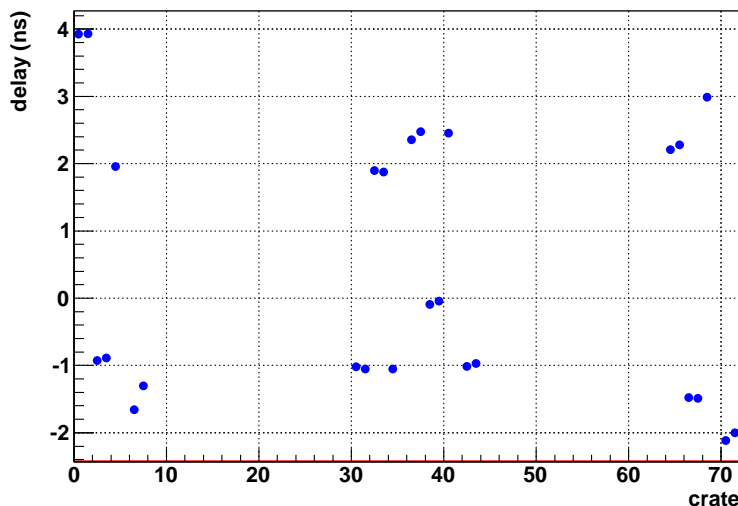
Figure 4.20: Crate delay parameters as measured with cosmic-ray calibration. Crate pairs (identified by consecutive crate indices, like 0-1, 2-3, ..., 70-71) share the same delay as they are fed by the same CPDM.

HPTDC time-shift

The TRM boards host 30 HPTDCs each, mounted on piggy-back cards in groups of three chips. Since all TRMs are equal, a set of parameters has been introduced to characterize their internal behaviour: 30 parameters are used to take into account any time-shift associated to the HPTDCs inside the board. They include time-shifts due to clock distribution to the HPTDCs as well as time-shifts due to the routing of the input signals; these contributions cannot be decoupled.

As a first approximation, since all piggy-backs are the same, 3 parameters should be enough to take into account the largest part of the delays. In fact, as can be deduced from the measured values presented in Figure 4.21, the time-shifts approximately repeat every three HPTDCs, signaling that most of the contribution is due to the piggy-back design. Nonetheless, a contribution due to the position of different piggy-backs inside the TRM is measured.

The correction to the measured time is applied as follows:
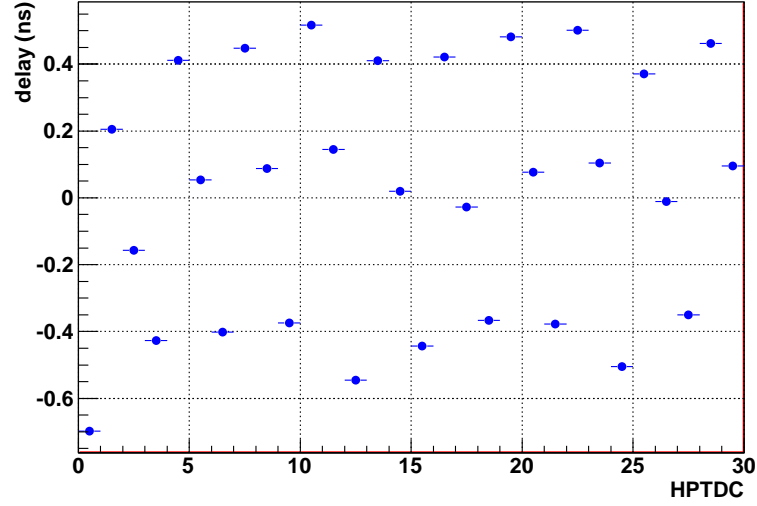
$$\tilde{t} = t - \Delta T_i^{HPTDC}, \tag{4.15}$$

Figure 4.21: HPTDC delay parameters as measured with cosmic-ray calibration. The delays must be intended as relative delays.

where ΔT_i^{HPTDC} is the time-shift associated to the HPTDC i, and $i = 0, ..., 29$ is the HPTDC index number. The same correction applies for all TRM boards.

FEA channel time-shift

The signals from the MRPCs are amplified and discriminated by the FEA cards before being readout by the TRM boards (Section 2.4.1). Two different kinds of FEA cards have been used for the TOF detectors: left- and right-FEA. Each card hosts 24 readout channels which are in turn connected to a TRM piggy-back. The signal routing within the FEA card introduces different delays between different channels; the same happens inside the TRM piggy-back. Since all FEAs (of the same type) and all piggy-backs are identical, $24 + 24$ calibration parameters have been used to characterize the delays introduced by the FEA–piggy-back systems in the two configurations (left and right).

If the channel to be corrected belongs to a left-FEA the correction is

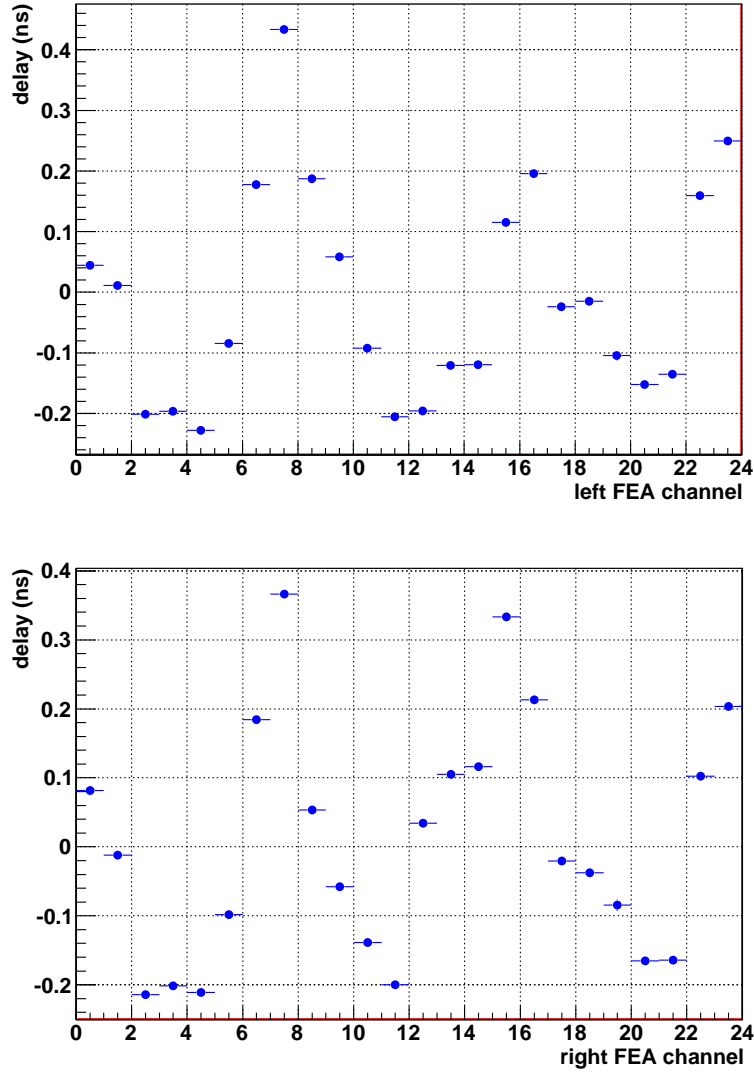$$\tilde{t} = t - \Delta T_i^{left-FEA}, \tag{4.16}$$

155

Figure 4.22: Left-FEA (top) and right-FEA (bottom) delay parameters as measured with cosmic-ray calibration. The delays must be intended as relative delays.

while if the channel belongs to a right-FEA

$$\tilde{t} = t - \Delta T_i^{right-FEA} \tag{4.17}$$

is used. $\Delta T_i^{left-FEA}$ and $\Delta T_i^{right-FEA}$ are the time-shifts associated to the left- and right-FEA channel i respectively.

The values of the measured parameters are shown in Figure 4.22.

Global time-slewing

The time-slewing correction has been applied to take into account time-amplitude correlations[11]. It has been already said that Time-Over-Threshold information is used for time-slewing correction on TOF data (Section 2.4.1).

The time-slewing correction is normally done on a single-channel basis, being the correction function strongly related to the behaviour of the channel itself and of the associated discriminator circuit. Clearly this cannot be done in our case (low statistics), thus a global time-slewing correction was performed applying the same correction function to all channels.

The correction to the measured time is applied as follows:

$$\tilde{t} = t - S(TOT), \tag{4.18}$$

where $S(TOT)$ is the time-slewing correction function

$$S(TOT) = C_0 + C_1 \, TOT + C_2 \, TOT^2 + C_3 \, TOT^3, \tag{4.19}$$

C_i are the calibration parameters, and TOT is the measured Time-Over-Threshold of the hit to be corrected.

It has to be pointed out that to obtain the global time-slewing correction function only Time-Over-Threshold values between 12 ns and 17 ns have been considered. The choice is motivated by the fact that Time-Over-Threshold spectra are not equal for the whole TOF detector, the biggest differences being located in the low and high TOT region; this requirement has to be intended as a prevention against possible incompatibilities which would result

---

[11]Time-amplitude correlations are related to the fact that the signals from the MRPCs enter a discriminator circuit with finite threshold before being digitized and recorded. Signals with large amplitude overcome the threshold before small-amplitude signals leading to a correlation which can be exploited to further correct the data.
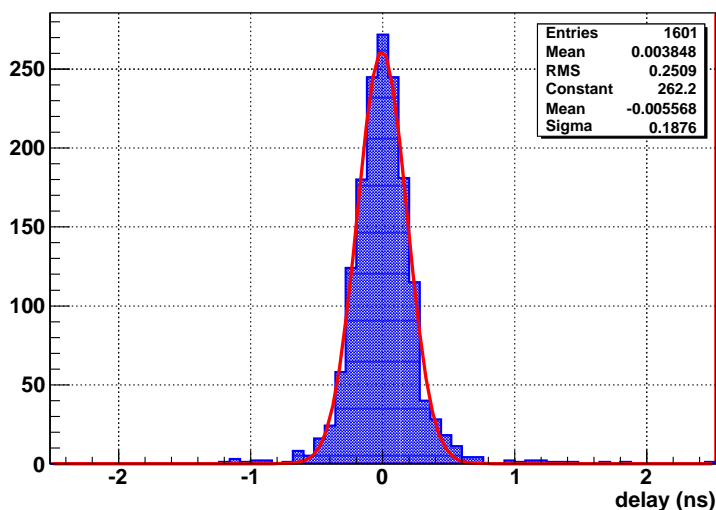
Figure 4.23: Distribution of the measured further Amphenol cable delays. One entry corresponds to the measured further delay of one cable

in a non reliable global time-slewing correction[12]. Moreover, despite the small range considered, the largest part of the signals lies in this region with about 75% of the selected muon tracks.

Further Amphenol cable delay

Despite the length of the Amphenol signal cables and their propagation delay were known, as already discussed in Section 4.3.3, one parameter has been introduced and associated to each cable. This parameter should take into account any further delay to be applied to the nominal cable delay.

A total of more than 6500 parameters is needed to characterize all signal cables, which is quite a big number with respect to the collected statistics. These parameters, therefore, can only be calculated with very limited accuracy. Moreover, since only a part of the detector has taken data, only some of them could be determined.

---

[12]Since in the normal calibration of the TOF detector the time-slewing correction is performed on a single-channel basis, no incompatibilities can arise and the full TOT range is used.

The correction to the measured time is applied as follows:

$$\tilde{t} = t - \Delta T_i^{cable}, \tag{4.20}$$

where ΔT_i^{cable} is the time-shift associated to the cable i, and i is the cable index number.

In Figure 4.23 the distribution of the measured values ΔT_i^{cable} is shown. The parameters ΔT_i^{cable} represent the further time-shifts associated to the Amphenol cables which were not included in the nominal values. The parameter distribution is thus related to the accuracy with which the nominal parameters, that is the Amphenol cable lengths, were known. The standard deviation of the distribution of the residual cable lengths, which can be obtained by taking into account the propagation speed over the cables, is measured to be about 4 cm; this also includes the uncertainties related to cable connectorization process.

4.3.5 Results and discussion

The calibration parameters obtained from the calibration procedure have been used to correct the TOF measurements; in Figure 4.24 the results are presented in terms of the deviation of the measured time-of-flight TOF with respect to the expected value L/c. The width of the distribution represents the time-of-flight resolution attained with the current calibration parameters: a resolution of about 190 ps is measured.

The detector resolution is evaluated taking into account that time-of-flight measurements are done via two independent time measurements provided by the TOF detector itself, thus if $\delta\tau$ is the time-of-flight resolution, the single-hit time resolution δt is

$$\delta t = \frac{\delta\tau}{\sqrt{2}}. \tag{4.21}$$

A time-of-flight resolution of about $\delta\tau = 190$ ps leads to a single-hit time resolution of about $\delta t = 130$ ps. In Figure 4.25 the zones of TOF detector (corresponding to the FEA cards) which have been hit by a reconstructed muon track are presented.

It has been already pointed out that with cosmic muons an optimal calibration of the detector is not possible for the time being because of the lack of statistics. Therefore, the measured resolution has to be intended as the upper limit of the actual TOF detector time resolution, which can be
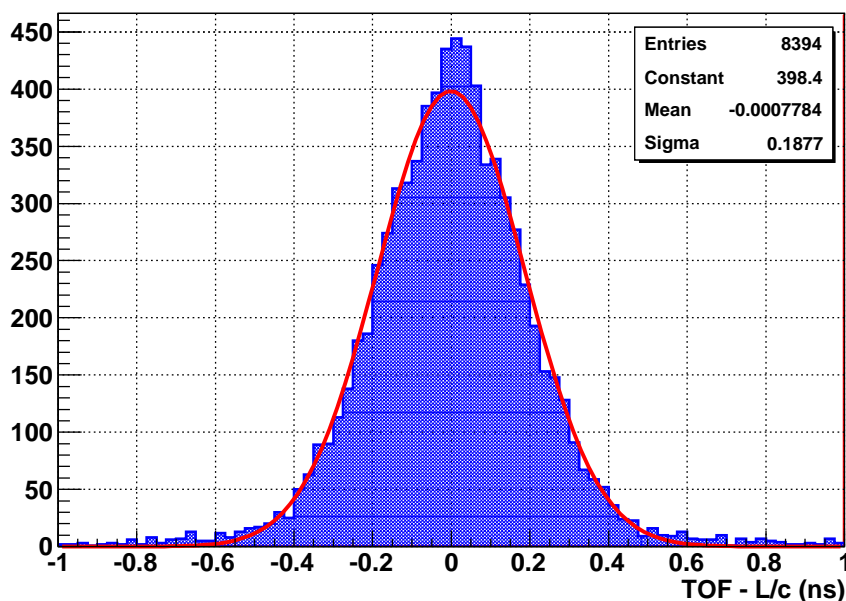
Figure 4.24: Deviation of the measured time-of-flight TOF with respect to the expected value L/c after applying the corrections obtained from all the calibration parameters.

achieved only when single-channel calibration will be done. Nonetheless, a very good result has been obtained even though a calibration approach based on a small number of parameters has been adopted.

The key point of this calibration approach was the identification of the relevant parameters which characterize the TOF detector in a global way. This was possible only thanks to the very good knowledge of the apparatus in all its aspects which allowed to obtain from the detector a good performance even without single-channel calibration. This calibration and the measured time resolution of 130 ps represent a very promising starting point for the ALICE Time-Of-Flight detector, and will allow the TOF detector to contribute to physics results also with the very first beam–beam data at LHC; in fact, particle identification with TOF will be possible even though in a slightly limited range of momenta with respect to the target one. Moreover, looking at the results obtained so far with low-statistics cosmic-ray data, we are extremely confident that further calibrations performed with
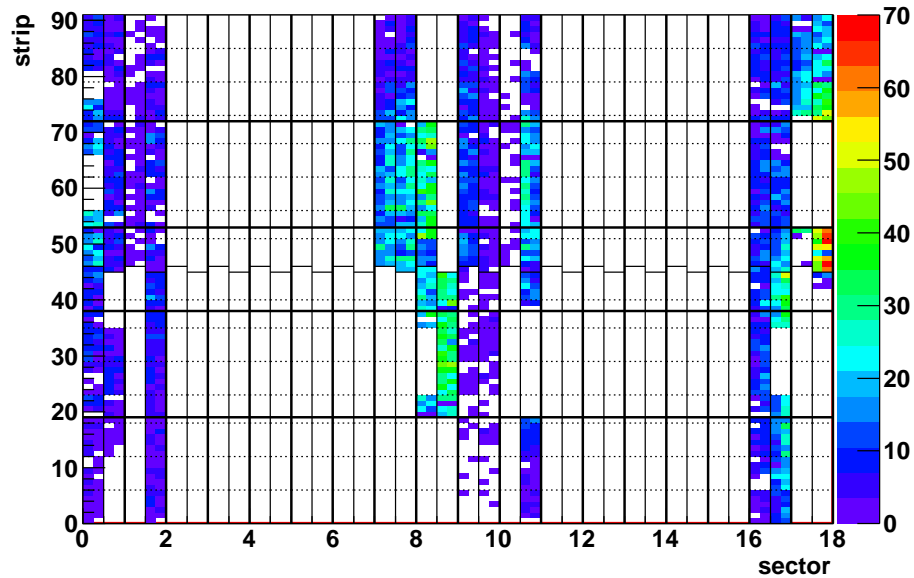
Figure 4.25: Map of the ALICE TOF zones (corresponding to the FEA cards) hit by a reconstructed muon track used for calibration. The colour legend on the right shows the number of muons hitting the zone.

high-statistics beam–beam data will push the TOF detector performance to a time resolution well below 100 ps.

4.4 Cosmic-ray track matching

Particle trajectories in the ALICE central barrel are reconstructed using the position information provided by the tracking detectors, as already said in Section 1.3.3, the Time-Projection Chamber (TPC) being the main tracking device. Reconstructed tracks have to be matched with the signals coming from the other ALICE detectors in order to benefit of the further information added to the track parameters. As an example, the particle time-of-flight information given by the TOF detector enables to measure the particle mass, provided that the particle momentum is known from an independent measurement, as already discussed in Section 2.2.1. The particle trajectory bending radius in a known magnetic field is used for momentum

161

measurement, which is thus performed by the tracking detectors themselves.

In general, the tracks reconstructed by the tracking detectors are extrapolated towards the other detectors following an adequate track parametrization (a helix trajectory in case of solenoidal magnetic field or a straight line trajectory in case of no magnetic field, for instance) to find the corresponding impact point. Eventually, a detector signal to be matched with the track is searched for in the proximity of the track impact point, taking also into account the track parameter errors[13]; when a suitable signal is found, it is associated to the track.

In this section some preliminary results on track matching with the signals of the ALICE Time-Of-Flight detector are presented. The results have been obtained with cosmic-muon tracks, collected during the global commissioning runs with cosmic rays in 2008. The results have to be intended as preliminary results since this study has been performed using the ideal geometrical representation of the ALICE detector[14], which represents the actual detector positions in the experiment only with limited accuracy[15]. Moreover, a big limitation comes from the TPC detector itself, which was not providing the correct track information along the z-coordinate of ALICE, that is along the beam axis. This was due to the fact that the tracks were not reconstructed using the actual TPC gas electron drift-velocity value, as pointed out in Section 4.4.3. Even in this case, a first study on the collected data should enable TPC experts to obtain the actual drift-velocity value. This will allow to perform a second reconstruction pass on cosmic-ray data using the correct reconstruction parameters and therefore a TOF track-matching performance study in better tracking conditions.

---

[13]Track parameter errors as well as parameter correlations are the elements of the track parameter covariance matrix.

[14]The ALICE detector is represented in a three-dimensional geometrical characterization implemented using the GEANT detector description and simulation tool. GEANT allows for a detailed description of detector volumes and materials and provides the tracking of particles through the experimental setup also for simulation of detector response. Moreover, it allows for a graphical representation of the setup and of the particle trajectories [162].

[15]This was the first study on track matching with TOF detector using real cosmic-ray data, therefore the alignment procedure needed to get the current detector position was not yet performed. Nonetheless, this can be done with cosmic-ray tracks to obtain a more realistic geometrical description of the apparatus. This track-matching study can be subsequently reiterated for more accurate results.

Selection cut	Event fraction (%)
no cuts	100
$N_{tracks} > 0$	10.5
$N_{tracks} \leq 2$	6.4

Table 4.2: Event-selection cuts and fraction of events which passes the selection. The cuts have to be intended as subsequent requirements.

4.4.1 Event selection and track reconstruction

The study of track matching with TOF-detector signals has been performed using the cosmic-ray data collected during September–October 2008 ALICE global runs (LHC08d period). The criteria used to select interesting runs are the same which have been used for the calibration with cosmic rays and are described in Section 4.3.1. Also in this case, TOF triggers represent the largest number of the selected events, whereas a small contribution from SPD and TRD triggers corresponds to about 5% of the events.

Track reconstruction

Track reconstruction has been performed using the official reconstruction code of ALICE, which is part of the offline software framework[16]. The details on track reconstruction within ALICE can be found in [115]. No selection cuts (i.e. track parameter covariance, number of TPC clusters associated to the track) have been applied to the reconstructed tracks.

Event selection

Some selection cuts have been applied to the data on the basis of the reconstructed track multiplicity[17] of the event. They are reported in Table 4.2 with the corresponding fraction of selected events and have to be intended as subsequents requirements. The minimum request of non-empty events

---

[16]AliRoot is the name of the ALICE offline framework for the simulation, reconstruction and analysis of the data [163]. It uses the ROOT system as a foundation on which the framework and all applications are built. Except for existing libraries, such as GEANT 3.21 and some remaining legacy code, AliRoot is written in C++.

[17]The only tracks which have been considered for this analysis are the ones which have been reconstructed by the TPC detector. The event multiplicity N_{tracks} is therefore an information coming from the TPC.
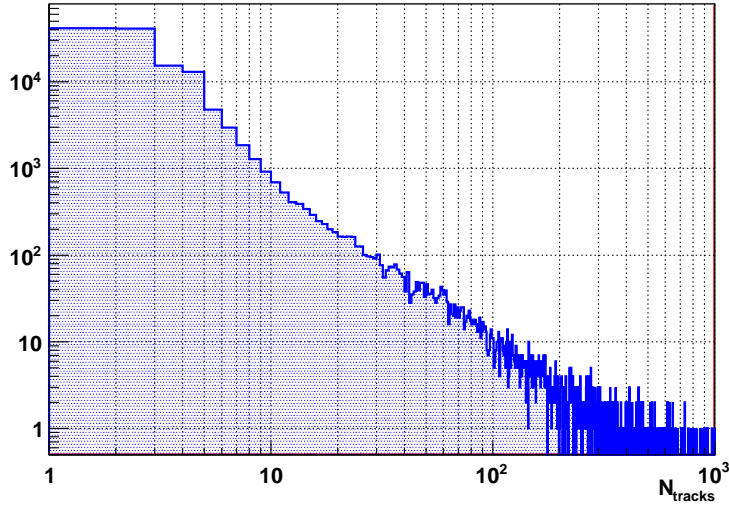
Figure 4.26: Inclusive track-multiplicity distribution of the events before applying the selection cuts.

$N_{tracks} > 0$ causes the rejection of a large fraction of events, while the further request of having low track-multiplicity events $N_{tracks} \leq 2$ causes the rejection of about 40% of the remaining events. The inclusive track-multiplicity distribution before applying the selection cuts is presented in Figure 4.26.

The choice of selecting only low track-multiplicity events with $N_{tracks} \leq 2$ is related to the request of selecting only single-muon events to cope with the non-aligned geometry and with the wrong TPC information on the z-coordinate. Muons are reconstructed by the ALICE offline framework as two separated tracks (which must be correlated, nevertheless) when they cross the TPC dead region located at its internal radius, as they were two back-to-back particles emerging from the beam pipe. This happens because the track-reconstruction algorithm assumes that particles originate from the interaction point. In any case, even though muon trajectories are totally included inside the TPC active volume, they are split into a top-track and a bottom-track[18]; therefore single-muon events are in general two-track events[19]. An

---

[18]The fact that muon trajectories are split into two tracks allows to control and monitor the level of misalignment by comparing the matching of top and bottom tracks.

[19]Nonetheless, if the track crosses only part of the TPC active volume, single-muon
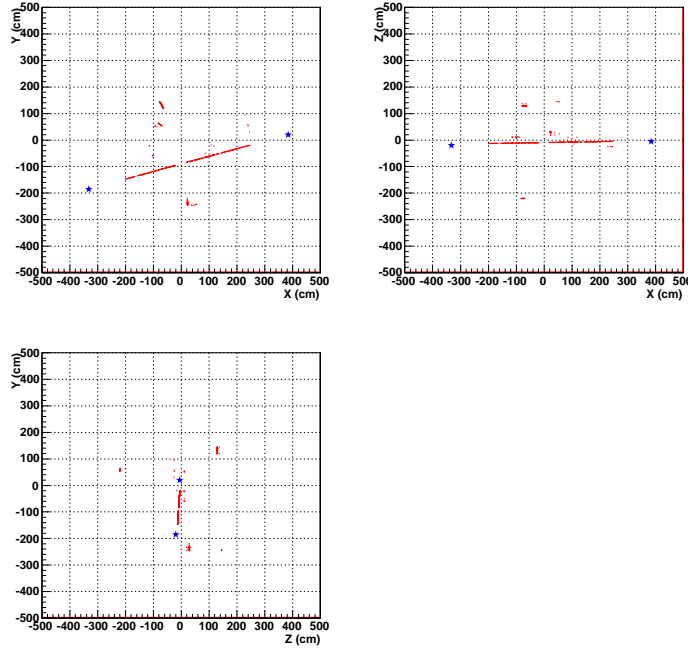
Figure 4.27: Event display of an event with $N_{tracks} = 2$ reconstructed tracks: front-view (top left), top-view (top right) and side-view (bottom left). Single muons are reconstructed as split into two tracks by the ALICE offline reconstruction framework.

example of a single-muon event with $N_{tracks} = 2$ reconstructed tracks is shown in Figure 4.27. Single-muon events are characterized by isolated tracks and isolated TOF clusters, therefore, despite the geometrical misalignment among TPC and TOF detectors and the wrong TPC drift velocity used in the reconstruction, the mismatch probability is low: if a cluster matches the track the matching is likely to be correct.

On the contrary, high track-multiplicity events in the collected cosmic-ray data are mainly due to the interaction of particles with the material surrounding the central detectors: showers generated in the iron yoke of the L3 magnet as well as in the muon absorber can give rise to hundreds of particle tracks in the TPC. As an example, two event displays corresponding to track multiplicities $N_{tracks} = 31$ and $N_{tracks} = 122$ are presented in Figure 4.28

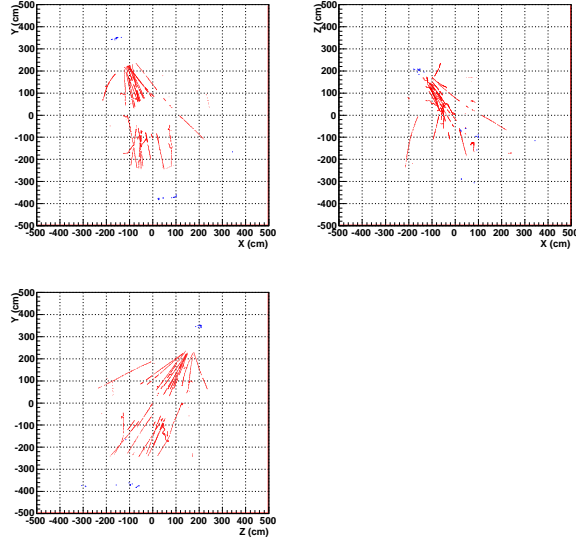events can be reconstructed as single-track events.

Figure 4.28: Event display of an event with $N_{\text{tracks}} = 31$ reconstructed tracks: front-view (top left), top-view (top right) and side-view (bottom left).
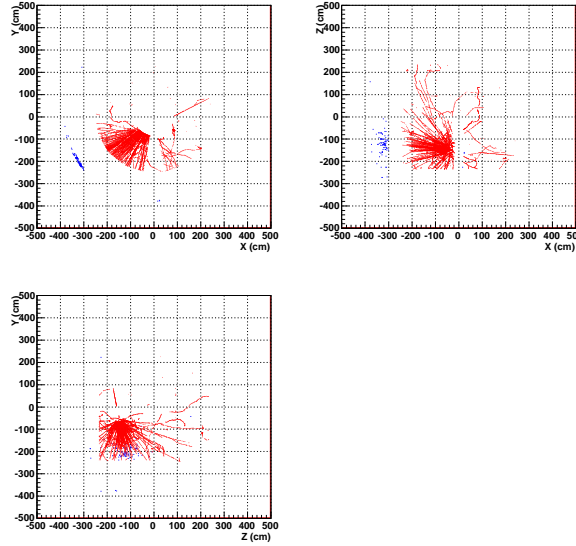

Figure 4.29: Event display of an event with $N_{\text{tracks}} = 122$ reconstructed tracks: front-view (top left), top-view (top right) and side-view (bottom left). A cosmic ray interacts in the muon absorber giving rise to hundreds of particles.
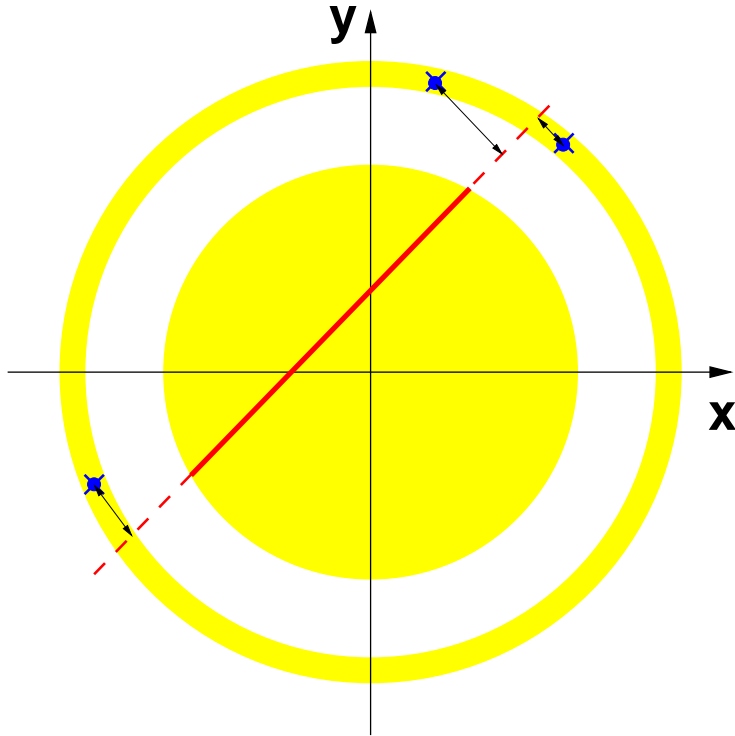
Figure 4.30: Generic scheme of track matching with TOF clusters. The reconstructed track (solid line) is propagated (dashed line) towards the TOF detector to be matched with a TOF cluster (cross symbols). The cluster to be matched is the one with the minimum distance of closest approach to the track.

and 4.29, respectively. When the track multiplicity is high the track-matching performance is corrupted by the poor alignment among TOF and TPC detectors. Moreover, the systematically-wrong position information related to the incorrect TPC drift velocity causes the mismatch probability to be high when the track multiplicity is high.

4.4.2 Track–cluster match procedure

Figure 4.30 shows the generic scheme of the track matching with TOF clusters. Reconstructed tracks are propagated to the TOF detector in the geometrical description of the ALICE detector. Candidate clusters to be
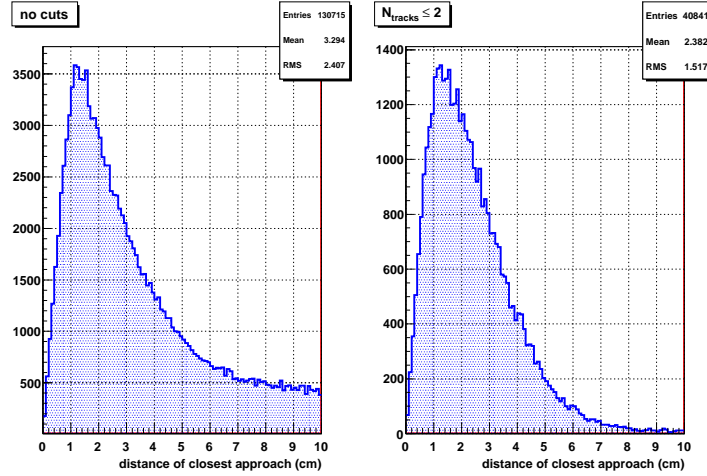
Figure 4.31: DCA distribution to the propagated track of matched TOF clusters before (left) and after applying the $N_{tracks} \leq 2$ event-selection cut (right).
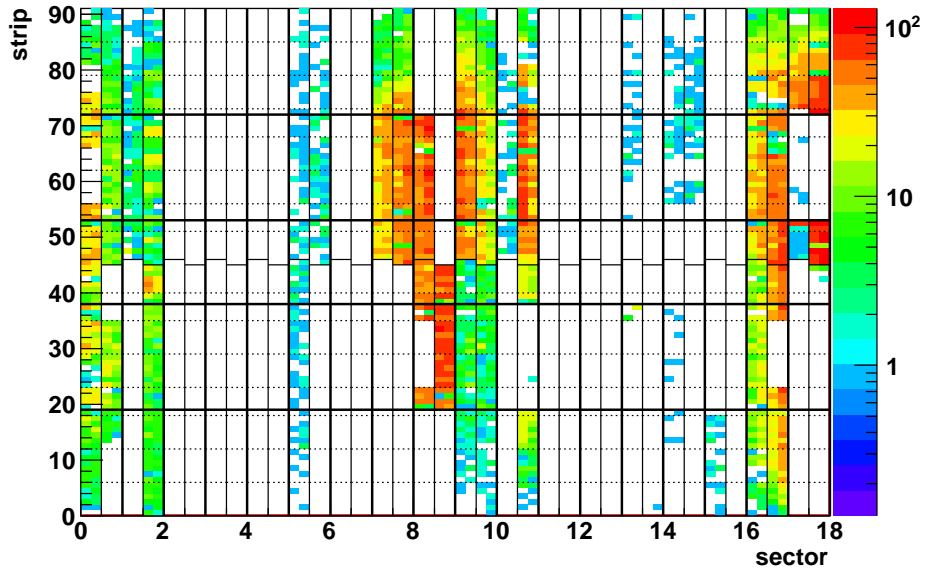

Figure 4.32: Matched-cluster location on TOF detector. The colour map shows the number of clusters matched with respect to the cluster position on TOF in a logarithmic scale.

matched with the track are selected among TOF clusters as the ones whose distance of closest approach (DCA) to the propagated track in three dimensions is less than 10 cm; the readout pad centre is used as the TOF cluster position[20]. The cluster to be matched to the track is selected as the one with the minimum DCA. Matched clusters cannot be shared by two or more tracks.

The DCA distribution of matched clusters obtained before and after applying the event-selection cut $N_{tracks} \leq 2$ is presented in Figure 4.31. The selection cut suppresses the flat background due to mismatched tracks which is present when no cuts are applied. In Figure 4.32 the number of clusters matched with a track with respect to the position on the TOF detector is presented. Notice that not all parts of the TOF detector could match tracks because the complete detector was not active during 2008, as already pointed out.

4.4.3 Track matching: z-coordinate

Track-matching performance has been studied in spite of the imperfect geometrical description. In the first approach the study concentrated only on the z-coordinate, whose direction coincides with the beam axis. The z-coordinate also represents the direction of the TPC drift field and it is therefore affected by the drift velocity value.

As a matter of fact, this study showed that the TPC drift velocity is not constant and that the value used for track reconstruction is not correct. It also showed that, despite the limited position resolution of a few centimetres, the TOF detector is sensitive to the lack of precision in the drift velocity value.

To evaluate the matching performance, the residuals between the extrapolated track z_{track} coordinate and the matched TOF cluster z_{TOF} coordinate

$$\Delta z = z_{track} - z_{TOF} \tag{4.22}$$

have been used, where z_{track} is the z-coordinate of the track at the distance of closest approach to the matched cluster and z_{TOF} is the matched TOF cluster z-coordinate at the pad centre (Figure 4.33).

---

[20]The information on track and cluster position is retrieved from the geometrical description of the apparatus.
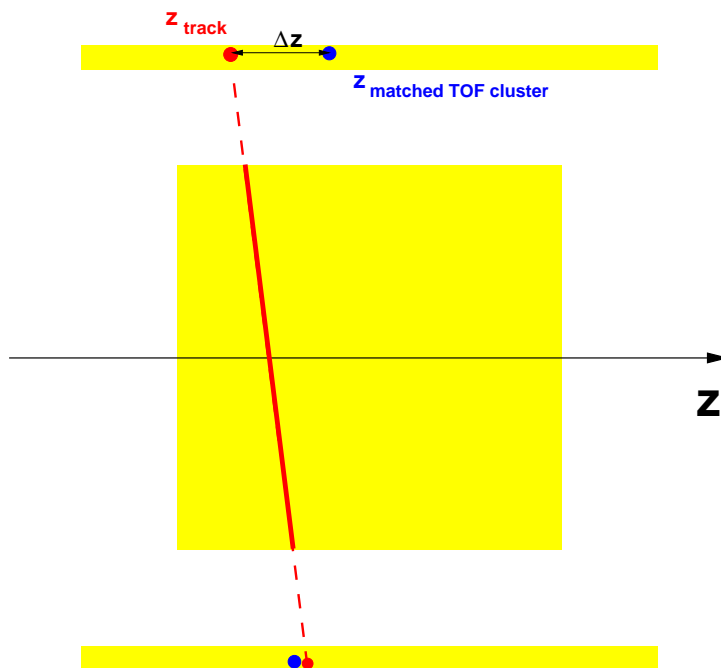
Figure 4.33: Schematic representation of the procedure used to evaluate the track matching in the z-coordinate.

Figure 4.34 shows that the residuals Δz depend on the position z of the matched TOF cluster. Moreover, the behaviour is not constant with time but varies from run to run. Unfortunately, as already anticipated, the TPC drift velocity was not constant during the selected period of data-taking[21], while a fixed drift velocity value was used to reconstruct the particle trajectories in all runs. This is exactly what is observed from Figure 4.34: the wrong value of the TPC drift velocity used during the track-reconstruction stage systematically spoils the reconstructed-track information on the z-coordinate, which is measured through the electron drift time, while the variation of the actual TPC drift velocity with time makes the systematic displacement effect differ from run to run.

This effect prevents any study based on track matching along the z-coordinate, thus any evaluation of TOF track matching performance along the z-coordinate is not reliable so far. Moreover, the systematically wrong

---

[21]Generally, as a first approximation, the TPC drift velocity depends on the ratio P/T, where P and T are the pressure and the temperature of the drift gas mixture, respectively.
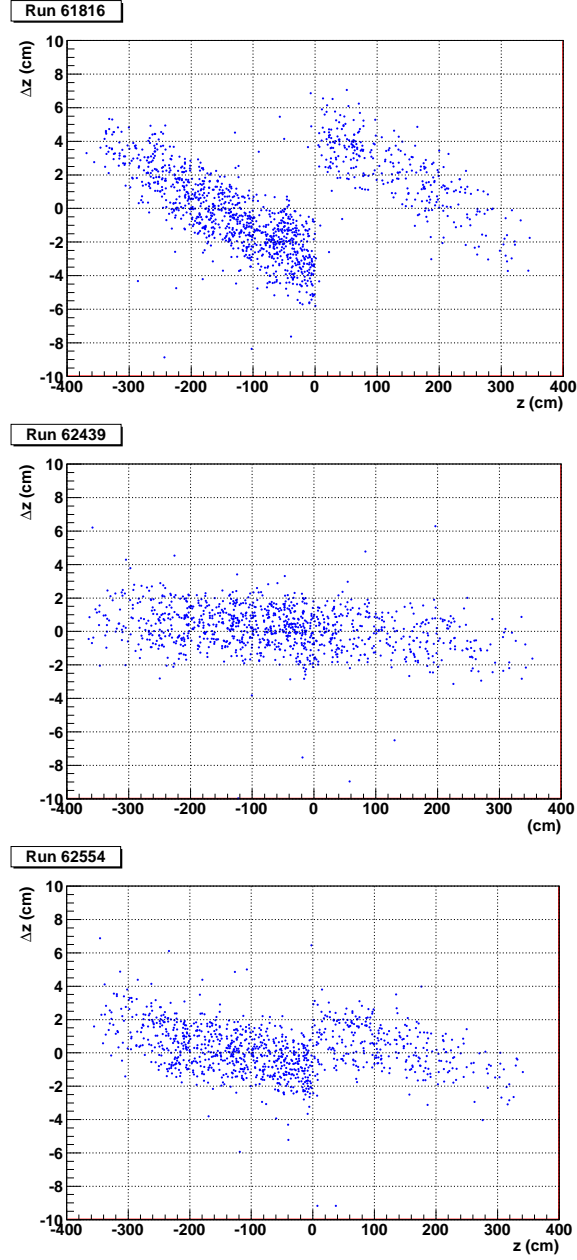
Figure 4.34: Measured residuals Δz (Equation 4.22) as a function of the associated TOF cluster z-coordinate for different runs.
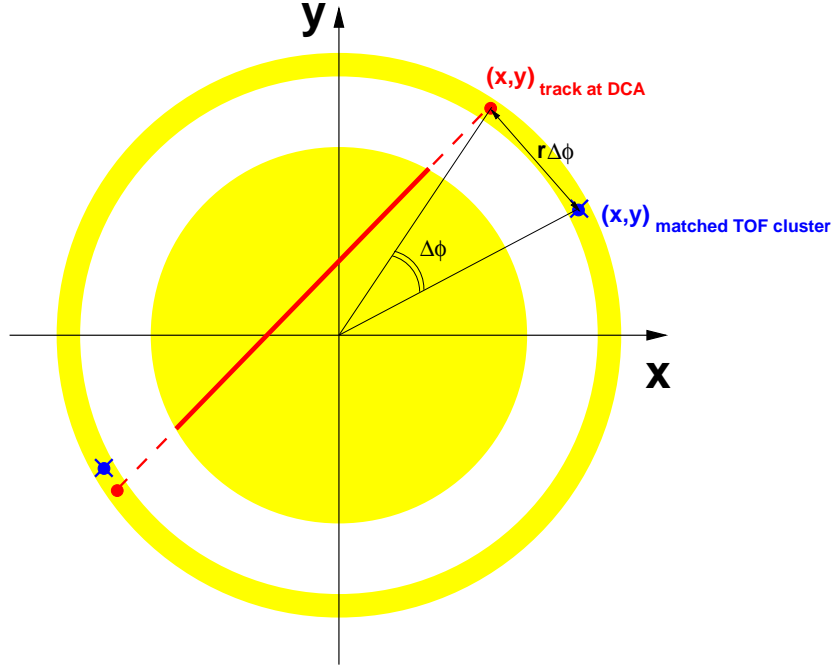
Figure 4.35: Schematic representation of the procedure used to evaluate the track matching in the ϕ-coordinate.

information on the z-coordinate causes the track mismatch probability to increase significantly when the track multiplicity is high, as already anticipated. This, together with the geometrical misalignments, is the main reason for selecting only events with low multiplicity, where muon tracks and TOF clusters are isolated.

4.4.4 Track matching: ϕ-coordinate

The track-matching performance in the ϕ-coordinate is not affected by the TPC drift velocity, being the ϕ-coordinate the azimuthal angle in the bending plane r-ϕ of ALICE. In fact, the measurement of the track azimuthal angle only relies on the spatial information provided by the TPC readout chambers and not on time information, thus it is independent of the electron drift velocity and unaffected by any drift velocity change with time.

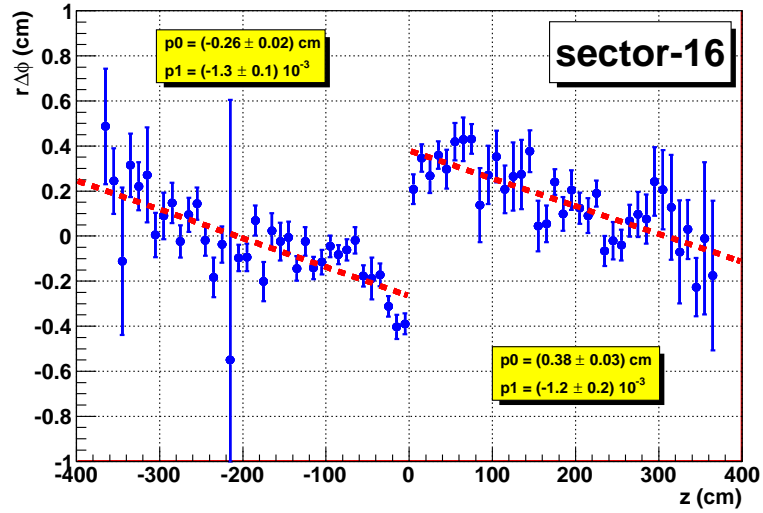To evaluate the matching performance, the residuals between the extrap-

Figure 4.36: Measured residuals $r\Delta\phi$ (Equation 4.26) for TOF Sector-16 as a function of the associated TOF cluster z-coordinate.
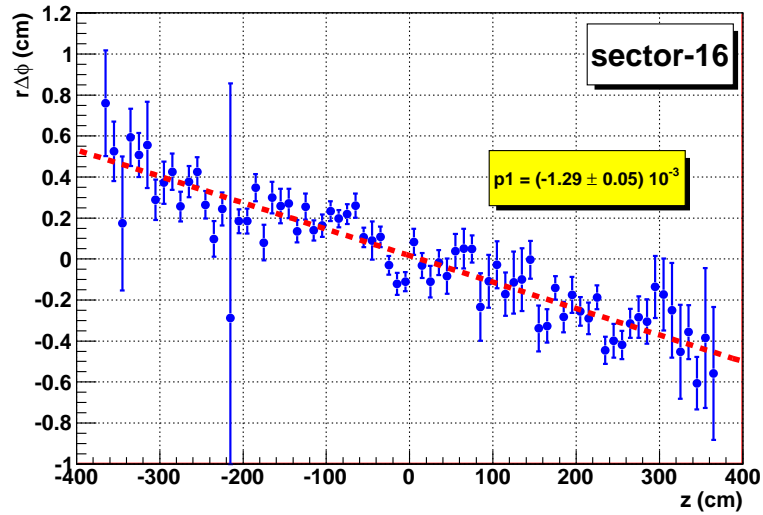

Figure 4.37: Measured residuals $r\Delta\phi$ (Equation 4.26) for TOF Sector-16 as a function of the associated TOF cluster z-coordinate after applying the correction to eliminate the discontinuity.
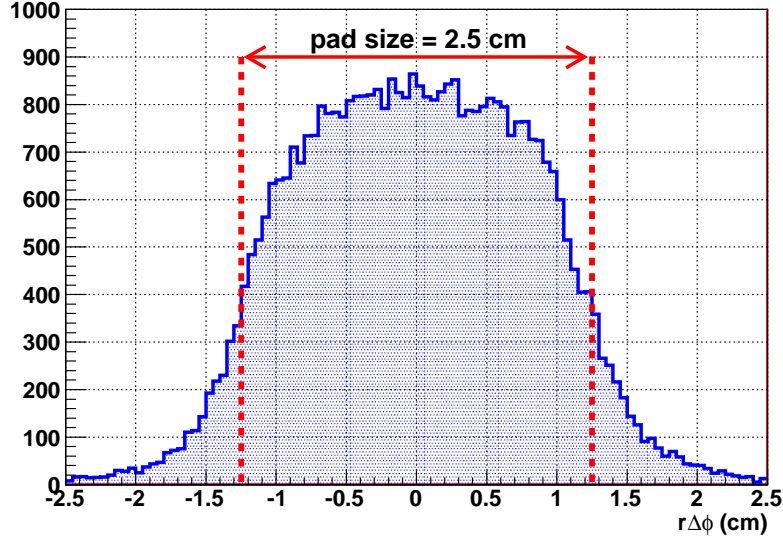
173

Figure 4.38: Distribution of the measured residuals $r\Delta\phi$ after equalizing the displacement of all MRPC strips. The TOF pad transversal size is shown and it is in agreement with the full width at half maximum of the distribution.

olated track ϕ_{track} angle and the matched TOF cluster ϕ_{TOF} angle

$$\Delta\phi = \phi_{track} - \phi_{TOF} \tag{4.23}$$

have been used, where ϕ_{track} is computed using the $(x,y)_{track}$ coordinates of the track at the distance of closest approach to the matched cluster. The angle ϕ_{TOF} is computed using the $(x,y)_{TOF}$ coordinates of the TOF cluster matched to the track, where the pad centre is used as cluster position. A schematic representation of the procedure is presented in Figure 4.35.

The ϕ angles have been computed from the (x,y) coordinates using the two-argument function $atan2(y,x)$ defined as[22]

$$atan2(y,x) = \begin{cases} \phi\,\theta(y) & x > 0 \\ \frac{\pi}{2}\,\theta(y) & x = 0 \\ (\pi - \phi)\,\theta(y) & x < 0 \end{cases} \tag{4.24}$$

---

[22]The $atan2$ function was originally introduced in computer programming languages.

for $y \neq 0$, where ϕ is the angle in $[0, \pi/2]$ such that $\tan(\phi) = \left|\frac{y}{x}\right|$ and $\theta(y)$ is the sign function. The function is defined as

$$atan2(0, x) = \begin{cases} 0 & x > 0 \\ \text{undefined} & x = 0 \\ \pi & x < 0 \end{cases} \qquad (4.25)$$

for $y = 0$.

The residuals $\Delta\phi$ are then used to compute the transverse distance $r\Delta\phi$ between the extrapolated track and the matched TOF cluster in the bending plane

$$r\Delta\phi = r_{TOF}\Delta\phi, \qquad (4.26)$$

where r_{TOF} is the radial distance from the beam axis of the TOF cluster matched to the track, defined as

$$r_{TOF} = \sqrt{x_{TOF}^2 + y_{TOF}^2}. \qquad (4.27)$$

This quantity can be then compared with the TOF pad transversal dimension in the bending plane and it is used to evaluate the matching performance.

Figure 4.36 shows the correlation between the measured $r\Delta\phi$ with respect to the matched TOF cluster position z along the beam line for TOF Sector-16. This example has been chosen to highlight two different effects which can been separately corrected to obtain the final matching performance result. First of all, it is clear that there is an abrupt discontinuity when passing from negative to positive values of the z-coordinate. The second observation is a linear correlation between the two quantities. It has to be kept in mind, nonetheless, that the outcome could be very different when looking at other TOF sectors, and that this is just an example.

The TPC is divided into two separate drift volumes, called "A-side" and "C-side", for positive and negative values of the z-coordinate respectively, each equipped with a set of readout chambers. If the two sets of readout chambers are not well aligned among themselves, the reconstructed track is systematically displaced in one TPC side with respect to the other side, thus giving rise to the discontinuity observed while matching TOF clusters. Nonetheless, since these are preliminary results, at this stage we just correct for the A-side/C-side discontinuity effect, while its actual origin will be deeply studied jointly with TPC experts afterwards. To correct for the A-side/C-side discontinuity we evaluate the measured $r\Delta\phi$ at $z = 0$ by fitting negative

and positive values with a first degree polynomial function $r\Delta\phi = A + B\,z$. The A parameters of the two functions are used to correct the measured $r\Delta\phi$ values for positive and negative z values, respectively. The correction simply applies as

$$\widetilde{r\Delta\phi} = \begin{cases} r\Delta\phi - A^- & z < 0 \\ r\Delta\phi - A^+ & z > 0 \end{cases} \qquad (4.28)$$

where A^- and A^+ are the A parameters of the correction function for negative and positive z coordinates, respectively and $\widetilde{r\Delta\phi}$ is the corrected value. After the correction, the discontinuity disappears, as shown in Figure 4.37. It is worth to point out that the B^- and B^+ parameters for negative and positive values are compatible, thus indicating that the two effects can be decoupled, being one a systematic "side-dependent" shift and the other one a common linear correlation.

After the correction for the systematic shift, the linear correlation effect appears to be a common feature over all the TOF Sector-16 length (Figure 4.37). This effect can be simply explained by a slight angular misalignment between the TOF sector and the TPC with respect to the ideal geometrical configuration. By fitting the graph with a first degree polynomial function it is possible to roughly estimate the angular misalignment: a value of the order of 1.3 cm over a length of 10 metres is measured, which corresponds to about 1.3 mrad. These results are also to be intended as preliminary results and it is worth to say that they do not aim to provide any alignment measurement. Nonetheless, a misalignment effect is observed with cosmic ray tracks, thus indicating that TOF detector alignment with cosmic rays is feasible.

Despite some correction functions could be obtained to correct for both the A-side/C-side discontinuity effect and the angular misalignment of TOF sectors, we have chosen another approach. The mean value of $r\Delta\phi$ has been measured for each MRPC strip and used as a correction in order to equalize all strips centering their $r\Delta\phi$ distributions at zero. The corrected $r\Delta\phi$ values, which we keep referring to as $r\Delta\phi$, are then used to evaluate the matching performance in the ϕ-coordinate. In Figure 4.38 the distribution of the transverse distance $r\Delta\phi$ of all tracks matched with a TOF cluster is presented. As pointed out in the picture, the full width at half maximum of the distribution is in accordance with the transverse size of the TOF pad of 2.5 cm; the smooth edges, on the contrary, are related to the resolution in determining the ϕ-coordinate of the extrapolated track.

4.4.5 Discussion

A preliminary study on track matching with cosmic rays has been performed with the ALICE TOF detector. Despite the approximate geometrical description of the apparatus and the systematically-wrong information on particle trajectories, muon tracks could be matched with TOF signals. The performance evaluated through this study shows that the distance between the extrapolated track and the matched-cluster positions is in accordance with the TOF expected spatial resolution, that is the readout pad size.

Track matching with TOF signals is successfully performed with cosmic rays and it will allow the ALICE experiment to fruitfully profit of the TOF detector contribution for the very first physics results at the LHC.

Conclusions

The Time-Of-Flight (TOF) detector for the ALICE experiment at the CERN Large Hadron Collider (LHC) has been constructed and is presently fully installed and operative at the experimental site. During the construction a wide set of tests has been carried out on the apparatus to guarantee its optimal performance and to acquire a deep experience in the detector characteristics and functioning. The commissioning of the services[23], trigger and readout electronics has been carried out smoothly and is nowadays completed.

A first calibration of the TOF detector has been performed with the cosmic-ray data collected during the global commissioning runs in 2008. Although only a small number of muon tracks was reconstructed for this purpose, which is insufficient for the channel-to-channel calibration, a satisfactory result has been obtained. The good knowledge of the hardware characteristics allowed to identify a smaller set of calibration parameters which has been used taking advantage of global features of the detector. Hence the time resolution could be already pushed down to 130 ps for the time being.

A preliminary study on cosmic-ray track matching with the TOF detector signals shows the good performance of the apparatus and has proved the readiness of the TOF in providing the information to be combined with the central tracking system of ALICE. With the present global time resolution of 130 ps (not including the event-time resolution contribution) particle identification with the ALICE TOF detector will be possible even in the very first beam–beam data of the LHC: a π/K and K/p separation better than 3σ is expected up to a particle momentum $p \simeq 1.8$ GeV/c and $p \simeq 3$ GeV/c respectively, provided that the event time is measured with a 50 ps resolution[24].

---

[23]Low voltage, high voltage, gas system, water-cooling system.

[24]The T0 detector was designed to provide the TOF array with a better than 50 ps

To conclude, the Time-Of-Flight detector of ALICE will add an important contribution to the physics analysis of the first proton–proton data by allowing to extend the particle-identification capabilities of ALICE to higher momenta for the first-physics results at the LHC.

---

resolution event-time information.

Bibliography

[1] E. W. Kolb and M. S. Turner, Front. Phys. **69**, 1 (1990).

[2] L. Evans and P. Bryant, JINST **3**, S08001 (2008).

[3] CERN Large Hadron Collider (LHC), URL `http://lhc.web.cern.ch/lhc/`.

[4] BNL Alternating Gradient Synchrotron (AGS), URL `http://www.bnl.gov/bnlweb/facilities/AGS.asp`.

[5] CERN Super Proton Synchroton (SPS), URL `http://public.web.cern.ch/Public/en/Research/SPS-en.html`.

[6] BNL Relativistiv Heavy-Ion Collider (RHIC), URL `http://www.bnl.gov/rhic/`.

[7] J. L. Nagle, Eur. Phys. J. **C49**, 275 (2007), `nucl-th/0608070`.

[8] I. Y. Pomeranchuk, Dokl. Akad. Nauk Ser. Fiz. **78**, 889 (1951).

[9] R. Hagedorn, Nuovo Cim. Suppl. **3**, 147 (1965).

[10] N. Cabibbo and G. Parisi, Phys. Lett. **B59**, 67 (1975).

[11] J. C. Collins and M. J. Perry, Phys. Rev. Lett. **34**, 1353 (1975).

[12] H. Pagels, Phys. Rept. **16**, 219 (1975).

[13] W. J. Marciano and H. Pagels, Phys. Rept. **36**, 137 (1978).

[14] R. D. Pisarski and F. Wilczek, Phys. Rev. **D29**, 338 (1984).

[15] H. Satz, Nucl. Phys. **A715**, 3 (2003), `hep-ph/0209181`.

[16] New State of Matter created at CERN, CERN Press Release (2000), URL `http://press.web.cern.ch/Press/PressReleases/Releases2000/PR01.00EQuarkGluonMatter.html`.

[17] I. Arsene et al. (BRAHMS), Nucl. Phys. **A757**, 1 (2005), `nucl-ex/0410020`.

[18] B. B. Back et al., Nucl. Phys. **A757**, 28 (2005), `nucl-ex/0410022`.

[19] K. Adcox et al. (PHENIX), Nucl. Phys. **A757**, 184 (2005), `nucl-ex/0410003`.

[20] J. Adams et al. (STAR), Nucl. Phys. **A757**, 102 (2005), `nucl-ex/0501009`.

[21] Z. Fodor and S. D. Katz (C01-08-19), Nucl. Phys. Proc. Suppl. **106**, 441 (2002), `hep-lat/0110102`.

[22] C. R. Allton et al. (2002), `hep-ph/0206200`.

[23] J. Cleymans and K. Redlich, Phys. Rev. Lett. **81**, 5284 (1998), `nucl-th/9808030`.

[24] J. Cleymans and K. Redlich, Phys. Rev. **C60**, 054908 (1999), `nucl-th/9903063`.

[25] F. Karsch, Lect. Notes Phys. **583**, 209 (2002), `hep-lat/0106019`.

[26] B. Svetitsky and L. G. Yaffe, Nucl. Phys. **B210**, 423 (1982).

[27] S. Gavin, A. Gocksch, and R. D. Pisarski, Phys. Rev. **D49**, 3079 (1994), `hep-ph/9311350`.

[28] P. Braun-Munzinger and J. Stachel, Nucl. Phys. **A606**, 320 (1996), `nucl-th/9606017`.

[29] P. Braun-Munzinger and J. Stachel, Nucl. Phys. **A638**, 3 (1998), `nucl-ex/9803015`.

[30] P. Braun-Munzinger and J. Stachel, J. Phys. **G28**, 1971 (2002), `nucl-th/0112051`.

[31] K. G. Wilson, Phys. Rev. **D10**, 2445 (1974).

[32] F. Karsch, E. Laermann, and A. Peikert, Nucl. Phys. **B605**, 579 (2001), `hep-lat/0012023`.

[33] A. Ali Khan et al. (CP-PACS), Phys. Rev. **D63**, 034502 (2001), `hep-lat/0008011`.

[34] P. de Forcrand and O. Philipsen, Nucl. Phys. **B642**, 290 (2002), `hep-lat/0205016`.

[35] S. Ejiri et al., Nucl. Phys. Proc. Suppl. **106**, 459 (2002), `hep-lat/0110080`.

[36] A. Akindinov et al., Eur. Phys. J. **C50**, 341 (2007), `0709.1664`.

[37] R. Preghenella, Master's thesis, Alma Mater Studiorum - Università di Bologna (2005).

[38] J. Rafelski and B. Muller, Phys. Rev. Lett. **48**, 1066 (1982).

[39] BNL/RHIC STAR experiment, URL `http://www.star.bnl.gov/`.

[40] B. I. Abelev et al. (STAR), Phys. Rev. **C77**, 044908 (2008), `0705.2511`.

[41] E. Andersen et al. (WA97), Phys. Lett. **B449**, 401 (1999).

[42] F. Antinori et al., Nucl. Phys. **A698**, 118 (2002).

[43] F. Antinori et al. (NA57), J. Phys. **G32**, 427 (2006), `nucl-ex/0601021`.

[44] S. Okubo, Phys. Lett. **5**, 165 (1963).

[45] G. Zweig (1964), CERN-TH-401.

[46] G. Zweig (1964), CERN-TH-412.

[47] J. Iizuka, K. Okada, and O. Shito, Prog. Theor. Phys. **35**, 1061 (1966).

[48] A. Shor, Phys. Rev. Lett. **54**, 1122 (1985).

[49] J. Rafelski, Nucl. Phys. **A418**, 215c (1984).

[50] M. Jacob and J. Tran Thanh Van, Phys. Rept. **88**, 325 (1982).

[51] P. Koch and J. Rafelski, Nucl. Phys. **A444**, 678 (1985).

[52] A. J. Baltz and C. Dover, Phys. Rev. **C53**, 362 (1996).

[53] H. Sorge, M. Berenguer, H. Stoecker, and W. Greiner, Phys. Lett. **B289**, 6 (1992).

[54] J. H. Chen (STAR), J. Phys. **G35**, 104053 (2008), `0804.4363`.

[55] STAR Collaboration (2008), `0810.4979`.

[56] M. Asakawa and C. M. Ko, Nucl. Phys. **A572**, 732 (1994).

[57] C. Song, Phys. Lett. **B388**, 141 (1996), `hep-ph/9603259`.

[58] M. Asakawa and C. M. Ko, Phys. Lett. **B322**, 33 (1994), `nucl-th/9401016`.

[59] A. Akindinov, Eur. Phys. J. **C45**, 669 (2006), `hep-ph/0601204`.

[60] Y. L. Dokshitzer and D. E. Kharzeev, Phys. Lett. **B519**, 199 (2001), `hep-ph/0106202`.

[61] M. Djordjevic, M. Gyulassy, and S. Wicks, Phys. Rev. Lett. **94**, 112301 (2005), `hep-ph/0410372`.

[62] N. Armesto, A. Dainese, C. A. Salgado, and U. A. Wiedemann, Phys. Rev. **D71**, 054027 (2005), `hep-ph/0501225`.

[63] B. I. Abelev et al. (STAR), Phys. Rev. Lett. **98**, 192301 (2007), `nucl-ex/0607012`.

[64] S. S. Adler et al. (PHENIX), Phys. Rev. Lett. **96**, 032301 (2006), `nucl-ex/0510047`.

[65] P. Braun-Munzinger and J. Stachel, Phys. Lett. **B490**, 196 (2000), `nucl-th/0007059`.

[66] A. Andronic, P. Braun-Munzinger, K. Redlich, and J. Stachel, Phys. Lett. **B571**, 36 (2003), `nucl-th/0303036`.

184

[67] L. Grandchamp and R. Rapp, Phys. Lett. **B523**, 60 (2001), `hep-ph/0103124`.

[68] M. I. Gorenstein, A. P. Kostyuk, H. Stoecker, and W. Greiner, Phys. Lett. **B524**, 265 (2002), `hep-ph/0104071`.

[69] R. L. Thews, M. Schroedter, and J. Rafelski, Phys. Rev. **C63**, 054905 (2001), `hep-ph/0007323`.

[70] M. I. Gorenstein, A. P. Kostyuk, L. McLerran, H. Stoecker, and W. Greiner, J. Phys. **G28**, 2151 (2002).

[71] T. Matsui and H. Satz, Phys. Lett. **B178**, 416 (1986).

[72] H. Satz, Nucl. Phys. **A783**, 249 (2007), `hep-ph/0609197`.

[73] CERN/SPS NA50 experiment, URL `http://na50.web.cern.ch/NA50/`.

[74] M. C. Abreu et al. (NA50), Phys. Lett. **B410**, 327 (1997).

[75] M. C. Abreu et al. (NA50), Phys. Lett. **B410**, 337 (1997).

[76] M. C. Abreu et al. (NA50), Phys. Lett. **B477**, 28 (2000).

[77] B. Alessandro et al. (NA50), Eur. Phys. J. **C39**, 335 (2005), `hep-ex/0412036`.

[78] B. Alessandro et al. (NA50), Eur. Phys. J. **C48**, 329 (2006), `nucl-ex/0612012`.

[79] CERN/SPS NA60 experiment, URL `http://na60.cern.ch/www`.

[80] R. Arnaldi et al. (NA60), Phys. Rev. Lett. **99**, 132302 (2007).

[81] L. Grandchamp, R. Rapp, and G. E. Brown, Phys. Rev. Lett. **92**, 212301 (2004), `hep-ph/0306077`.

[82] A. Capella and E. G. Ferreiro, Eur. Phys. J. **C42**, 419 (2005), `hep-ph/0505032`.

[83] BNL/RHIC PHENIX experiment, URL `http://www.phenix.bnl.gov/`.

[84] A. Adare et al. (PHENIX), Phys. Rev. Lett. **98**, 232301 (2007), `nucl-ex/0611020`.

[85] A. Adare et al. (PHENIX), Phys. Rev. Lett. **101**, 122301 (2008), `0801.0220`.

[86] NASA Cosmic Background Explorer (COBE), URL `http://lambda.gsfc.nasa.gov/product/cobe/`.

[87] L. Stodolsky, Phys. Rev. Lett. **75**, 1044 (1995).

[88] S. Mrowczynski, Phys. Lett. **B430**, 9 (1998), `nucl-th/9712030`.

[89] E. V. Shuryak, Phys. Lett. **B423**, 9 (1998), `hep-ph/9704456`.

[90] M. Asakawa, U. W. Heinz, and B. Muller, Phys. Rev. Lett. **85**, 2072 (2000), `hep-ph/0003169`.

[91] S. Jeon and V. Koch, Phys. Rev. Lett. **85**, 2076 (2000), `hep-ph/0003168`.

[92] J. D. Bjorken (1982), FERMILAB-PUB-82-059-THY.

[93] M. Gyulassy, I. Vitev, X.-N. Wang, and B.-W. Zhang (2003), `nucl-th/0302077`.

[94] A. Kovner and U. A. Wiedemann (2003), `hep-ph/0304151`.

[95] X.-N. Wang and M. Gyulassy, Phys. Rev. Lett. **68**, 1480 (1992).

[96] X.-N. Wang, Phys. Rev. **C58**, 2321 (1998), `hep-ph/9804357`.

[97] R. Baier, D. Schiff, and B. G. Zakharov, Ann. Rev. Nucl. Part. Sci. **50**, 37 (2000), `hep-ph/0002198`.

[98] K. Adcox et al. (PHENIX), Phys. Rev. Lett. **88**, 022301 (2002), `nucl-ex/0109003`.

[99] S. S. Adler et al. (PHENIX), Phys. Rev. Lett. **91**, 072301 (2003), `nucl-ex/0304022`.

[100] T. Isobe (PHENIX), AIP Conf. Proc. **842**, 56 (2006), `nucl-ex/0604016`.

186

[101] J. Adams et al. (STAR), Phys. Rev. Lett. **91**, 072304 (2003), `nucl-ex/0306024`.

[102] C. Adler et al. (STAR), Phys. Rev. Lett. **90**, 032301 (2003), `nucl-ex/0206006`.

[103] C. Adler et al. (STAR), Phys. Rev. Lett. **90**, 082302 (2003), `nucl-ex/0210033`.

[104] J.-Y. Ollitrault, Phys. Rev. **D46**, 229 (1992).

[105] S. Voloshin and Y. Zhang, Z. Phys. **C70**, 665 (1996), `hep-ph/9407282`.

[106] A. Adare et al. (PHENIX), Phys. Rev. Lett. **98**, 162301 (2007), `nucl-ex/0608033`.

[107] R. A. Lacey and A. Taranenko, PoS **CFRNC2006**, 021 (2006), `nucl-ex/0610029`.

[108] B. Muller and J. L. Nagle, Ann. Rev. Nucl. Part. Sci. **56**, 93 (2006), `nucl-th/0602029`.

[109] N. Xu, Nucl. Phys. **A751**, 109 (2005).

[110] S. A. Voloshin, Nucl. Phys. **A715**, 379 (2003), `nucl-ex/0210014`.

[111] S. A. Voloshin, A. M. Poskanzer, and R. Snellings (2008), `0809.2949`.

[112] P. F. Kolb, Heavy Ion Phys. **15**, 279 (2002), `nucl-th/0104089`.

[113] K. Aamodt et al. (ALICE), JINST **3**, S08002 (2008).

[114] F. Carminati et al. (ALICE), J. Phys. **G30**, 1517 (2004).

[115] B. Alessandro et al. (ALICE), J. Phys. **G32**, 1295 (2006).

[116] L3 Collaboration, Nucl. Instrum. Meth. **A289**, 35 (1990).

[117] D. K. Swoboda et al., IEEE Trans. Appl. Supercond. **16**, 1696 (2006).

[118] ALICE Collaboration (1999), CERN-LHCC-99-12.

[119] G. Dellacasa et al. (ALICE) (2000), CERN-LHCC-2000-001.

[120] ALICE Collaboration (2001), CERN-LHCC-2001-21.

[121] ALICE Collaboration (2000), CERN-LHCC-2000-012.

[122] P. Cortese et al. (ALICE) (2002), CERN-LHCC-2002-016.

[123] E. Cerron Zeballos et al., Nucl. Instrum. Meth. **A374**, 132 (1996).

[124] S. Beole et al. (ALICE) (1998), CERN-LHCC-98-19.

[125] ALICE Collaboration (1999), CERN-LHCC-99-04.

[126] P. Cortese et al. (ALICE) (2008), CERN-LHCC-2008-014.

[127] ALICE Collaboration (1999), CERN-LHCC-99-22.

[128] ALICE Collaboration (1999), CERN-LHCC-99-05.

[129] G. Dellacasa et al. (ALICE) (1999), CERN-LHCC-99-32.

[130] ALICE Collaboration (2003), CERN-LHCC-2003-038.

[131] ALICE Collaboration (2004), CERN-LHCC-2004-025.

[132] A. Fernandez et al., Czech. J. Phys. **55**, B801 (2005).

[133] A. Fernandez et al., Nucl. Instrum. Meth. **A572**, 102 (2007), `physics/0606051`.

[134] ALICE Collaboration (2003), CERN-LHCC-2003-621.

[135] V. V. Parchomchuck, Y. N. Pestov, and N. V. Petrovykh, Nucl. Instrum. Meth. **93**, 269 (1971).

[136] M. C. S. Williams (ALICE), Nucl. Instrum. Meth. **A478**, 183 (2002).

[137] F. Anghinolfi et al., Nucl. Instrum. Meth. **A533**, 183 (2004).

[138] M. Mota and J. Christiansen, Proceedings of 2000 Nuclear Science Symposium and Medical Imaging Conference, Lyon, 15–20 October, 2000.

[139] J. Christiansen, *HPTDC Manual version 2.1*, (unpublished).

[140] A. N. Akindinov et al., Nucl. Instrum. Meth. **A533**, 178 (2004).

[141] P. Antonioli and S. Meneghini, Proceedings of the 9th Workshop on Electronics for LHC Experiments, Amsterdam, 29 September–3 October, 2003.

[142] A. Alici, P. Antonioli, A. Mati, S. Meneghini, M. Pieracci, M. Rizzi, and C. Tintori, Proceedings of the 10th Workshop on Electronics for LHC Experiments, Boston, 13–17 September, 2004.

[143] R. Divià, P. Jovanovic, and P. Vande Vyvre, *Data Format over the ALICE DLL*, ALICE-INT-2002-10.

[144] A. Akindinov et al., Nucl. Instr. and Meth. **A** (2008), 10.1016/j.nima.2008.12.016.

[145] A. Akindinov et al. (2005), prepared for 9th ICATPP Conference on Astroparticle, Particle, Space Physics, Detectors and Medical Physics Applications, Villa Erba, Como, Italy, 17-21 Oct 2005.

[146] O. Pinazza et al., Conf. Proc. **C051010**, PO1.058 (2005).

[147] G. Scioli, Ph.D. thesis, Alma Mater Studiorum - Università di Bologna (2005).

[148] A. Alici, Ph.D. thesis, Alma Mater Studiorum - Università di Bologna (2005).

[149] A. Akindinov et al., Nucl. Phys. Proc. Suppl. **158**, 60 (2006).

[150] A. Akindinov et al., Nucl. Phys. Proc. Suppl. **158**, 78 (2006).

[151] A. Akindinov et al., Nucl. Instr. and Meth. **A** (2008), 10.1016/j.nima.2008.12.095.

[152] R. Preghenella, Nuovo Cim. **121B**, 789 (2006).

[153] A. Akindinov, D. Mal'kevich, A. Smirnitskiy, and K. Voloshin (2006), `physics/0606054`.

[154] A. Akindinov et al., Nucl. Instrum. Meth. **A555**, 65 (2005).

[155] ALICE DAQ project, *ALICE DAQ and ECS User's Guide*, ALICE-INT-2005-015.

[156] F. Roukoutakis and O. Cobanoglu, IEEE Trans. Nucl. Sci. **55**, 379 (2008).

[157] S. Chapeland and F. Roukoutakis, J. Phys. Conf. Ser. **119**, 022017 (2008).

[158] ROOT, An Object-Oriented Data analysis Framework, URL `http://root.cern.ch`.

[159] A. Akindinov et al., Proceedings of the 10th Conference on Astroparticle, Particle, Space Physics, Detectors and Medical Physics Applications, Como, 8–12 October, 2007.

[160] A. Akindinov et al., Nucl. Instr. and Meth. **A** (2008), 10.1016/j.nima.2008.12.138.

[161] MINUIT - Function Minimization and Error Analysis, URL `http://wwwinfo.cern.ch/asdoc/minuit/minmain.html`.

[162] GEANT, Detector Description and Simulation Tool, URL `wwwinfo.cern.ch/asd/geant/`.

[163] ALICE Experiment: Offline Project, URL `http://aliceinfo.cern.ch/Offline/`.